DOE/MC/16333-144
(DE83017036
Distribution Category UC-92a

STRESS TRAJECTORY AND ADVANCED HYDRAULIC FRACTURE SIMULATIONS FOR THE EASTERN GAS SHALES PROJECT

Final Report

By
S. H. Advani and J. K. Lee

July 1983

Work Performed Under Contract No. : DE-AC21-81MC16333

For
U. S. Department of Energy
Morgantown Energy Technology Center
P.O. Box 880
Morgantown, WV 26505

By
Ohio State University
Department of Engineering Mechanics
1314 Kinnear Road
Columbus, OH 43212

STRESS TRAJECTORY AND ADVANCED HYDRAULIC FRACTURE SIMULATIONS FOR THE EASTERN GAS SHALES PROJECT

S.H. Advani, Co-Principal Investigator
J.K. Lee, Co-Principal Investigator

Department of Engineering Mechanics
College of Engineering
The Ohio State University
Columbus, Ohio 43210

FINAL REPORT: April 30, 1981 to July 30, 1983

Prepared for the Morgantown Energy Technology Center
U.S. Department of Energy
Under Contract No. DE-AC-21-81MC16333

FOREWORD

This final report describes the effort under U.S. DOE Contract No. DE-AC-21-81MC 16333 with The Ohio State University for the period April 30, 1981 to July 30, 1983. Details pertaining to advanced hydraulic fracture and stress trajectory simulations associated with the Eastern Gas Shales Project are presented.

Dr. S.H. Advani and Dr. J.K. Lee served as Co-Principal Investigators in the program with contract monitoring by Mr. C. Komar and Mr. J. Mercer of the Morgantown Energy Technology Center. Major contributions to this program were made by Dr. M.S. Hamid, Mr. H. Khattab, Mr. O. Gurdogan, Mr. K-S Chen, and Mr. A. Andrews. Professor B. Kulander of Wright State University served as a consultant on the stress trajectory simulations and Professor D. Mendelsohn conducted preliminary formulations on the effects of vertical fracture height on transient well flow behavior.

TABLE OF CONTENTS

Part A

ADVANCED HYDRAULIC FRACTURE SIMULATIONS

ABSTRACT

A summary review of hydraulic fracture modeling is given. Advanced hydraulic fracture model formulations and simulations, using the finite element method, are presented. The numerical examples include the determination of fracture width, height, length, and stress intensity factors with the effects of frac fluid properties, layered strata, *in situ* stresses, and joints. Future model extensions are also recommended.

1.0 INTRODUCTION

Several general purpose as well as custom tailored hydraulic fracture models with varying complexities have been developed by industry and university investigators over the last three decades. The sophistication of recently developed models is often incompatible with the limited data available on the reservoir properties and hydraulic fracture treatment variables.

One of the earliest rigorous hydraulic fracture modeling efforts is due to Kristianovich and Zheltov [1] with the plane strain assumption of a vertical fracture induced by a highly viscous fluid and the frac fluid flow models introduced by Carter [2]. Subsequent coupled flow-structural models by Perkins and Kern [3], Nordgren [4], Geertsma and De Klerk [5], and Daneshy [6] have provided fundamental information on fracture width, length, and leak-off characteristics. Critiques of these models, pertinent assumptions, and numerical comparisons have been presented by Geertsma and Haafkens [7]. Related research on hydraulic fracture mechanisms is due to Haimson and Fairhurst [8], Seth and Gray [9], Wang and Farmer [10], and Shuck and Advani [11].

Incorporation of the effects of elasto-diffusive coupling for investigating hydraulic fracture propagation is due to Rice and Cleary [12] and Ruina [13]. Numerical studies on models with discrete variations of *in situ* stress have been conducted by Simonsen et al. [14] and Advani et al. [15]. The effects of multi-layering have been investigated by Cleary [16], Advani and Lee [17], Daneshy [18], van Eckelen [19], and Hanson [20]. Recent research applicable to vertical hydraulic fracture design and configuration prediction has been reported by Clifton and Abou-Sayed [21], Cleary

[22, 23], Mastrojannis et al. [24], Palmer and Carroll [25, 26], Warpinski et al. [27], Rubin [28], Settari and Cleary [29, 30], Cleary et al. [31, 32], McLeod [33], and Nilson and Griffiths [34]. Of particular note is a basic theory of two dimensional fracture propagation, using a Lagrangian formulation, developed by Biot et al. [35]. This theory has been successfully used for the design of fracture treatments in oil and gas reservoirs in Canada, California, the mid-continent and Rocky Mountains, the North Sea, Gulf Coast, and in northern Germany. A recent overview of current hydraulic fracturing design and treatment technology has been presented by Veatch [36].

Various field tests associated with the Eastern Gas Shales Project and Western Gas Sands Project [37, 38] along with mine back experiments [39, 40] have been performed. A Multi-Well Experiment (MWX) is currently being conducted by Sandia National Laboratories [41] to enhance technology and energy recovery related to the low permeability, lenticular gas sands in the West. A mine back program in the East is currently in the planning stages [42]. Results of several small scale experiments have been presented by Teufel and Clark [43], Anderson [44], Rubin [45], Ingraffea[46], Biot et al. [47], Kenner et al. [48], Schmidt [49] and Papadopoulos et al. [50]. These laboratory experiments have investigated the roles of fracture toughness, multilayering, in situ stresses, friction across interfaces and fracture growth. Interpretations of field fracture parameters from pressure decline curves have been made by Nolte [51]. Research on proppant transport has been reported by Novotny [52] and a related summary of proppant transport models and settling velocity correlations has been presented by Clark and Quadir [53] and Clark and Güler [54].

In this report, finite element hydraulic fracture simulations associated with fracture width, length, height, and stress intensity prediction along with leak-off characterization are reported. In addition, various extensions and applications of developed models are reported.

2.0 ADVANCED HYDRAULIC FRACTURE MODEL FORMULATIONS

In this section, finite element formulations for the prediction of hydraulic fracture geometry, stress intensity factors, and frac fluid leak off are presented. The initial analysis is conducted for an isotropic, homogeneous elastic medium subjected to uniform tectonic stress. Subsequent extensions to cases with layering, differential tectonic stress, and joint effects are also presented with numerical examples in Section 3.0.

2.1 Fracture Width, Length, and Stress Intensity Model Formulations

The idealized vertical fracture configuration is selected to have constant height H (Figure 1). In addition, for each vertical cross section perpendicular to the propagation direction, the crack fluid pressure p is assumed constant with its magnitude equal to the minimum horizontal stress σ_{HMIN} at the fracture front x = L. The vertical elliptic cross section width w can then be characterized by

$$w(x,z,t) = \frac{(1-\nu)H\Delta p(x,t)}{G}\left(1-\left(\frac{2z}{H}\right)^2\right)^{1/2} \tag{1}$$

where G, ν are the formation shear modulus and Poisson's ratio respectively and $\Delta p = p - \sigma_{HMIN}$ is the effective crack opening pressure. From the definition of the maximum width $W(x,t) = w(x,0,t)$ and Eq. 1, we have

$$\Delta P = \frac{G}{H(1-\nu)} W(x,t) \tag{2}$$

For a non-Newtonian power frac fluid, the shear stress τ_{ij}-shear rate $\dot{\gamma}_{ij}$ relationship is characterized by

$$\tau_{ij} = K' \dot{\gamma}_{ij}^{n'} \tag{3}$$

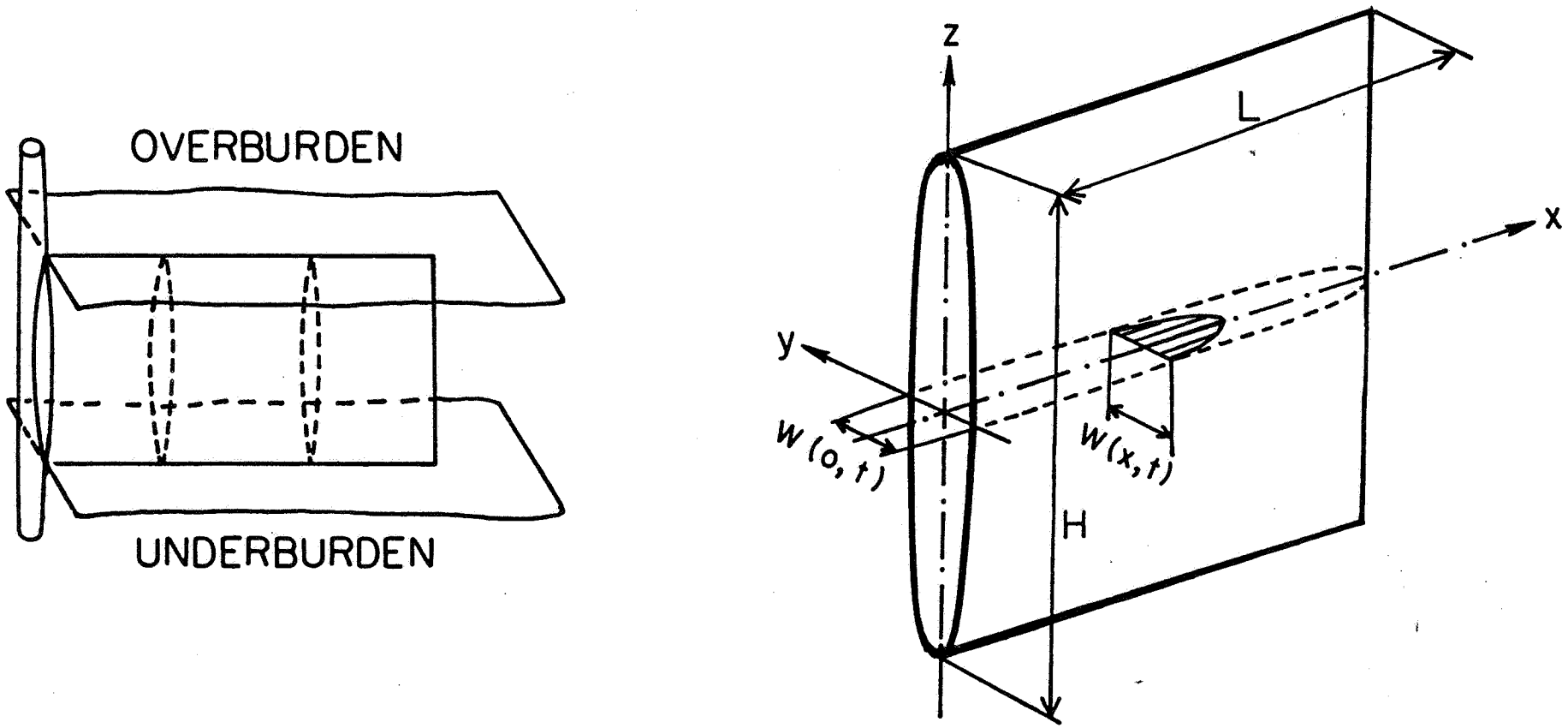

Figure 1: Vertical Fracture Model Idealization

where K' is the consistency index and n' is the flow behavior index. For n'=1, the fluid behaves Newtonian and K'=μ is the conventional fluid viscosity. The pressure gradient for flow in an elliptical channel, from momentum considerations, is

$$\frac{\partial}{\partial x}(\Delta p) = -\frac{64}{3\pi}\frac{K'}{W}\left[\frac{Q}{HW^2}\left(\frac{2n'+1}{n'}\right)\right]^{n'} \tag{4}$$

where Q is the flow rate. For an incompressible fluid, the continuity equation is

$$\frac{\partial Q}{\partial x} + \frac{\pi H}{4}\frac{\partial W}{\partial t} + Q_L = 0 \tag{5}$$

Where $Q_L = \frac{2HC}{(t-\tau(x))^{1/2}}$ is the fluid leak-off rate, C is the combined fluid loss coefficient, and $\tau(x)$ is the elapsed time when the frac fluid reaches coordinate x. The loss coefficient, for an incompressible fluid with constant crack pressure, from Darcy's law is given by

$$C = [\phi\, K\Delta p/2\mu]^{1/2} \tag{6}$$

where ϕ is the formation porosity and K is the formation permeability. Different representations of C including the effects of compressibility, wall building, filtrate displacement along with their combined form have been recently developed by Settari [55].

From Eqs. (2), (4) and (5), we obtain the width equation, for $0<x<L(t)$ and $t>0$,

$$\left(-\frac{1}{M}\right)^{\frac{1}{n'}}\frac{\partial}{\partial x}\left[\left(\frac{\partial}{\partial x}W^{2n'+2}\right)^{\frac{1}{n'}}\right] + \frac{\pi H}{4}\frac{\partial W}{\partial t} + \frac{2HC}{(t-\tau)^{1/2}} = 0 \tag{7}$$

where $M = \frac{128K'(1-\nu)}{3\pi G}H^{1-n'}(n'+1)\left(\frac{2n'+1}{n'}\right)^{n'}$.

Equation (7) is subjected to the initial condition $W(x,0) = 0$ and the boundary condition $W(x,t) = 0$ for $x \geq L(t)$. For a two-sided fracture $Q_2(0,t) = \frac{Q_o}{2}$ and the appropriate boundary condition is

$$\left[\frac{\partial}{\partial x} W^{2n'+2}\right]_{x=0} = - MQ_2^{n'} \tag{8}$$

The coupled length magnitude at a given instant, for the case of the frac fluid residing at the fracture tip, can be obtained from the volume balance associated with the pumped fluid, fracture volume, and leak-off volume. For a uniform flow rate Q_o, we have

$$\frac{\pi H}{4} \frac{d}{dt} \int_o^{L(t)} W(x,t)\, dx + 2HC \int_o^t \frac{dL}{d\tau} \frac{d\tau}{(t-\tau)^{1/2}} = Q_2 \tag{9}$$

Various finite element formulations can be provided for the set of governing equations (7) and (9). An attractive way is to introduce a simple transformation $\xi = x/L(t)$ to minimize difficulties associated with the free boundary in Equation (7), which permits Equations (7) and (9) to be rewritten as

$$\left(-\frac{1}{LM}\right)^r \frac{1}{L} \frac{\partial}{\partial \xi} \left(\frac{\partial}{\partial \xi} W^{2+2n'}\right)^r + \frac{\pi H}{4} \frac{\partial W}{\partial t} + 2HCf(t,\tau) = 0 \tag{10}$$

and

$$\frac{\pi H}{4} \frac{d}{dt} \left(L \int_o^1 W(\xi,t) d\xi\right) + 2HC \int_o^t f(t,\tau) \frac{dL}{d\tau} d\tau = Q_2 \tag{11}$$

respectively, with $\xi \varepsilon [0,1]$, $r = 1/n'$ and $f = 1/(t-\tau)^{1/2}$. Now the width equation can be discretized on the fixed interval [0,1] by taking, with

the usual summation convention on repeated indices,

$$W(\xi,t) \simeq W^j(t)\ N_j(\xi) \tag{12}$$

and use of the Galerkin approach to yield

$$K_{ij}(W(\xi,t),\ L(t))\ W^j(t) + C_{ij}\ \dot{W}^j(t) + F_i = 0 \tag{13}$$

where

$$K_{ij}(W,L) = -\frac{1}{L}\left[-\frac{2(n'+1)}{ML}\right]^r \int_0^1 \frac{\partial N_i}{\partial \xi}\ (W^k N_k)^{2+r}\left(W^\ell \frac{\partial N_\ell}{\partial \xi}\right)^{r-1} \cdot$$

$$\frac{\partial N_j}{\partial \xi}\ d\xi$$

$$C_{ij} = \frac{\pi H}{4} \int_0^1 N_i N_j d\xi$$

$$F_i = 2HC \int_0^1 f\ N_i\ d\xi - \frac{Q_2}{L(t)}\ N_i\Big|_{\xi=0}$$

The usual two-point time stepping method along with the Newton-Raphson iteration can be used to solve (13) when the fracture length L(t) is known.

As for the prediction of the fracture length, we let

$$g(t) = \int_0^1 W(\xi,t)d\xi$$

and rewrite Eq. (11) as

$$L(t)\ \frac{dg}{dt} + g(t)\ \frac{dL}{dt} + \frac{8C}{\pi} \int_0^t f(t,\tau)\ \frac{dL}{d\tau}\ d\tau = \frac{4Q_2}{\pi H} \tag{14}$$

The third term in Eq. (14) dominates and this results in numerical instability when the Galerkin approach is used, similar to the case of convection dominant diffusion problems. The weighted residual method can be applied to the integro-differential equation (14) by modifying the procedure outlined by Reddy and Murty [56]. The upwinding functions ψ_i are expressed in the form [57]

$$\psi_1(\xi) = N_1(\xi) + \alpha F(\xi)$$
$$\psi_2(\xi) = N_2(\xi) - \alpha F(\xi) \tag{15}$$

where $N_i(\xi)$ are the usual isoparametric shape functions used in Eq. (12) and

$$F(\xi) = -\frac{3}{4}(1 - \xi)(1 + \xi)$$

The length equation (14) can now be discretized in the fluid injection time interval [0,T] by taking

$$L(t) = L^j \phi_j(t)$$

to obtain

$$(G_{ij}(W) + S_{ij}(\dot{W}))\ L^j - Q_i = 0 \tag{16}$$

where the elements are taken in the time domain and

$$G_{ij} = \int_0^T \psi_i \left(W^k(t) \int_0^1 N_k(\xi) d\xi \right) \frac{d\phi_j}{dt}\, dt$$
$$+ \frac{8C}{\pi} \int_0^T \psi_i \left(\int_0^t \frac{d\phi_j}{d\tau} f\, d\tau \right) dt$$
$$S_{ij} = \int_0^T \psi_i \left(\dot{W}^k \int_0^1 N_k\, d\xi \right) \phi_j\, dt$$

$$Q_i = \frac{4}{\pi H} \int_0^T Q_2 \psi_i \, dt$$

The strongly coupled semi-discrete equations (13) and (16) must be solved simultaneously to obtain fracture width and length at a given time. For convenience in computations, the number of time steps used to solve (13) can be considered as the numbers of time elements in (16) having nodal points at the same time stations. The following steps can be taken for a successive approximation:

i) set m = 0 and initialize

ii) compute $\underset{\sim}{L}_m(t)$ according to (43) for each time node t ϵ [0,T]

iii) solve(13) with $\underset{\sim}{L}_m$ for each time step to obtain $\underset{\sim}{W}_m$ and $\dot{\underset{\sim}{W}}_m$

iv) solve (16) with $\underset{\sim}{W}_m$ and $\dot{\underset{\sim}{W}}_m$ to obtain $\underset{\sim}{L}_{m+1}$ containing new time nodal values

v) if max $|L^i_{m+1} - L^i_m| > \epsilon_{tol}$, go to step iii) with m = m+1

vi) print and stop

The Newton-Raphson method used in step iii) requires 10~20 iterations while the successive approximation involving steps iii) and iv) converges within 2~5 iterations, indicating that the fracture length estimate (43) is fairly good.

The instantaneous crack opening mode stress intensity factor K_I during fracture extension is given by

$$K_I(t) = \frac{1}{(\pi L)^{1/2}} \int_{-L(t)}^{L(t)} \Delta p \left(\frac{L+x}{L-x} \right)^{1/2} dx \qquad (17)$$

Using the effective pressure width relation for the horizontal plane, equation (17) yields

$$K_I(t) = \frac{G}{2(1-\nu)L(\pi L)^{1/2}} \int_{-L(t)}^{L(t)} W(x,t) \left(\frac{L+x}{L-x}\right)^{1/2} dx \qquad (18)$$

Introducing the coordinate transformation $\xi = x/L$ in equation (17), following symmetry simplifications, we get

$$K_I(t) = \frac{G}{(1-\nu)(\pi L)^{1/2}} \int_0^1 \frac{W(\xi,t)}{(1-\xi^2)^{1/2}} d\xi \qquad (19)$$

Equation (19) can be numerically integrated using the Gauss-Legendre procedure after solving for $W(\xi,t)$ at each time step.

In lieu of the leak-off representation governed by Eq. 7, a refinement entailing an iterative scheme based on the local and global frac fluid mass balance has been developed as follows:

i) Assume an initial fracture length L_o and select the facture width profile based either on the previous one dimensional formulation or the classical models [7].

ii) Evaluate the trial crack pressure profile from Eq. 1.

iii) Compute the fracture volume and pertinent time interval from the injected flow rate.

iv) Using the pressure distribution $\Delta P(x,t)$ along the fracture length, simulate the two dimensional transient Darcy flow equation (with frac fluid compressibility) using the finite element method.

v) From the pressure distribution in the formation, the leak-off velocity is determined from Darcy's law and hence the leak-off value is obtained. Global mass balance is employed and the appropriate time is determined by iteration.

vi) The local balance Eq. 5 is used and the crack pressure gradient is determined from Eq. 4.

vii) The pressure profile is then recomputed from the previously determined pressure gradient and the corresponding width profile is evaluated.

viii) The evaluated ΔP is compared with steps (ii) and steps (iii) through (vii) are repeated with a revised width until the "correct" ΔP with a specified tolerance is obtained.

ix) The crack length is advanced until injection ceases and the above procedure is repeated.

The flow chart for this computational procedure is illustrated in Fig. 2. It is noteworthy that a pressure dependent compressibility and shear rate dependent viscosity effects can be introduced in the preceding formulation. A more comprehensive formulation involves utilization of the Navier - Stokes flow equations in the crack which is coupled with the Darcy flow equation in the formation. Appropriate coupling at the frac fluid front - virgin formation interface involves continuity of pressure and flow intensity. The associated numerical effort involving the interface coupling is formidable.

2.2 Fracture Width and 2D Vertical Fracture Configuration Model Formulations

As indicated in the introduction, various advanced models for predicting vertical hydraulic fracture geometry have been presented in the literature. In particular, Clifton and Abou-Sayed [21] have reported a variational methodology for the prediction of three dimensional geometry. The associated elasticity and flow problems are reduced to a 2D formulation by means of an integral equation relating crack width and pressure and by considering crack fluid flow in the plane of the crack. Cleary et al. [32] have recently developed approximate lumped and P3DH models for use on a micro-computer.

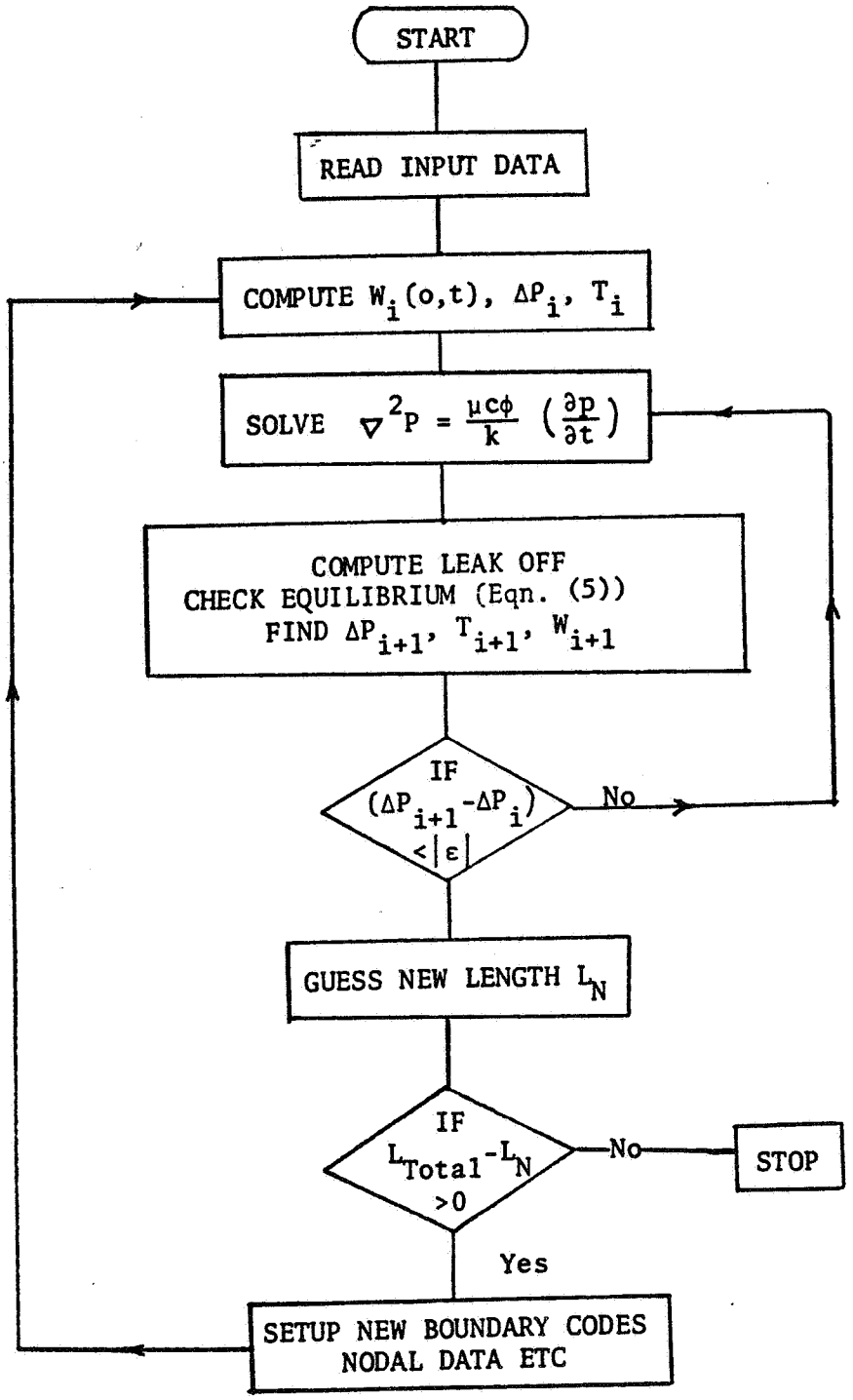

Figure 2: Schematic Flow Chart for Undefined Leak-Off Function Simulation

These models combine the characteristics of the Perkins-Kern-Nordgren and the Geertsma-DeKlerk models for propagation in the length (height) and height (length) directions, respectively. More complex pseudo-three-dimensional (P3DH) models have also been simulated as special cases of the work by Settari and Cleary [30] and Cleary et al. [31].

Here, finite element model formulations for fracture width, 2D vertical fracture configuration, and stress intensity factor are presented using the basic framework reported in Section (2.1).

A schematic of the fracture geometry is illustrated in Fig. 3. The approximate fracture width (w)-effective crack pressure (Δp) relation is given by

$$w(x,y,t) = c(x) \int_{y/h(x)}^{1} \frac{su(s)\, ds}{(s^2-(y/h(x)^2)^{1/2}} \tag{20}$$

where

$$u(s) = \int_{o}^{s} \frac{\Delta p(f,t)}{(s^2-f^2)^{1/2}}\, df \tag{21}$$

$$c(x) = \frac{2(1-\nu)}{\pi G}\, h(x)$$

The momentum equations for fluid flow in the crack are selected in the form

$$\frac{\partial}{\partial x}(\Delta p) + \frac{\eta'}{w^{4n+3}} |q|^{2n} q_x = 0 \tag{22}$$

$$\frac{\partial}{\partial y}(\Delta p) + \frac{\eta'}{w^{4n+3}} |q|^{2n} q_y = 0 \tag{23}$$

where q_x, q_y are flow rates in the x and y directions, respectively, $|q| = (q_x^2+q_y^2)^{1/2}$ is the resultant flow rate magnitude, and parameters n and η' are related to the conventional non-Newtonian frac fluid properties as follows:

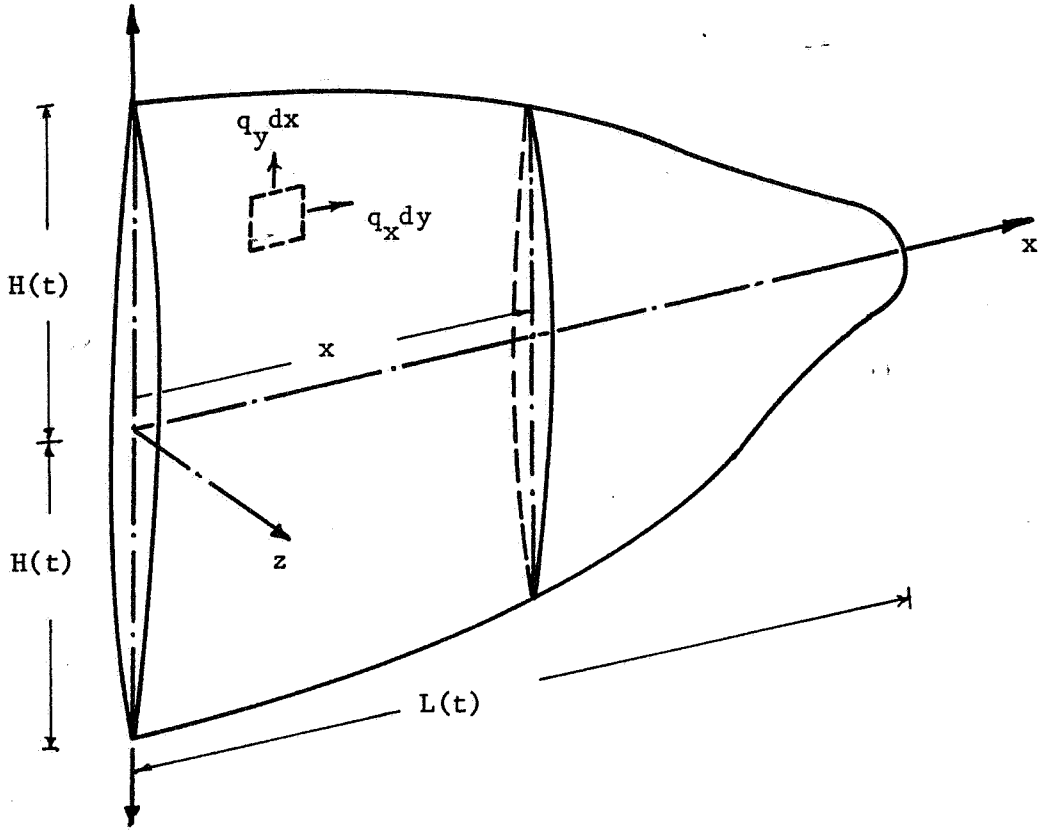

Figure 3a: Schematic of Vertical Fracture Configuration

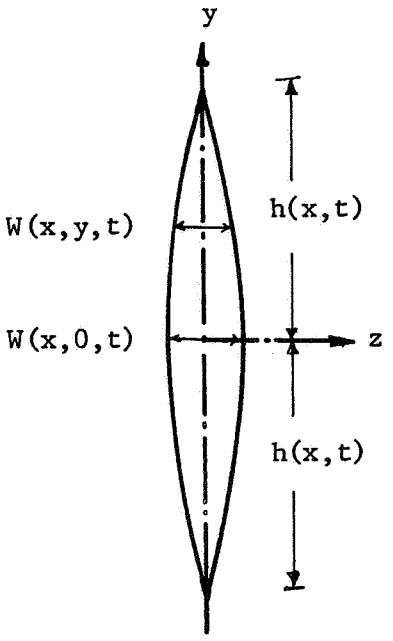

Figure 3b: Vertical Fracture Width Profile

$$\eta' = K'\left[\left(2 + \frac{1}{n'}\right)2^{\left(1+\frac{1}{n'}\right)}\right]^{n'} \tag{24}$$

$$n = \frac{n'-1}{2} \tag{25}$$

In the above, K' is the consistency index of the fluid and n' is the flow behavior index.

For an incompressible fluid, the continuity equation is

$$\frac{\partial q_x}{\partial x} + \frac{\partial q_y}{\partial y} + q_L + \frac{\partial w}{\partial t} = 0 \tag{26}$$

where $q_L = \dfrac{2C}{(t-\tau(x,y))^{1/2}}$ is the fluid leak-off rate per unit area, C is the lumped fluid loss coefficient, and (x,y) is the elapsed time when the frac fluid reaches the crack surface coordinates x, y.

Suitable manipulation of Eqs. (22) and (23) yields

$$|q|^{2n} = \left(\frac{w^{4n+3}}{\eta'}\right)^{\frac{2n}{2n+1}} \left[\left(\frac{\partial}{\partial x}(\Delta p)\right)^2 + \left(\frac{\partial}{\partial y}(\Delta p)\right)^2\right]^{\frac{n}{2n+1}} \tag{27}$$

Substituting Eq. (27) in (22) and (23), and defining $\xi = x/L$ and $\eta = y/H$, we obtain the following expressions for q_ξ and q_η

$$q_\xi = -\lambda\, w^{2+r}\, \frac{1}{L}\left(\frac{\partial \Delta p}{\partial \xi}\right)\left[\frac{1}{L^2}\left(\frac{\partial \Delta p}{\partial \xi}\right)^2 + \frac{1}{H^2}\left(\frac{\partial \Delta p}{\partial \eta}\right)^2\right]^{\frac{r-1}{2}} \tag{28}$$

$$q_\eta = -\lambda\, w^{2+r}\, \frac{1}{H}\left(\frac{\partial \Delta p}{\partial \eta}\right)\left[\frac{1}{L^2}\left(\frac{\partial \Delta p}{\partial \xi}\right)^2 + \frac{1}{H^2}\left(\frac{\partial \Delta p}{\partial \eta}\right)^2\right]^{\frac{r-1}{2}} \tag{29}$$

with $r = \dfrac{1}{n'}$ and $\lambda = \left(\dfrac{1}{\eta'}\right)^r$.

The governing coupled equations for pressure (Δp) and width now reduce to the following:

$$\frac{1}{L}\frac{\partial q_\xi}{\partial \xi} + \frac{1}{H}\frac{\partial q_\eta}{\partial \eta} + q_L + \frac{\partial w}{\partial t} = 0 \tag{30}$$

$$w(\xi,\eta,t) = c(\xi)\int_{\beta}^{1}\frac{sds}{(s^2-\beta^2)^{1/2}}\left(\int_{o}^{s}\frac{\Delta p(f,t)}{(s^2-f^2)^{1/2}}\,df\right) \tag{31}$$

where

$$\beta = \frac{\eta H}{h(\xi)}$$

and

$$c(\xi) = \frac{2(1-\nu)}{\pi G}\,h(\xi) \quad .$$

Although the above formulation is presented for an elastic isotropic medium, subjected to a uniform tectonic stress, it can be extended to cases with layering and in situ stress variation across the layers. For a symmetric vertical fracture, the following boundary conditions are assumed for Eqs. (30) and (31)

$$q_{\xi}(0,\eta,t) = \frac{Q_o}{2} = Q_2$$

$$\frac{\partial \Delta P}{\partial \eta}(\xi,0,t) = 0$$

$w(\xi,\eta,t) = 0$ outside the fracture domain Ω

The weak form of Eq. 30 after use of the Green's theorem, boundary conditions and Eqs. (28) and (29) is

$$\int_{\Omega}\lambda\, w^{2+r}\left[\frac{1}{L^2}\left(\frac{\partial \Delta P}{\partial \xi}\right)^2+\frac{1}{H^2}\left(\frac{\partial \Delta P}{\partial \eta}\right)^2\right]^{1/2(r-1)}\left\{\frac{1}{L^2}\frac{\partial \Delta P}{\partial \xi}\frac{\partial v}{\partial \xi}+\frac{1}{H^2}\frac{\partial \Delta P}{\partial \eta}\frac{\partial v}{\partial \eta}\right\}d\xi d\eta$$

$$+\int_{\Omega}\frac{2C}{(t-\tau)^{1/2}}\,v\,d\xi d\eta+\int_{\Omega}\frac{\partial w}{\partial t}\,v\,d\xi d\eta-\frac{Q_2}{L}\int_{s}v\,ds=0 \tag{32}$$

where $v(\xi,\eta)$ is a pre-multiplying smooth function. Similarly, the weak form of Eq. (31) is

$$\int_{\Omega} w\, v\, d\xi d\eta = \int_{\Omega} [c(\xi) \int_{\beta}^{1} \frac{sds}{(s^2-\beta^2)^{1/2}} (\int_{o}^{s} \frac{\Delta p(f,t)}{(s^2-f^2)^{1/2}} df)]v\, d\xi d\eta \tag{33}$$

Eqs. (32) and (33) can now be discretized in the domain Ω by expressing

$$\Delta P(\xi,\eta,t) = \phi_i(\xi,\eta)\Delta P^i(t)$$

$$w(\xi,\eta,t) = \phi_i(\xi,\eta)w^i(t)$$

and use of the Galerkin approach to obtain

$$K_{ij}(\Delta P(t),W(t))\Delta P^j(t) + G_{ij}\dot{W}^j(t) + F_i(t) = 0 \tag{34}$$

$$G_{ij}W^j(t) - C_{ij}\Delta P^j(t) = 0 \tag{35}$$

where

$$K_{ij} = \int_{\Omega} \lambda(W^m\phi_m)^{2+r}[\frac{1}{L^2}(\Delta P^k \frac{\partial\phi_k}{\partial\xi})^2 + \frac{1}{H^2}(\Delta P^\ell \frac{\partial\phi_\ell}{\partial\eta})^2]^{1/2(r-1)}$$

$$x \{\frac{1}{L^2}\frac{\partial\phi_i}{\partial\xi}\frac{\partial\phi_j}{\partial\xi} + \frac{1}{H^2}\frac{\partial\phi_i}{\partial\eta}\frac{\partial\phi_j}{\partial\eta}\} d\xi d\eta$$

$$C_{ij} = \int_{\Omega} [C(\xi) \int_{\beta}^{1} \frac{sds}{(s^2-\beta^2)^{1/2}} (\int_{o}^{s} \frac{\phi_i}{(s^2-f^2)^{1/2}} df)]\phi_j d\xi d\eta$$

$$G_{ij} = \int_{\Omega} \phi_i\phi_j\, d\xi d\eta$$

and

$$F_i = \int_{\Omega} \frac{2C}{(t-\tau)^{1/2}} \phi_i\, d\xi d\eta - \frac{Q_2}{L}\int \phi_i ds$$

For the solution techniques, a one-step integration scheme is considered, i.e. a discrete algorithm which couples only two successive time values of the unknown. In this scheme, for each time interval, the time rate of change of $\underset{\sim}{W}$ at a particular time t_* is given by

$$\dot{\underset{\sim}{W}}_* = \frac{1}{\Delta t}(\underset{\sim}{W}_{n+1} - \underset{\sim}{W}_n)$$

with $t_* = (1-\alpha)t_n + \alpha t_{n+1} \qquad \alpha \in (0,1)$.

Moreover, the dependent variables at t_* are expressed by

$$\Delta \underset{\sim}{P}_* = (1-\alpha)\Delta \underset{\sim}{P}_n + \alpha \Delta \underset{\sim}{P}_{n+1}$$

$$\underset{\sim}{W}_* = (1-\alpha)\underset{\sim}{W}_n + \alpha \underset{\sim}{W}_{n+1}$$

Re-writing Eqs. (34) and (35) with the preceding approximations and $\alpha=1$, we have

$$K_{ij}\ \Delta P^j_{n+1} + \frac{G_{ij}}{\Delta t}\ W^j_{n+1} + H^i_{n+1} = 0 \tag{36}$$

$$G_{ij}\ W^j_{n+1} - C_{ij}\Delta P^j_{n+1} = 0 \tag{37}$$

Hence, Eqs. (36) and (37) at the (n+1) time step are given by

$$Y_i = K_{ij}\Delta P^j + \frac{G_{ij}}{\Delta t}\ W^j + H^i = 0$$

$$R_i = G_{ij}\ W^j - C_{ij}\Delta P^j$$

where $H^i = F^i(t) - \dfrac{G_{ij}\ W^j_n}{\Delta t}$

Using the curtailed Taylor series expansion for Y_i and R_i in the above, we obtain

$$\begin{bmatrix} \dfrac{\partial Y_i}{\partial W_\ell} & \dfrac{\partial Y_i}{\partial (\Delta P_\ell)} \\ \dfrac{\partial R_i}{\partial W_\ell} & \dfrac{\partial R_i}{\partial (\Delta P_\ell)} \end{bmatrix} \begin{bmatrix} \Delta \underset{\sim}{W}_\ell \\ \Delta(\Delta \underset{\sim}{P}_\ell) \end{bmatrix} = -\begin{Bmatrix} \underset{\sim}{Y}_i \\ \underset{\sim}{R}_i \end{Bmatrix} \tag{38}$$

Solution of Eqs. (38) yields $\Delta \underset{\sim}{W}_\ell$ and $\Delta(\Delta \underset{\sim}{P}_\ell)$, and hence $\underset{\sim}{W}_\ell$ and $\Delta \underset{\sim}{P}_\ell$ can be obtained from $\underset{\sim}{W}^{m+1} = \underset{\sim}{W}^m + \Delta \underset{\sim}{W}^m$, and $\Delta P^{m+1} = \Delta \underset{\sim}{P}^m + \Delta(\Delta \underset{\sim}{P}^m)$.

After obtaining the nodal values of the pressure, either the critical stress intensity factor approach or the concept of equilibrium fracture

propagation, advanced by Barenblatt, and used by Geertsma and De Klerk [5] can be used to establish the equilibrium height profile $h(\xi)$ for a specified fracture extent L at a given time t. The iterative procedure, therefore, entails the solution of $\underset{\sim}{W}$ and $\Delta\underset{\sim}{P}$ for a specified initial length L_o and selected height $h(\xi)$ equilibrium profile (based either on the Geertsma-De Klerk formulation or specified fracture toughness). The correct profile $h(\xi)$ is then determined iteratively and the solution process then marches with time.

2.3 Formulations for Fracture Height Prediction - Bi-material Cases

The preceding formulations are applicable to homogeneous, isotropic elastic media. To extend this work to bi-material fracture response prediction with an arbitrary variation in tectonic stresses and/or joint effects, sophisticated finite element simulations are necessary.

When the crack front terminates at a bi-material interface, the power of the stress/strain singularity is no longer (-1/2) but (-p), $(0<p<1)$, where p is a function of the elastic constants and the crack orientation. The procedure proposed by Akin [58] has been modified to solve various bi-material fracture problems, wherein the original eight-noded quadratic quadrilateral element is degenerated to quadratic triangular element. To maintain the correct degeneration, the shape function of the mid-side node across the collapsed corner is modified. This procedure utilizes a local function, ϕ^p where $\phi(\xi,\mu)=1-N_1(\xi,\mu)$, ξ,μ are local co-ordinates, N_1 is the regular interpolation function associated with the singular point, and the element family is derived from standard isoparametric elements. The singular element displacement field u is

$$u(\xi,\mu) = \sum_{i=1} H_i^*(\xi,\mu)u_i \tag{39}$$

where

$$H_i(\xi,\mu) = 1-W^{1-p}(\xi,\mu) \ , \ H_i^*(\xi,\mu) = N_i^*(\xi,\mu)W^{-p}(\xi,\mu) \quad 2\leq i\leq 8$$

$$N_k^* = \frac{1}{2} N_k \{(1+\xi\xi_k) + (1+\mu\mu_k)\} \ , \ N_j^*=N_j \qquad j\neq k$$

and k is the mid-side node.

The above formulation has been numerically calibrated for crack opening displacements and stresses by considering several bi-material crack problems in fracture mechanics literature for composites prior to its application to problems in hydraulic fracturing [59].

In addition, finite element formulations for the J integral [60] and associated path independent integrals [61,62] for bi-material problems have been developed to predict fracture containment, penetration, and interfacial crack propagation for several models [63].

3.0 NUMERICAL EXPERIMENTS

In this section, numerical simulations for the prediction of hydraulic fracture geometry and associated response variables, based on the preceding finite element formulations, are presented. Selected results are also presented in Appendix A titled "Finite Element Model Simulations Associated with Hydraulic Fracturing."

3.1 Fracture Width, Length, and Stress Intensity Model Simulations

Prior to presenting the numerical results from the formulations in Section 2.1, previously deduced expressions for the fracture width and half fracture length are presented for illustration and numerical comparison.

The Perkins-Kern [3] - Nordgren [4] formulations, with vertical plane dominating stiffness and elliptical vertical cross-section, yield

$$W(0,t) = 4\left[\frac{2\mu(1-\nu)Q_2^2}{\pi^3 GHC}\right]^{1/4} t^{1/8} \tag{42}$$

$$L(t) = Q_2\, t^{1/2} / \pi HC \tag{43}$$

for large t and/or C.

On the other hand, the equations derived by Geertsma and De Klerk [5] based on horizontal cross-sectional analysis and the concept of equilibrium fracture propagation is

$$W(0,t) = \left[\frac{84(1-\nu)\mu Q_2 L^2(t)}{\pi GH}\right]^{1/4} \tag{44}$$

$$L(t) = \frac{Q_2 W(0,T)}{16\pi C^2}\left[\frac{2\beta}{\pi 1/2} - 1 + e^{\beta^2}\ \text{erfc}\ \beta\right] \tag{45}$$

where $W(0,T) \cong 1.5W(0,t)$, $\beta = 8Ct^{1/2}/\pi^{1/2}\, W(0,T)$, and $W(0,T)$ designates the bore hole fracture width when the pump stops at time T.

Figure 4 illustrates the maximum width versus time comparisons at the bore hole for Newtonian and non-Newtonian frac fluid properties using the hydraulic fracture data indicated in Fig. 6. Computed crack pressure profiles, transient fracture lengths, and stress intensity factors are revealed in Figs. 5, 6, and 7, respectively.

Selected results, using the iterative leak-off modification presented in Section 2.1, are presented in Reference [65]. Using this refinement, comparisons for the Ostego, Michigan Welch #1-15 experiments have been made with the following parameters:
$Q = 6.4$BPM ($1.02\ m^3$/min), $C = 0.002$ ft/$\sqrt{\text{min}}$ (0.00061 m$\sqrt{\text{min}}$), $H = 72$ ft (21.95 m), $\nu = 0.2$, $G = 1.2 \times 10^6$ psi (8.27GPa), $\mu = 46$ cp, $n' = 1$ (0.000767 Pa min), $K = 1$ mD, and injection time $T = 45$ minutes.

The fracture widths, lengths, and leak-offs using the $C/(t-\tau)^{1/2}$ and unspecified leak-off representations compare favorably (within 10%) for this case with the cumulative leak-off approaching 80% of the injected volume. A comparison of the leak-off results from the Perkins-Kern [3] - Nordgren[4] formulation and the unspecified leak-off case is shown in Fig. 8.

3.2 Fracture Width and 2D Vertical Fracture Configuration Model Simulations

The finite element formulations presented in Section 2.2 are applicable to general hydraulic fracture configuration prediction with either the critical stress intensity factor approach or the concept of equilibrium fracture propagation incorporated. To simplify presentation of the numerical results, the vertical fracture configuration is assumed to be elliptical with simultaneous critical stress intensity criteria posed at extreme locations of the major and minor axes of the elliptical crack in a manner

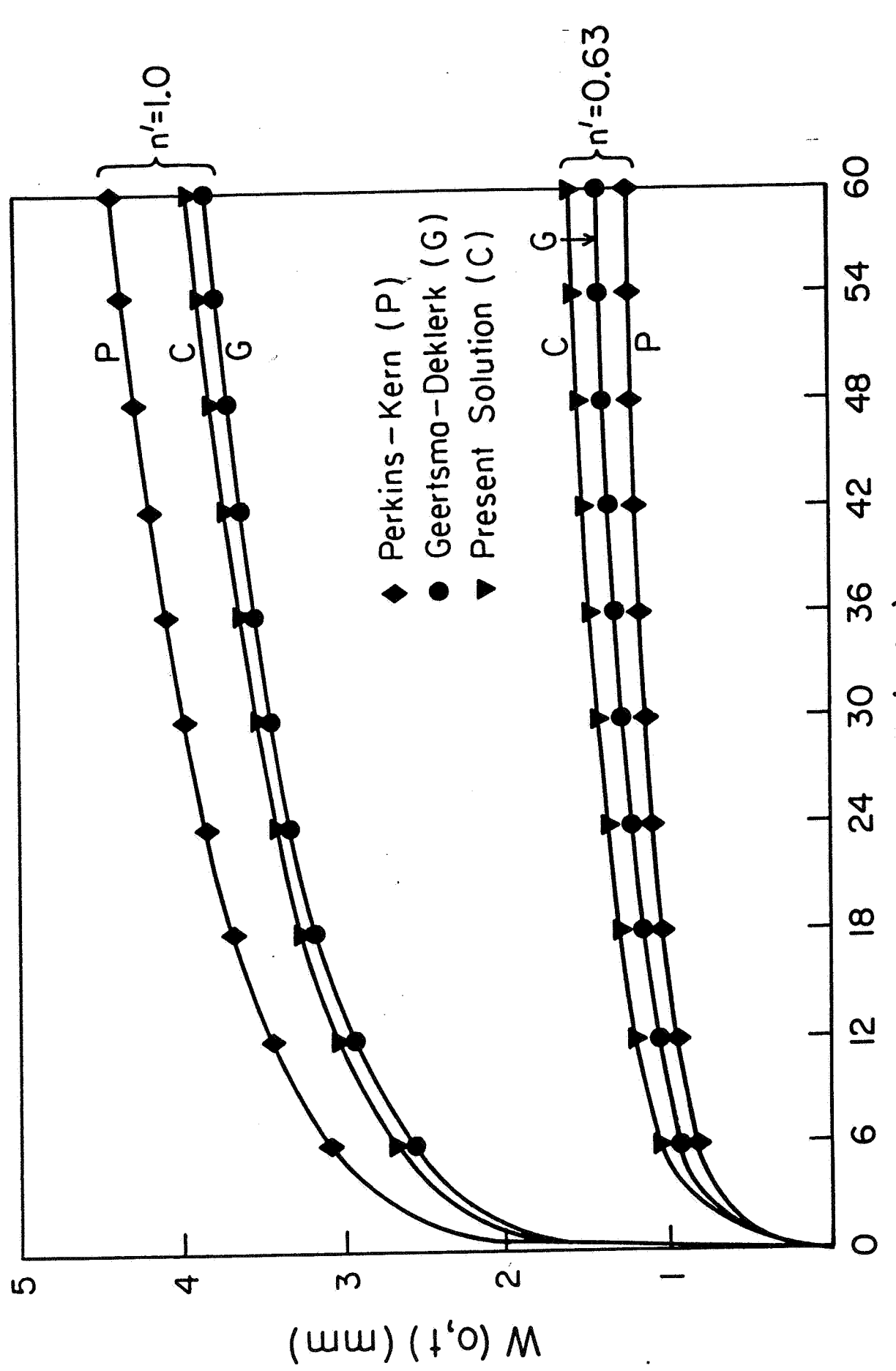

Figure 4: Borehole Width Versus Time Comparisons for Hydraulic Fracture Parameters in Figure 6

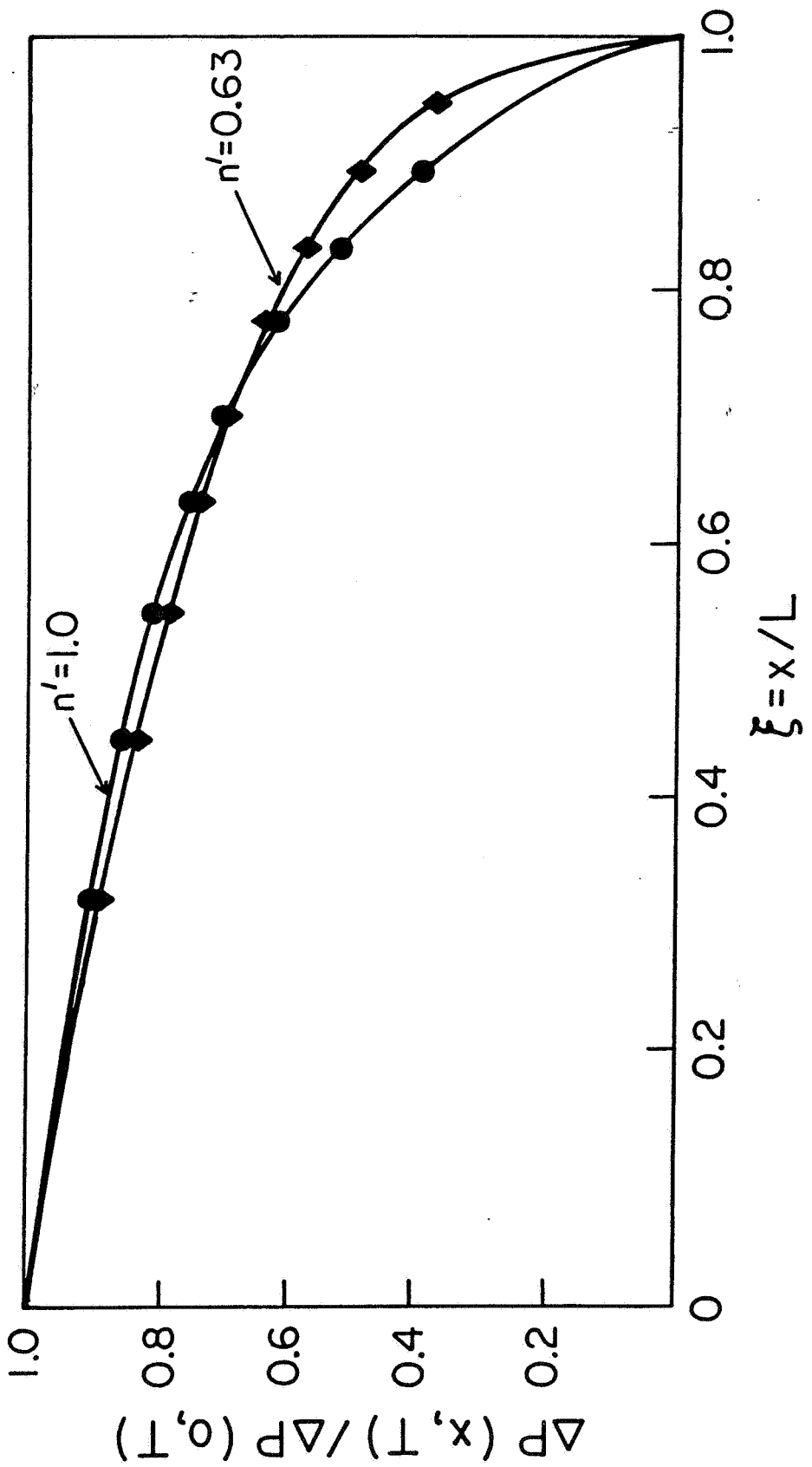

Figure 5: Crack Pressure Profile Comparisons for Hydraulic Fracture Parameters in Figure 6

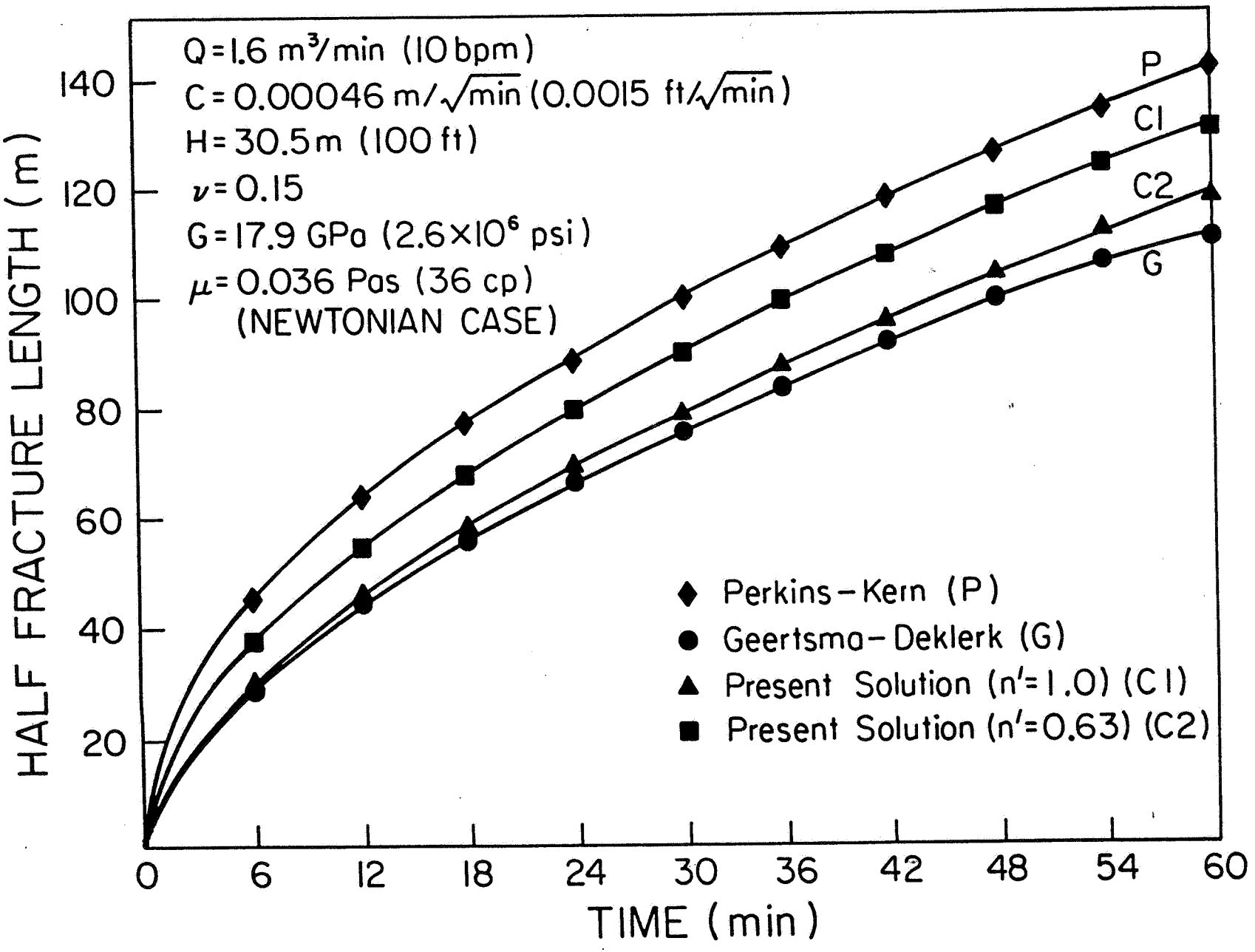

Figure 6: Transient Half Fracture Length Comparisons

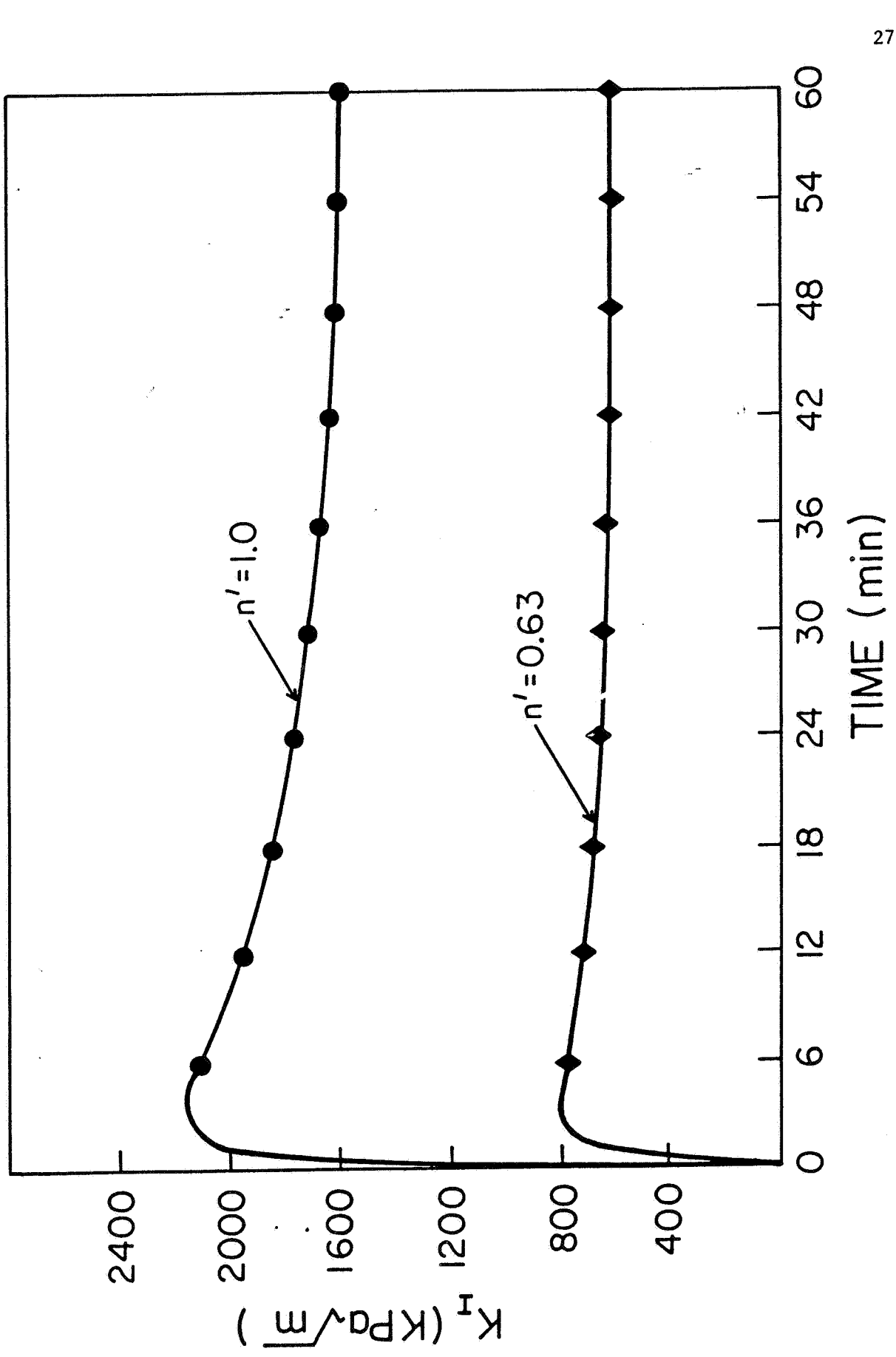

Figure 7: Stress Intensity Factor Versus Time Plots for Hydraulic Fracture.Parameters in Figure 6

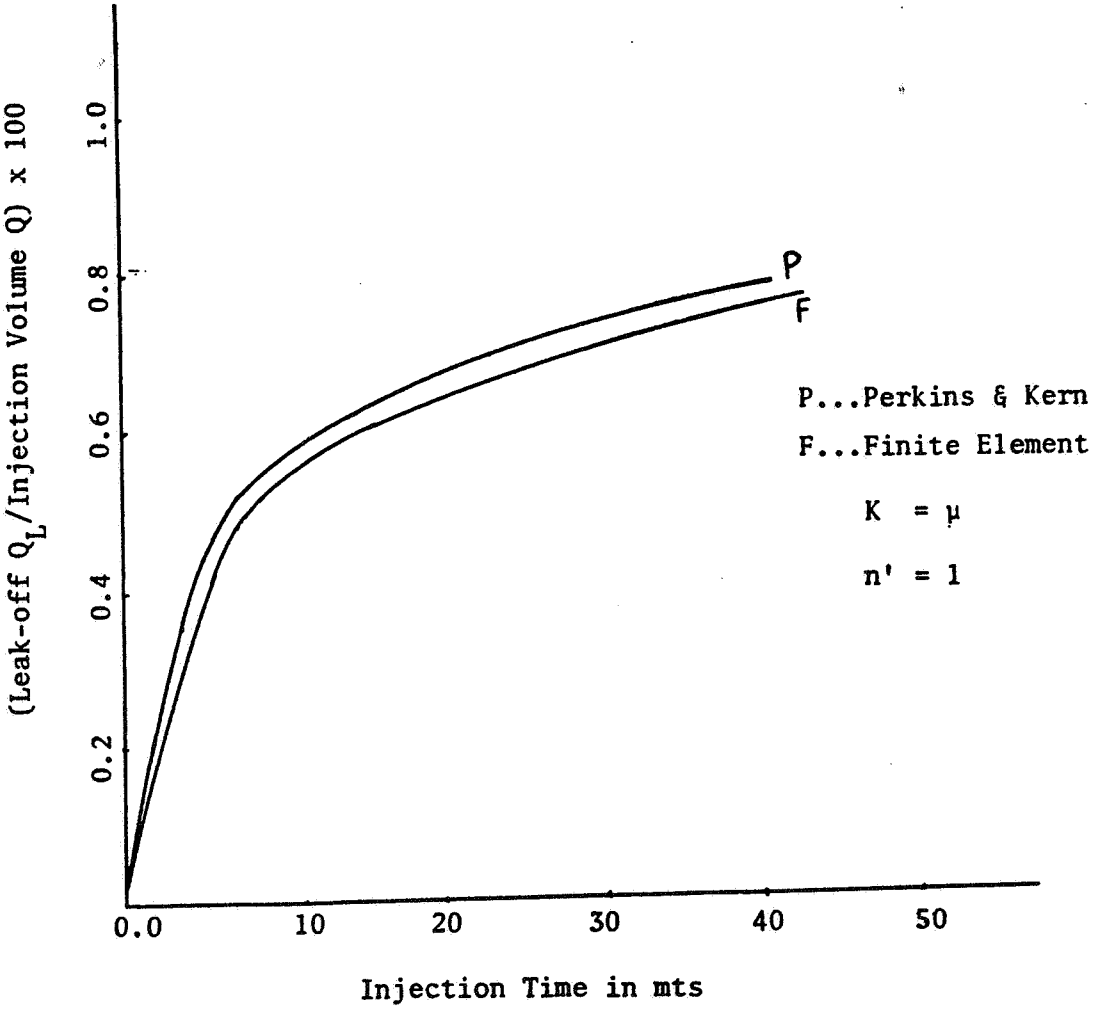

Figure 8: Comparison of percentage of leakoff to injection volume.

similar to Palmer and Carroll [26]. After obtaining the nodal values of the pressure and width with an initially assumed geometry, a least squares technique is used to fit the crack pressure p(x,y) to the cubic equation, in the form

$$p(x,y) = A_{oo} + A_{10}x + A_{01}y + A_{20}x^2 + A_{11}xy + A_{02}y^2 + A_{30}x^3 + A_{21}x^2y + A_{12}xy^2 + A_{03}y^3$$

This pressure distribution is supplied as an input for the analytical computations of the crack opening mode stress intensity factors at the intersection points of the major and minor axes with the ellipse. An iterative procedure with modified fracture geometry, using the governing field equations, is adopted until these stress intensity values are equal to the critical stress intensity factor.

For purposes of numerical comparison, the hydraulic fracture parameters used here are the same as those selected in Section 3, namely: Flow rate Q = 1.58 m^3/min (10 BPM), loss coefficient C = 0.00046 m/$min^{1/2}$ (0.0015 ft/$min^{1/2}$), Poisson's ratio ν=0.15, Shear modulus G = 17.9 GPa (2.6 x 10^6psi), Consistency index K' = 0.0006 Nmin/m^2 (36 cp), flow behavior index n' = 1. In addition, a fracture toughness of 2.2 MPa$\sqrt{m}$ (2000 psi$\sqrt{in}$) is employed in the preliminary numerical simulations.

Figures 9 and 10 illustrate the time dependent growth of the minor and major axes of the elliptical crack. The corresponding transient configurations are revealed in Fig. 11.

Figures 12 and 13 show the width profiles at three time instants along the minor and major axes, respectively, and the corresponding pressure plots are shown in Figs. 14 and 15. It should be emphasized that these presented evaluations are preliminary in nature and refinements of the model formulations and numerical techniques are in progress.

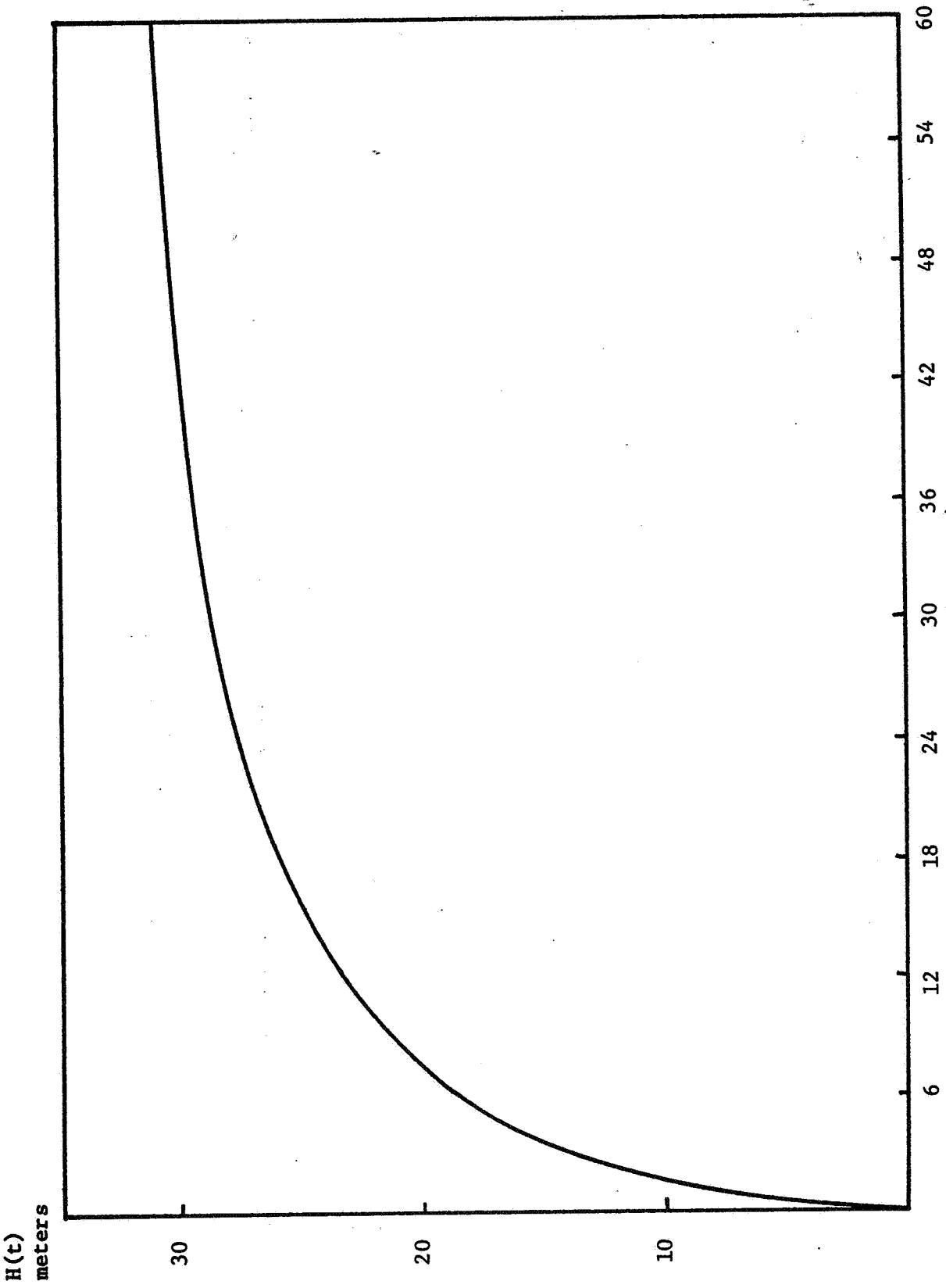

Figure 9. Elliptical Crack Minor Axis Versus Time

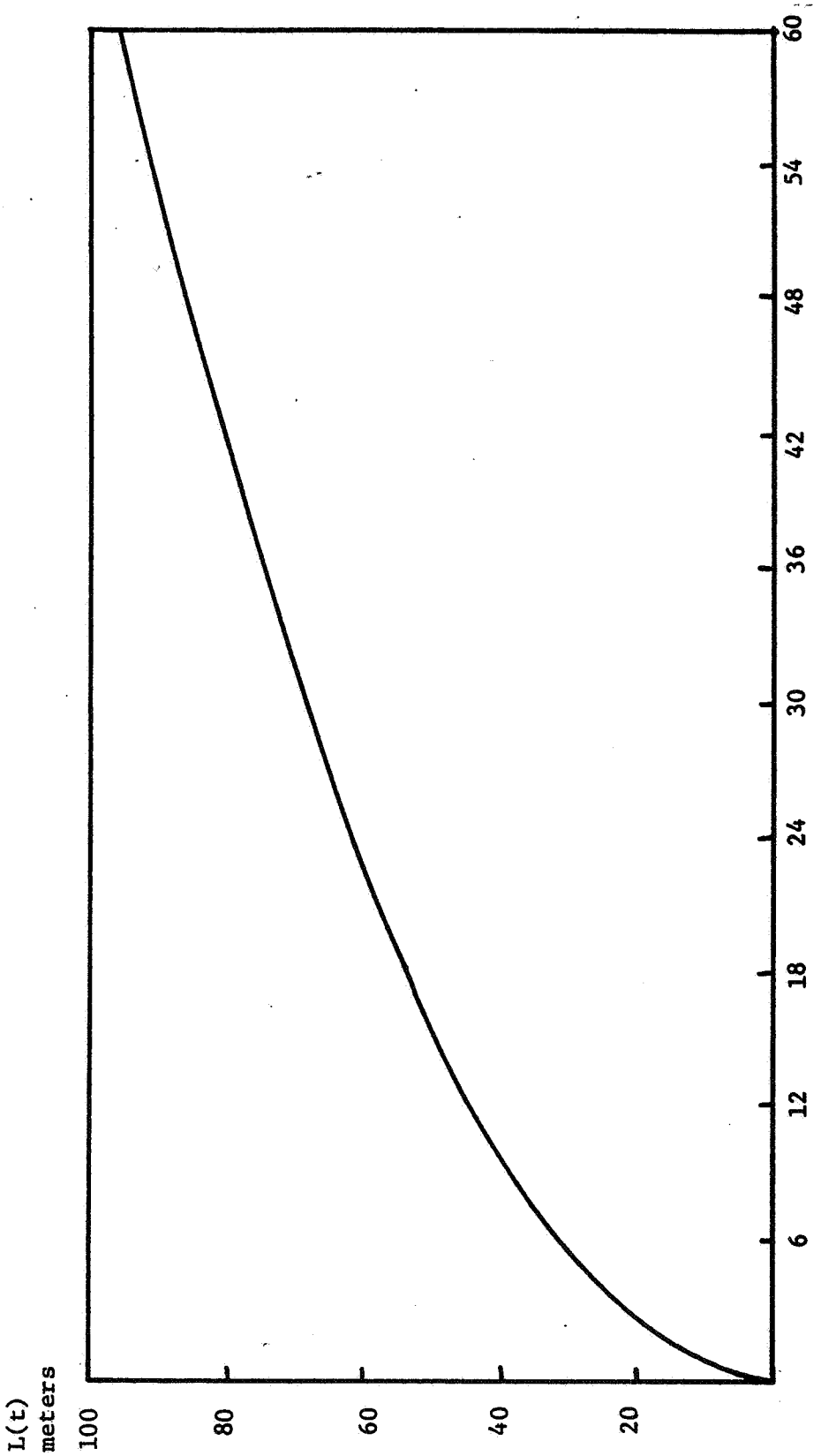

Figure 10. Elliptical Crack Major Axis Versus Time

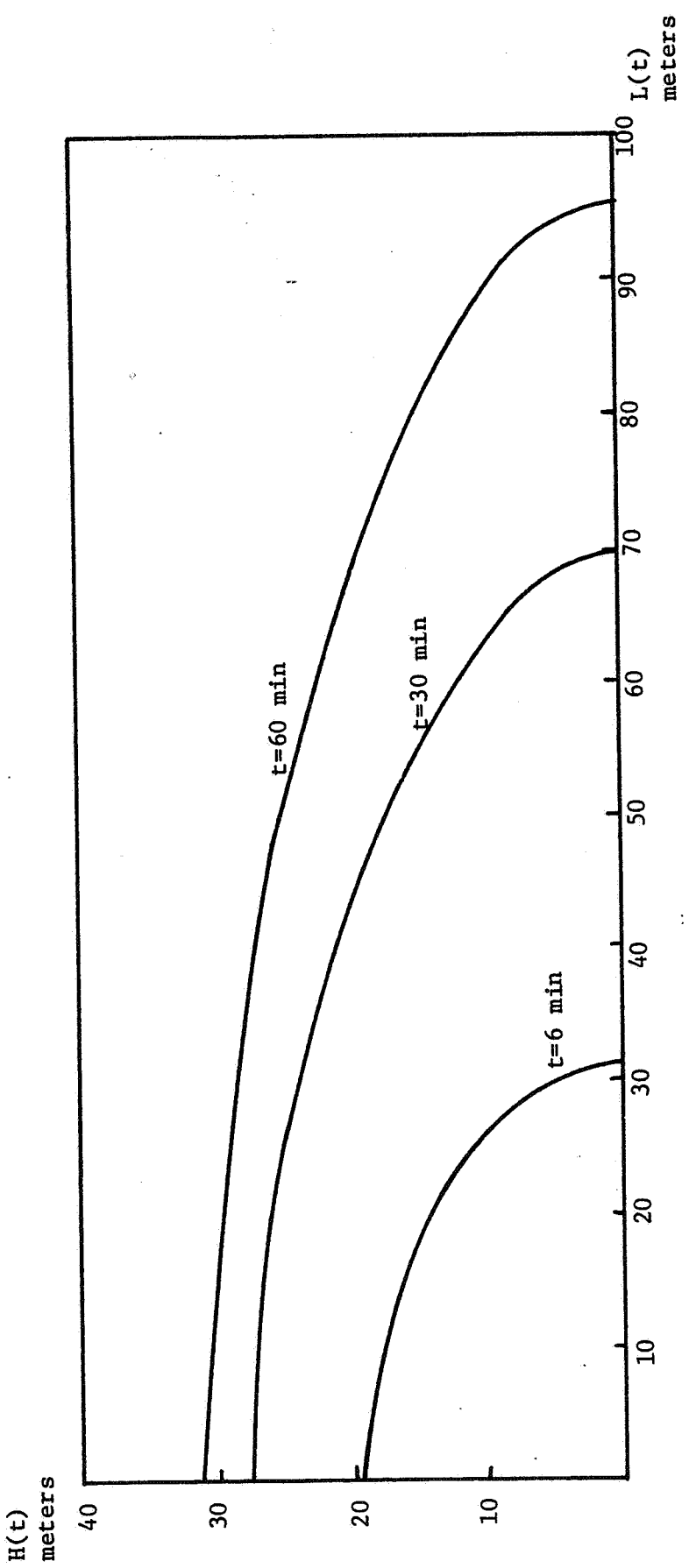

Figure 11. Elliptical Crack Transient Configuration

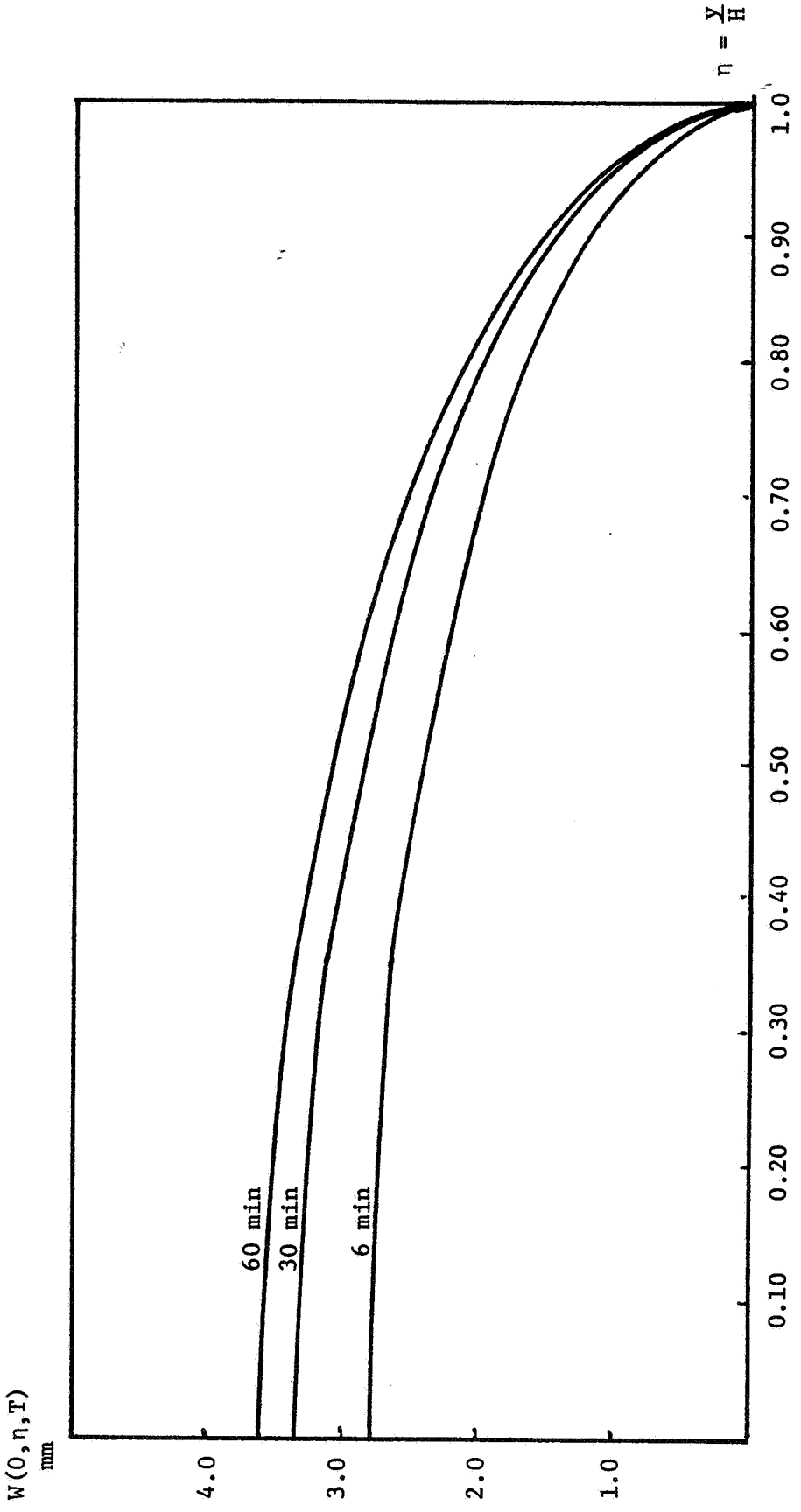

Figure 12. Fracture Width Versus Time Along Elliptical Crack Minor (Borehole) Axis

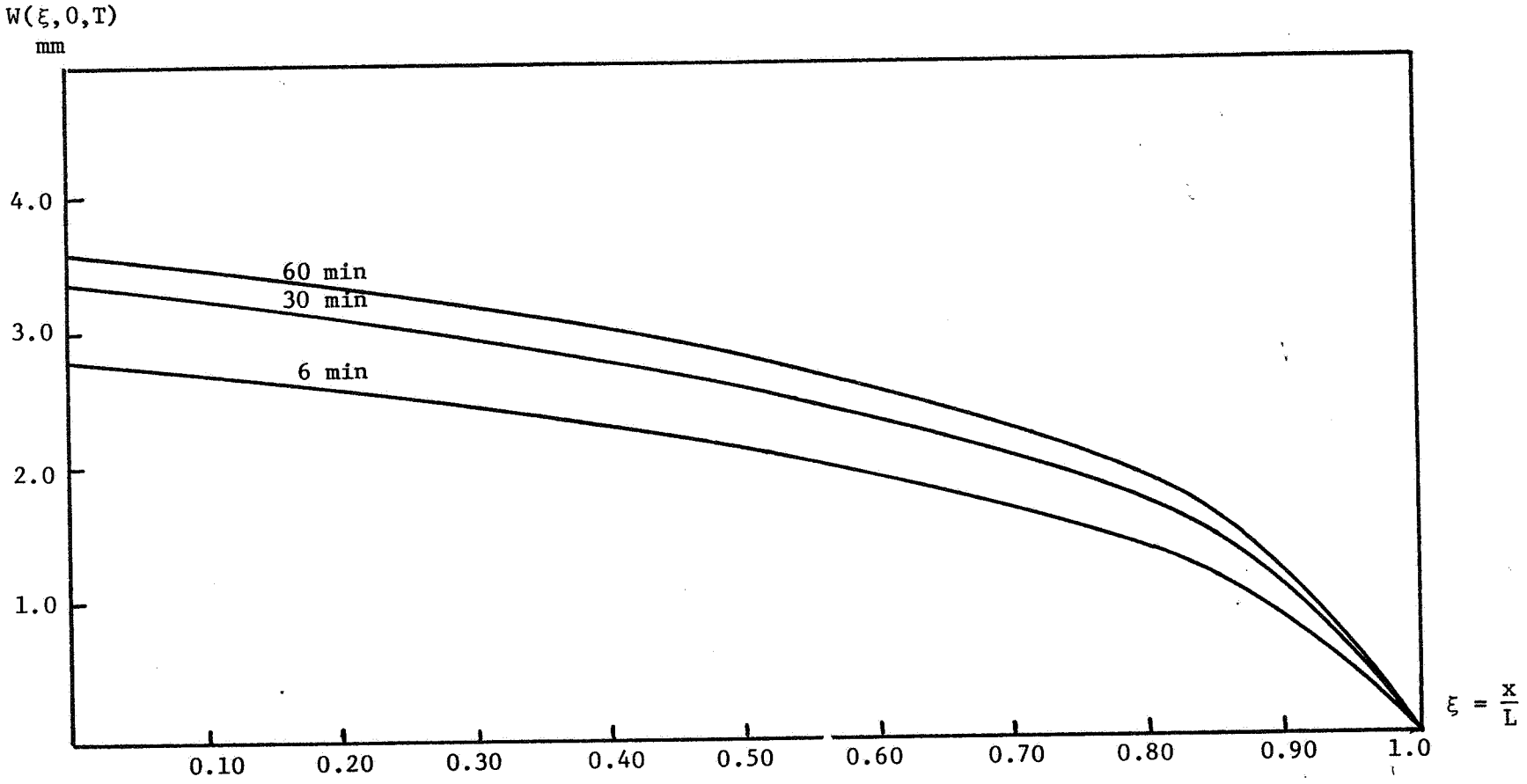

Figure 13. Fracture Width Versus Time Along Elliptical Crack Major Axis

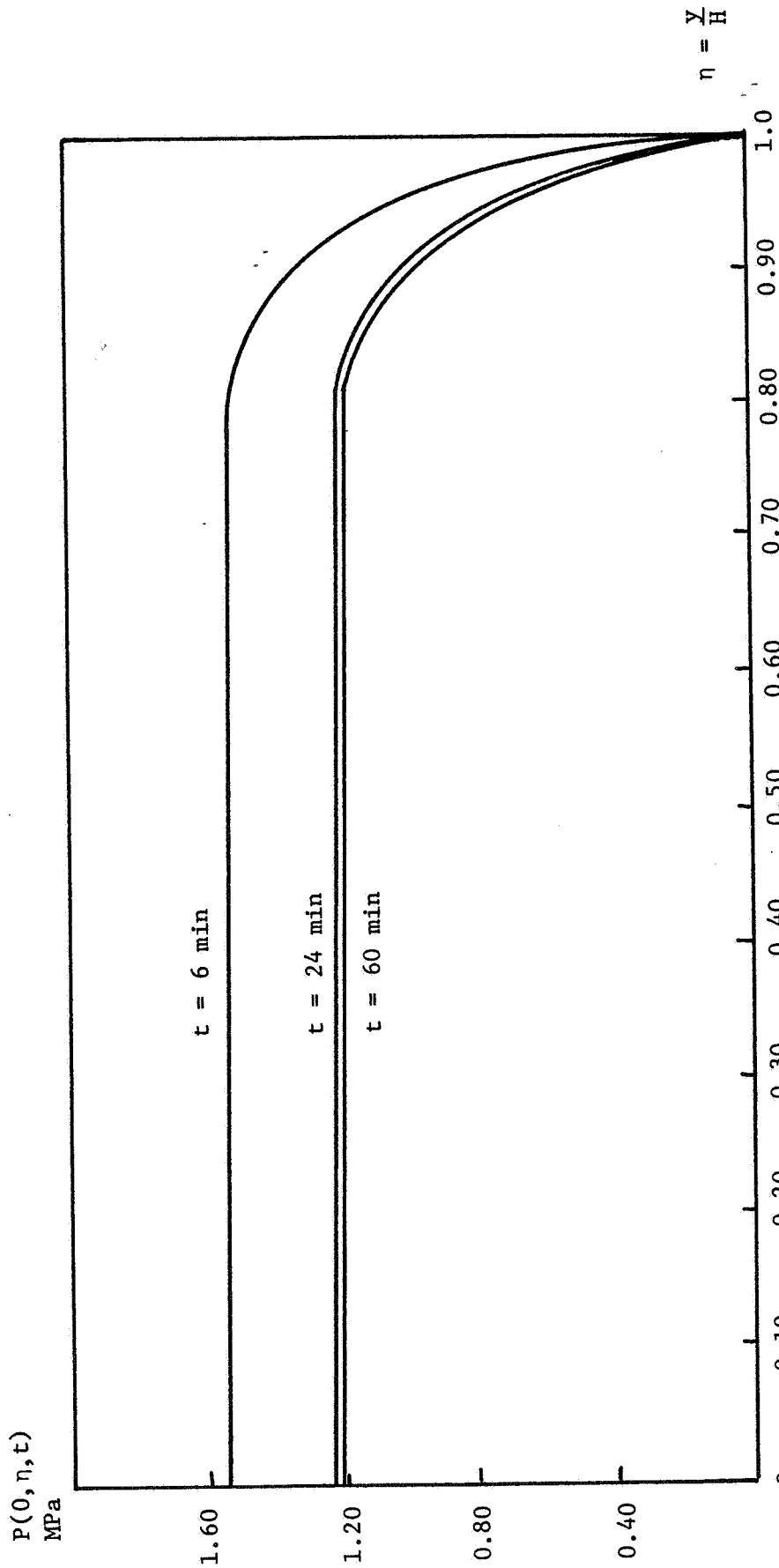

Figure 14. Effective Crack Pressure Versus Time Along Elliptical Crack Minor (Borehole) Axis

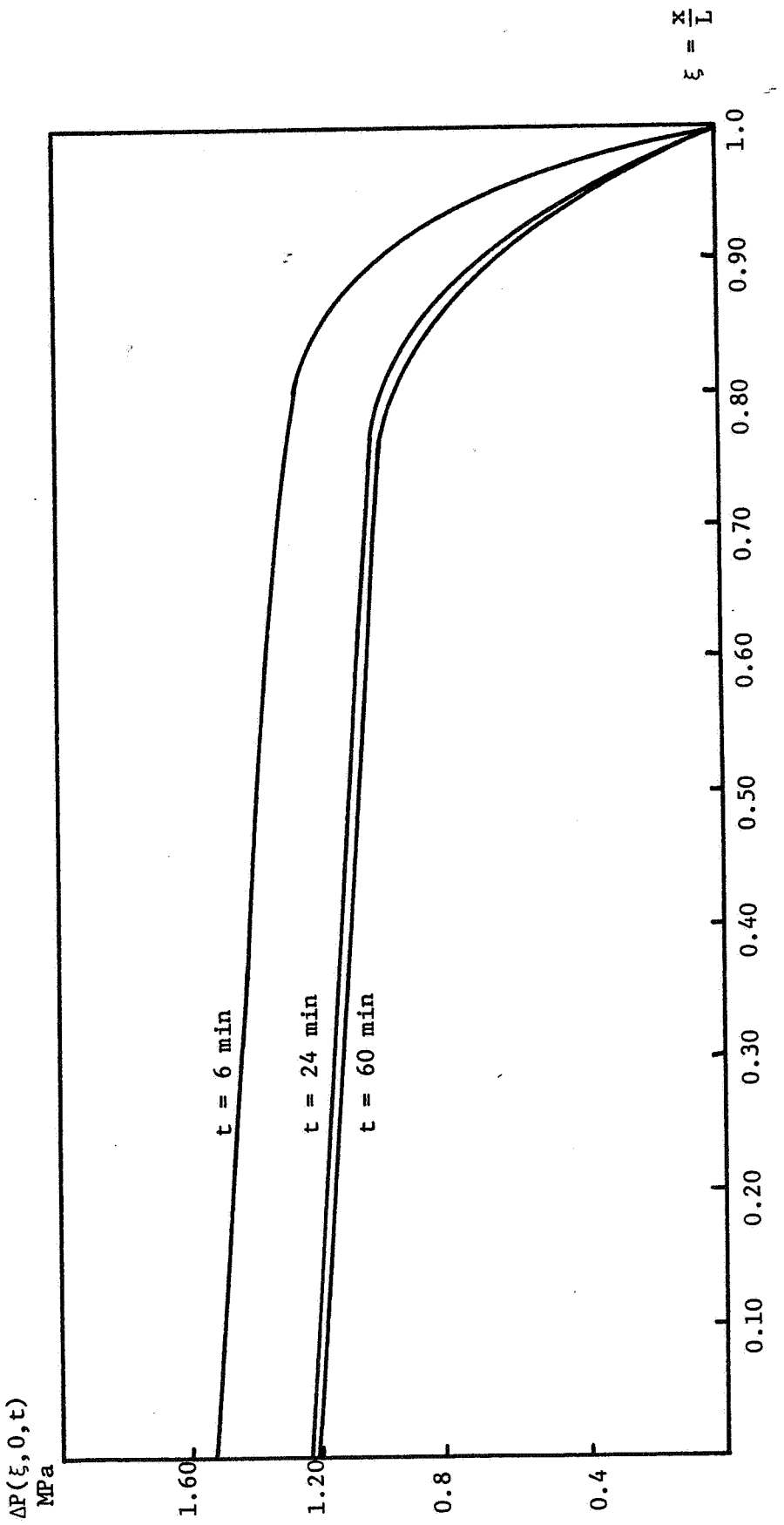

Figure 15. Effective Crack Pressure Versus Time Along Elliptical Crack Major Axis

3.3 Bi-Material Response Simulations

Pertinent finite element results for vertical fracture height prediction including the effects of multi-layering and differential in-situ stresses across the layers along with dendritic fracture applications are presented in Appendix A. In addition, the analytical development of an interface element, for potential use in problems dealing with the interaction of induced fractures with joints, is presented in Appendix B. In this section, calibrative results for bi-material interface problems are initially presented along with associated design data for predicting crack tip stress intensity factors. Also, the problem of interaction of a vertical fracture with a horizontal joint is numerically investigated using the finite element methodology presented in Section 2.3.

Current research and experimental studies have shown that in situ stresses, interface bond strength, internal friction coefficient, and relative fracture toughness are important factors in fracture containment design. Calibrative response results, with a perfectly bonded bi-material interface, for a pressurized crack terminating at the interface are compared against known solutions [65] for an epoxy-aluminum pair (Figs. 16,17). Similarly, for the interfacial crack model, a calibrative comparison of the strain energy release rate ($\partial U/\partial a$) versus crack shear modulus ratio m is shown in Fig. 18. The energy release rate is computed by evaluating the associated path independent J integral. Good estimates for the crack opening displacement and the stress intensity factors K_I and K_{II} have also been obtained. With these basic models, the computed stress intensity factors or associated energy release rates provide design information for vertical fracture penetration, arrest or interfacial propagation.

The effects of the differences in in situ stresses and material properties are studied by utilizing the geometry in the above calibrative

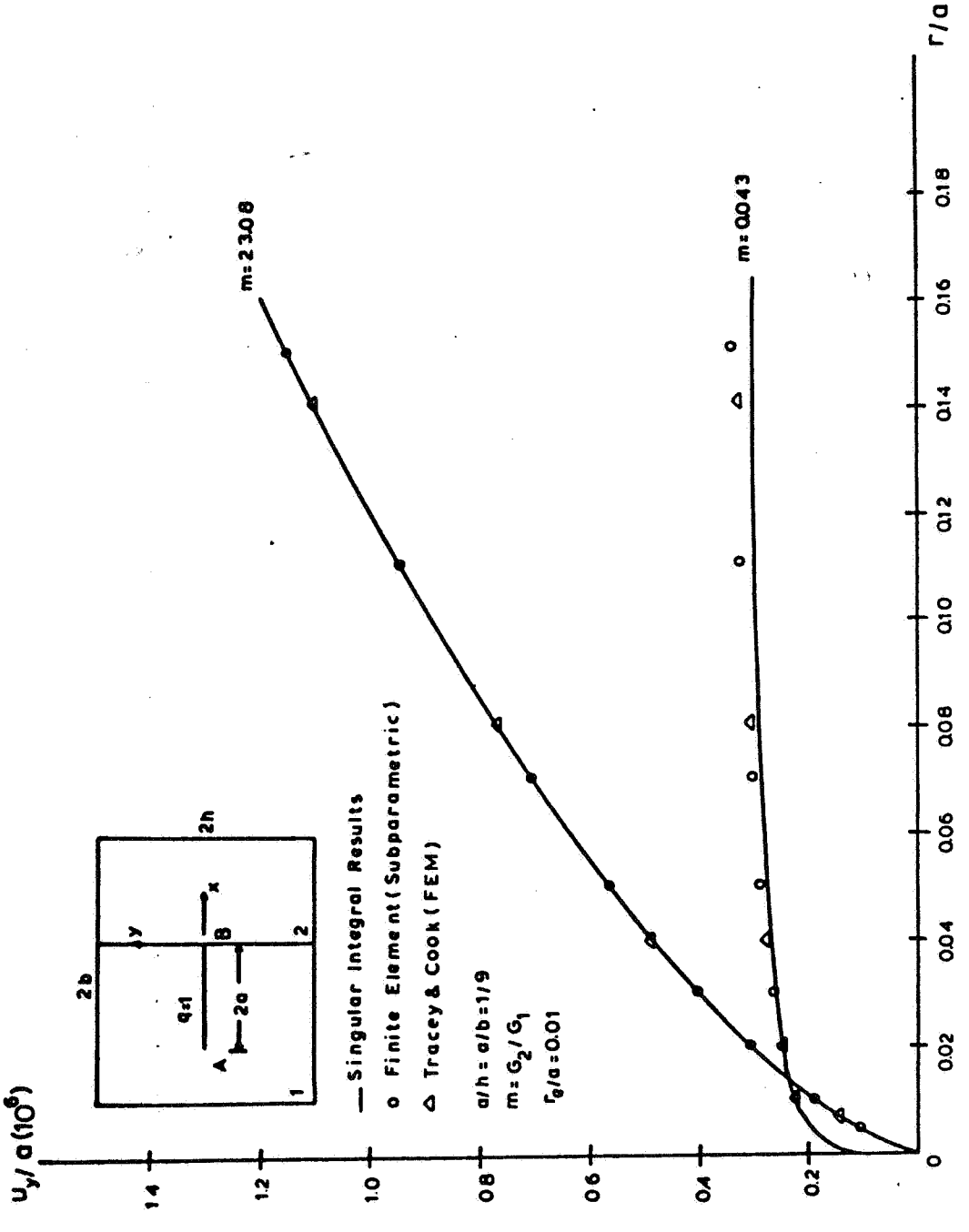

Crack Opening Displacement vs. r/a

Figure 16: Pressurized Crack Opening Displacement Comparison for Aluminum-Epoxy Pair

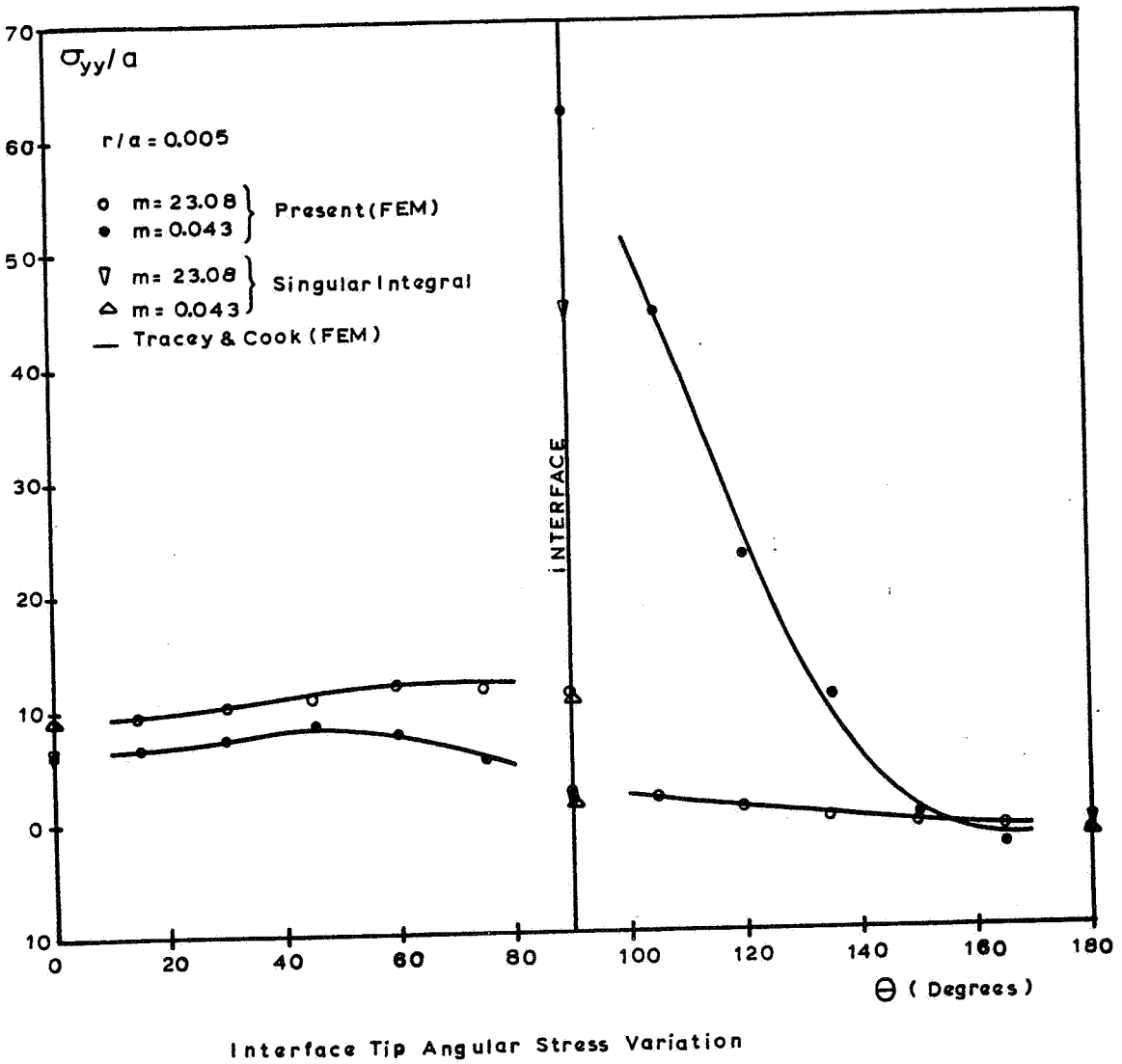

Figure 17: Comparison of Interface Tip Angular Stress Variation for Aluminum-Epoxy Pair

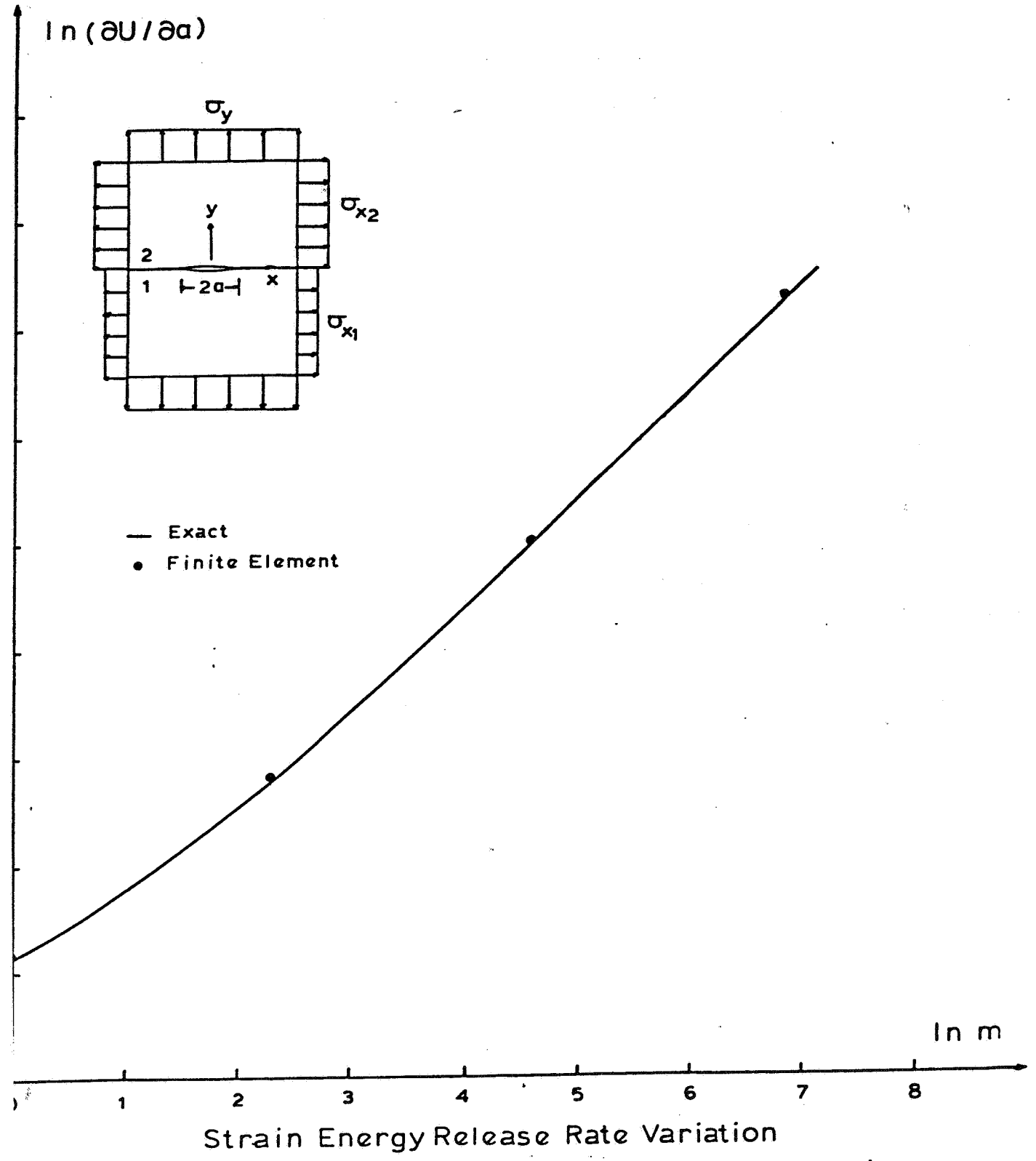

Figure 18: Comparison of Strain Energy Release Rate versus $m=G_2/G_1$ for Interfacial Crack Problem

examples with plane strain conditions. Figure 19 illustrates the superposed normalized stress intensity factors at the bi-material tip induced by a pressurized crack and different in situ stresses in the payzone and adjacent layer for different shear moduli ratios m. Corresponding stress intensity factors for different ratios of σ_2/σ_1 are revealed in Fig. 20.

An application of the stress intensity and J integral results for a pressurized crack plane strain coal-overburden model has been presented in Reference [65]. Effective critical bottom hole pressure ratios p_2/p_1 (i.e. pressure for bi-material penetration/pressure for isotropic material propagation) have been obtained using the criterial stress intensity factor and bi-material J integral criteria. For a plexiglass-resin sandwich model with the crack in the plexiglass layer, Biot et al [47] have permanently demonstrated that the ratio p_2/p_1 is approximately 2.0. From their simplified elasticity theory solution, a pressure ratio of 1.24 can be deduced. The J-integral analysis for this bi-material case yields a comparable value of 1.31, also considerably lower than the experimental case from the condition

$$\frac{p_2}{p_1} = \left[\frac{(J_{1c})_2}{(J_{1c})_1} \frac{J_{homogeneous}}{J_{bi\text{-}material}}\right]^{1/2}$$

Additional refinements of the J integral approach and comparisons with available data are being conducted by Gurdogan [63].

As a final application, the response of a pressurized crack intersecting a joint (Fig. 21) is evaluated. The joint is assumed to behave as an interfacial crack and the pressurized crack runs perpendicular to the joint at its midpoint. Triangular quarter point elements are used to model the lower crack tip, and subparametric semi-radial singularity elements are employed

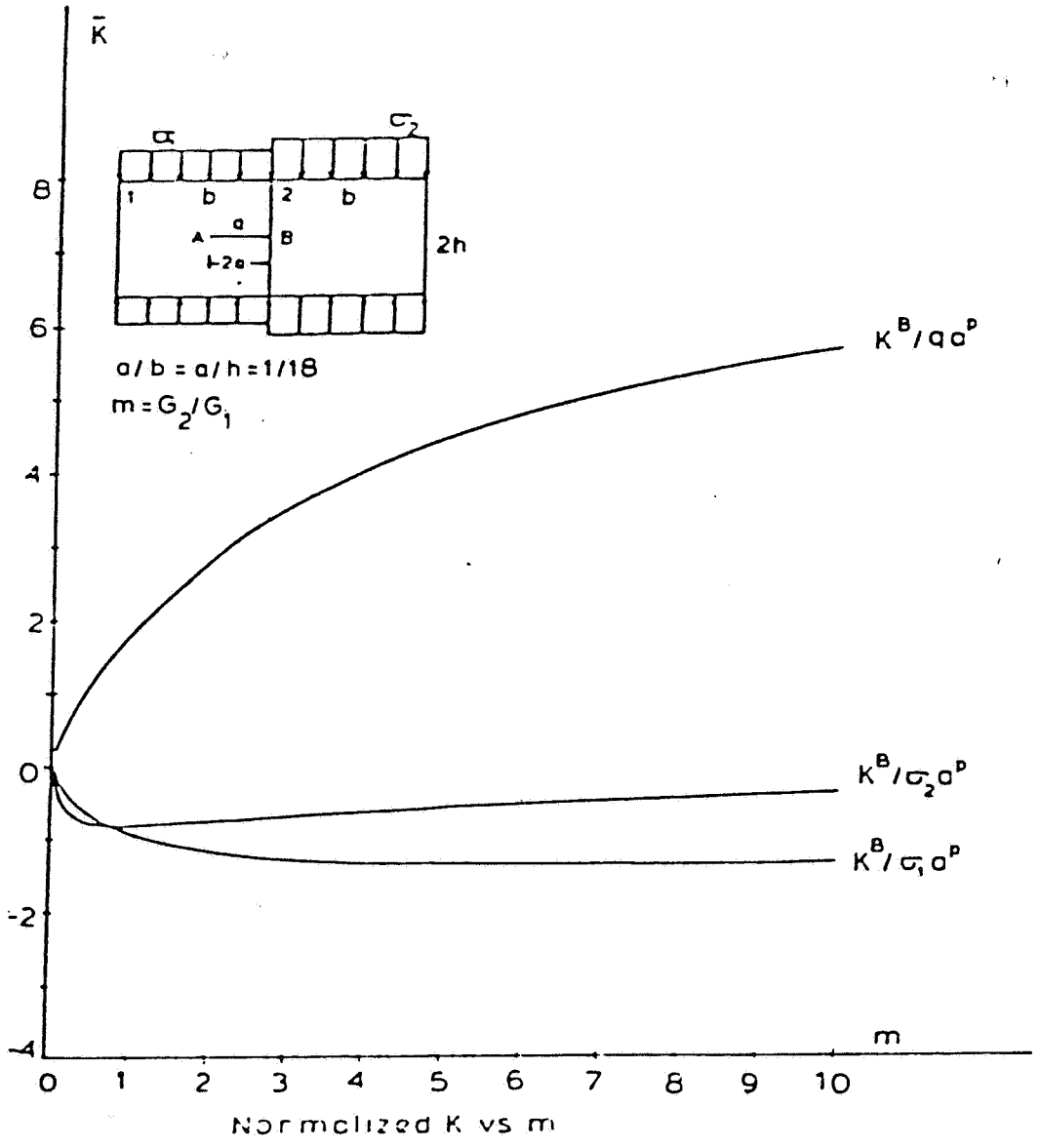

Figure 19: Non-Dimensionalized Mode I Stress Intensity Factor versus m for Pressure and In Situ Stress Loadings

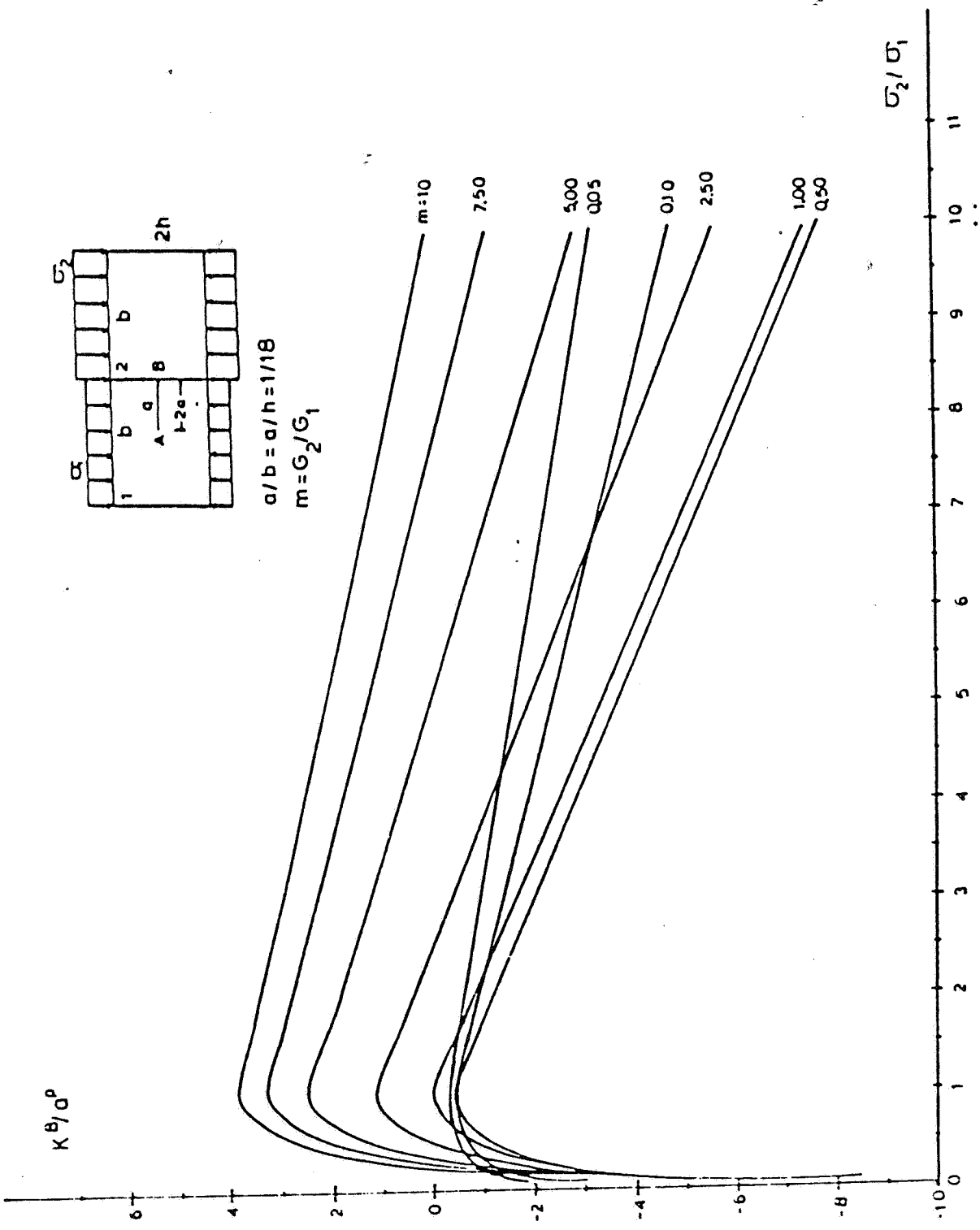

Figure 20: Non-Dimensionalized Mode I Stress Intensity Factors versus In Situ Stress Ratio for Different m

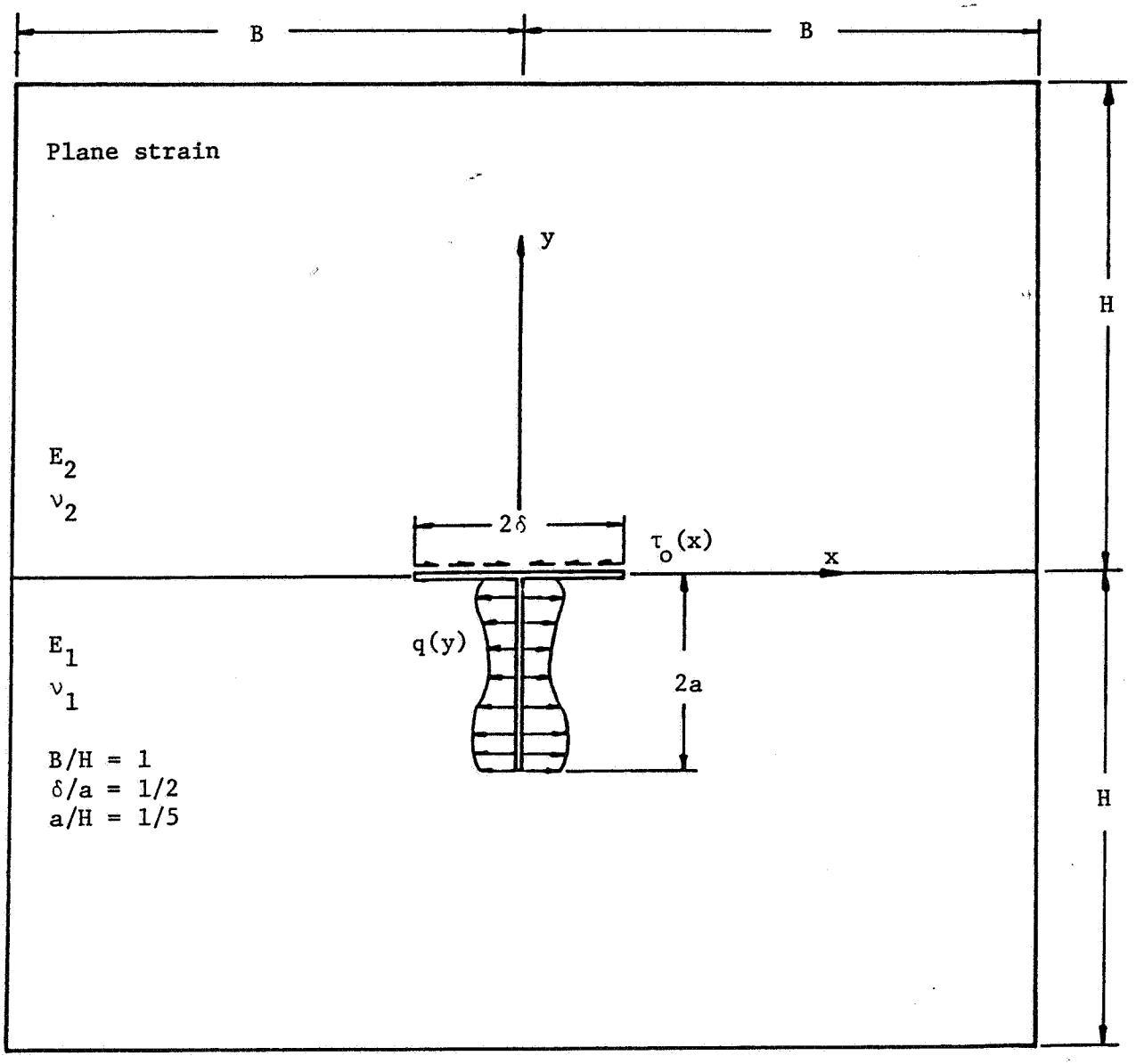

Figure 21. Pressurized Crack Intersecting a Joint.

at the interfacial crack tip region. Following Keer and Chen [67], relative slip is assumed to occur in the joint and the shear tractions in the joint are assumed to have the form $\tau(x) = \tau_o x$. This linear behavior reflects the loss of frictional resistance due to the frac fluid leakage in the joint. The crack opening pressure, $q(y)$ is assumed to have the form

$$q(y) = d + ey \qquad 0 \geq y \geq -L$$

where d is the effective crack pressure and e is the effective pressure gradient.

For certain values of d, e and τ_o, the crack may propagate at the lower tip and/or be accompanied by interfacial slipping. For zero stress intensity factors at the lower tip, these values are [67]; d=1.0000, e=0.3333, and $\tau_o = 0.5920$ with $(\alpha,\beta) = (0.5, 0)$. Here, α and β are Dundurs' material constants defined by

$$\alpha = \frac{m(1-\nu_1)-(1-\nu_2)}{m(1-\nu_1)+(1+\nu_2)} \quad , \quad \beta = \frac{m(1-2\nu_1)-(1-2\nu_2)}{2(m(1-\nu_1)+(1-\nu_2))}$$

The case $(\alpha,\beta) = (0,0)$ represents the homogeneous case.

A comparison of the obtained non-dimensionalized crack opening displacement profile with the results presented by Keer and Chen [67] is illustrated in Fig. 22. The analysis for predicting the joint crack tip propagation is conceptually similar to that presented in Appendix A for the primary-secondary crack interaction problem associated with dendritic fracturing.

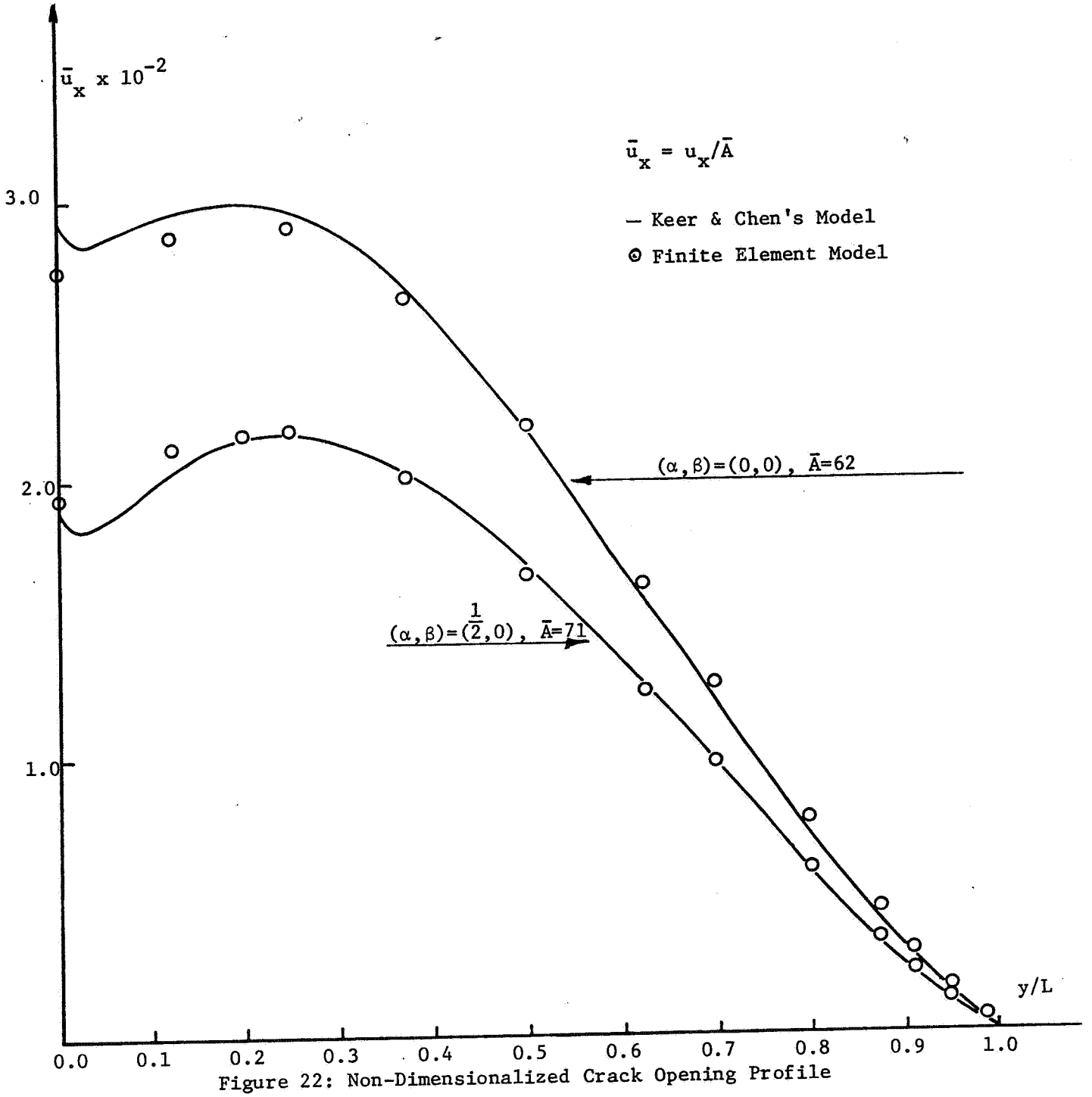

Figure 22: Non-Dimensionalized Crack Opening Profile

4.0 DISCUSSION AND CONCLUSIONS

The elliptical fracture numerical simulations for the isotropic case demonstrate the influence of fracture height growth as a result of two-dimensional crack fluid flow. Figure 23 reveals the cumulative frac fluid leak off for the constant height and elliptical fracture models for the parameters employed in Sections 3.1 and 3.2. For the same injected fluid volume, the fracture volume for the elliptical crack case is larger than the corresponding constant height model. Also, the crack effective pressure for the constant height case increases with elapsed time while it decreases with time for the elliptical crack model. These finite element simulations can be extended to cases with multilayering and differential in situ stresses across layers by employing the methodology and finite element results in Sections 2.3, 3.3 and Appendix A. The judicious use of the developed "anisotropy" scaling factors in terms of in situ stress differentials and adjacent layer property ratios can provide realistic design predictions for fracture configurations in three layered media.

Problems associated with induced vertical crack interaction with natural joint and fracture systems present a formidable challenge. In particular, interface/joint characterization experiments with well defined local friction properties are necessary for a detailed prediction of vertical fracture arrest, penetration or interfacial propagation. The studies presented in Sections 3.3, Appendix A and Appendix B provide numerical strategies for potential incorporation in generalized hydraulic fracture simulation models with complex geometry prediction capabilities in multi-layered media. To the authors' best knowledge, state-of-the-art simulators are in their infancy from the vantage point of modeling layers with multiple inclusions (such as sand lenses) with variable formation

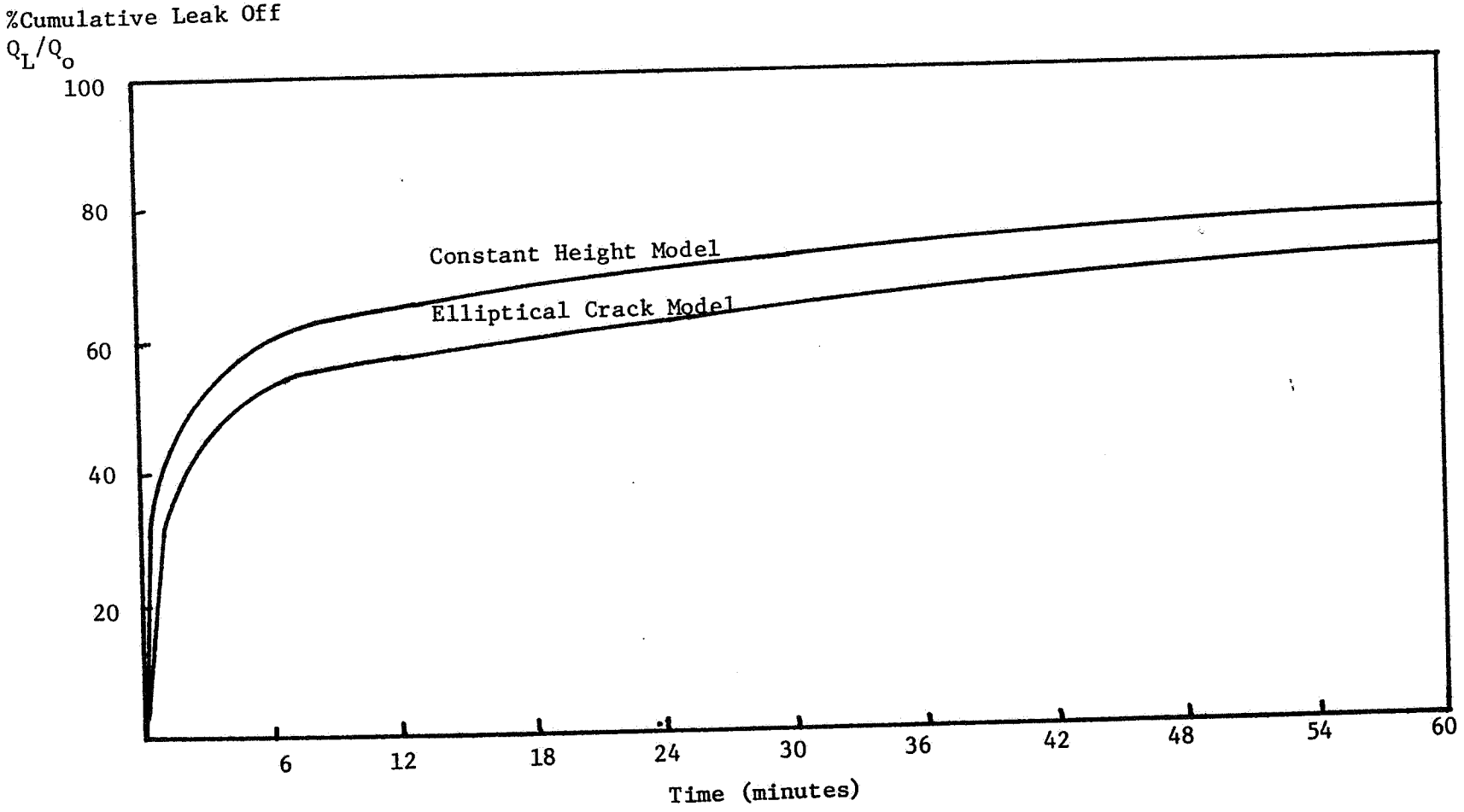

Figure 23. Percentage Cumulative Leak-Off Versus Time for Constant Height and Elliptical Crack Models

permeabilities, mechanical properties, in situ stress fields, and fracture systems.

In conclusion, the coupling of a hydraulic fracture simulator with a reservoir flow simulator is highly desirable. In this context, a preliminary formulation dealing with the effect of vertical fracture height on transient well flow behavior is presented in Appendix C. Detailed studies incorporating the effects of the induced fracture(s), natural frequencies, and reservoir flow are essential for the development of comprehensive simulators and commercial stimulation treatments.

5.0 REFERENCES

1. Yu.P. Zheltov and S.A. Kristianovitch, "The Hydraulic Fracturing of an Oil-Producing Formation," Isvest. Aked. Nauk SSSR, Otel Tekh Nauk, No. 3, 41, 1955.

2. R.D. Carter, "Derivation of the General Equation for Estimating the Extent of the Fractured Area," Appendix to "Optimum Fluid Characteristics for Fracture Extension," by G. Howard and C. Fast, Drill. and Prod. Prac., API, pp. 261-270, 1957.

3. T.K. Perkins and L.R. Kern, "Widths of Hydraulic Fractures," J. Pet. Tech., 937, 1961.

4. R.P. Nordgren, "Propagation of a Vertical Hydraulic Fracture," Soc. Pet. Eng. J., 12, 306, 1972.

5. J. Geertsma and F. deKlerk, "A Rapid Method of Predicting Width and Extent of Hydraulically Induced Fractures," J. Pet. Tech., 1571, 1969.

6. A.A. Daneshy, "On the Design of Vertical Hydraulic Fractures," J. Pet. Tech., 83, 1973.

7. J. Geertsma and R. Haafkens, "A Comparison of the Theories for Predicting Width and Extent of Vertical Hydraulically Induced Fractures," Journal of Energy Resources Technology, ASME, 101, 8, 1979.

8. B. Haimson and C. Fairhurst, "Initiation and Extension of Hydraulic Fractures in Rocks," Soc. Pet. Eng. J., 7, 310, 1967.

9. M.S. Seth and K.E. Gray, "Transient Stresses and Displacements Around a Wellbore due to Fluid Flow in Transversely Isotropic Porous Media: I, II, Infinite Reservoirs," Soc. Pet. Eng. J., 8, 63, 1968.

10. H.Y. Wong and I.W. Farmer, "Hydrofracture Mechanisms in Rock During Pressure Grouting," Rock Mechanics, 5, 21, 1973.

11. L.Z. Shuck and S.H. Advani, "Induced Stresses in Hydraulic Fracturing Operations," Proceedings 15th Conference on Rock Mechanics, ASCE Publication, 93, 1975.

12. J.R. Rice and M.P. Cleary, "Some Basic Stress Diffusion Solutions for Fluid-Saturated Elastic Porous Media with Compressible Constituents," Reviews of Geophysics and Space Physics, 14, 227, 1976.

13. A. Ruina, "Influence of Coupled Deformation-Diffusion Effects on the Retardation of Hydraulic Fracture," Proceedings 19th U.S. Symposium on Rock Mechanics, 274, 1978.

14. E.R. Simonsen et.al., "Containment of Massive Hydraulic Fractures," Society of Petroleum Engineers, Inc., Paper No. SPE6088, 1976.

15. S.H. Advani et.al., "Hydraulic Fracture Modeling for the Eastern Gas Shales Project," Proc. 2nd Eastern Gas Shales Symposium, METC/SP-76/6, Vol. I, Morgantown, 84, 1978.

16. M.P. Cleary, "Primary Factors Governing Hydraulic Fractures in Heterogeneous Stratified Porous Formations," ASME Paper No. 78-PET-47, 1978.

17. S.H. Advani and J.K. Lee, "Finite Element Model Simulations Associated with Hydraulic Fracturing," Soc. Pet. Eng. J., 22, 209, 1982.

18. A.A. Daneshy, "Hydraulic Fracture Propagation in Layered Formations," Society of Petroleum Engineers, Inc., Paper No. SPE6088, 1976.

19. H.A. Van Eekelen, "Hydraulic Fracture Geometry: Fracture Containment in Layered Formations," Society of Petroleum Engineers of AIME, Paper No. SPE9261, 1980.

20. M.E. Hanson et.al., "Theoretical and Experimental Research on Hydraulic Fracturing," Journal of Energy Resources Technology, ASME, 102, 92, 1980.

21. R.J. Clifton and A.S. Abou-Sayed, "A Variational Approach to the Prediction of the Three-Dimensional Geometry of Hydraulic Fractures," Proc. 1981 SPE/DOE Symposium on Low Permeability Gas Reservoirs, Paper No. SPE/DOE 9879, 1981.

22. M.P. Cleary, "Comprehensive Design Formulae for Hydraulic Fracturing," Society of Petroleum Engineers of AIME, Paper No. SPE 9529, 1980.

23. M.P. Cleary, "Analysis of Mechanisms and Procedures for Producing Favorable Shapes of Hydraulic Fractures," Society of Petroleum Engineers of AIME, Paper No. SPE 9260, 1980.

24. E.N. Mastrojannis et.al., "Growth of Planar Cracks Induced by Hydraulic Fracturing," International Journal of Numerical Methods in Engineering, 15, 41, 1980.

25. I.D. Palmer and H.B. Carroll, Jr., "3D Hydraulic Fracture Propagation in the Presence of Stress Variation," Proceedings Unconventional Gas Recovery Symposium, Paper No. SPE/DOE 10849, 1982.

26. I.D. Palmer and H.B. Carroll, Jr., "Numerical Solution for Height and Elongated Fractures," Proc. 1983 SPE/DOE Symposium on Low Permeability Gas Reservoirs, Paper No. SPE/DOE 11627, 1983.

27. N.R. Warpinski et.al., "Laboratory Investigation on the Effect of In Situ Stresses on Hydraulic Fracture Containment," Proceedings 1981 SPE/DOE Symposium on Low Permeability Gas Reservoirs, Paper No. SPE/DOE 9880, 1981.

28. M.B. Rubin, "Experimental and Theoretical Study of Hydraulic Fracturing in Impermeable and Permeable Materials," Final Report, SRI International, Contract No. AC-21-79 MC11597, 1981.

29. A. Settari and M.P. Cleary, "Three-Dimensional Simulation of Hydraulic Fracturing," Society of Petroleum Engineers of AIME, Paper No. SPE 10504, 1982.

30. A. Settari and M.P. Cleary, "Development and Testing of a Pseudo-Three-Dimensional Model of Hydraulic Fracture Geometry," Society of Petroleum Engineers of AIME, Paper No. SPE 10505, 1982.

31. M.P. Cleary et.al., "Development of a Fully Three-Dimensional Simulator for Analysis and Design of Hydraulic Fracturing," Proc. 1983 SPE/DOE Symposium on Low Permeability Gas Reservoirs, Paper No. SPE/DOE 11631, 1983.

32. M.P. Cleary et.al., "Microcomputer Models for the Design of Hydraulic Fractures," Proc. 1983 SPE/DOE Symposium on Low Permeability Gas Reservoirs, Paper No. SPE/DOE 11628, 1983.

33. H.O. McLeod, Jr., "A Simplified Approach to Design of Fracturing Treatments Using High Viscosity Cross-Linked Fluids," Proc. 1983 SPE/DOE Symposium on Low Permeability Gas Reservoirs, Paper No. SPE/DOE 11614, 1983.

34. R.H. Nilson and S.K. Griffiths, "Numerical Analysis of Hydraulically-Driven Fractures," Computer Methods in Applied Mechanics and Engineering, 36, 359, 1983.

35. M.A. Biot et.al., "A Two-Dimensional Theory of Fracture Propagation," Society of Petroleum Engineers of AIME, Paper No. SPE 11607, 1982.

36. R.W. Veatch, Jr., "Overview of Current Hydraulic Fracturing Design and Treatment Technology," Parts 1 and 2, Journal of Petroleum Technology, May 1983, 669-687, June 1983, 853-864.

37. A.I. Horton, "Comparative Analysis of Stimulations in the Eastern Gas Shales," Morgantown Energy Technology Center Report DOE/METC-145, 1981.

38. "Western Gas Sands Project" Status Reports for FY 82/1, 82/2, 82/3, Bartlesville Energy Technology Center, U.S. Department of Energy, 1982-83.

39. N.R. Warpinski et.al., "In Situ Stresses: The Predominant Influence on Hydraulic Fracture Containment," Proc. 1980 SPE/DOE Symposium on Unconventional Gas Recovery, Paper No. SPE/DOE 8932, 1980.

40. J.F. Cuderman, "Multiple Fracturing Experiments - Propellant and Borehole Considerations," Proc. 1982 SPE/DOE Symposium on Unconventional Gas Recovery, Paper No. SPE/DOE 10845, 1982.

41. D.A. Northrop et.al., "Multi-Well Experiment: A Field Laboratory for Tight Gas Sands," Proc. 1983 SPE/DOE Symposium on Low Permeability Gas Reservoirs, Paper No. SPE/DOE 11646, 1983.

42. "Confirmation Field Tests Workshop," Gas Research Institute, Chicago, Illinois, Feb. 1983.

43. L.W. Teufel and J.A. Clark, "Hydraulic Fracture Propagation in Layered Rock: Experimental Studies of Fracture Containment," Proc. 1981 SPE/DOE Symposium on Low Permeability Gas Reservoirs, Paper No. SPE/DOE 9878, 1981.

44. G.D. Anderson, "Effects of Friction on Hydraulic Fracture Growth Near Unbonded Interfaces in Rocks," Soc. Pet. Eng. J., 21, 21, 1981.

45. M. Rubin, "Experimental Study of Hydraulic Fracturing in an Impermeable Material," in press, Journal of Energy Resources Technology, June 1983.

46. A. Ingraffea, "Mixed Mode Fracture Initiation in Indiana Limestone and Westerly Granite," Proc. 22nd U.S. Symposium on Rock Mechanics, 186, 1981.

47. M.A. Biot et.al., "Laboratory Experiments in Fracture Propagation," Society of Petroleum Engineers of AIME, Paper No. SPE 10377, 1981.

48. V.H. Kenner et.al., "A Study of Fracture Toughness for an Isotropic Shale," Issues in Rock Mechanics, 23rd U.S. Symposium on Rock Mechanics, AIME, Chap. 60, 586, 1982.

49. R.A. Schmidt, "A Microcrack Model and Its Significance to Hydraulic Fracturing and Fracture Toughness Testing, The State of the Art in Rock Mechanics," 21st U.S. Symposium on Rock Mechanics, U. of Missouri-Rolla, 581, 1980.

50. J.M. Papadopoulos et.al., "Laboratory Simulations of Hydraulic Fracturing," Proc. 1983 SPE/DOE Symposium on Low Permeability Gas Reservoirs," Paper No. 11618, 1983.

51. K.G. Nolte, "Determination of Fracture Parameters from Fracture Pressure Decline," Society of Petroleum Engineers, Inc., Paper No. SPE 8341, 1980.

52. E.J. Novotny, "Proppant Transport," Society of Petroleum Engineers, Inc., Paper No. SPE 6813, 1977.

53. P.E. Clark and J.A. Quadir, "Prop Transport in Hydraulic Fractures: A Critical Review of Particle Settling Velocity Equations," Proc. 1981 SPE/DOE Symposium on Low Permeability Gas Reservoirs, Paper No. SPE/DOE 9866, 1981.

54. P.E. Clark and N. Güler, "Prop Transport in Vertical Fractures: Settling Velocity Correlations," Proc. 1983 SPE/DOE Symposium on Low Permeability Gas Reservoirs, Paper No. SPE/DOE 11636, 1983.

55. A. Settari, "A New General Model of Fluid Loss in Hydraulic Fracturing," Proc. 1983 SPE/DOE Symposium on Low Permeability Gas Reservoirs, Paper No. SPE/DOE 11625, 1983.

56. J.N. Reddy and V.D. Murty, "Finite-Element Solution of Integral Equations Arising in Radiative Heat Transfer and Laminar Boundary-Layer Theory," Numerical Heat Transfer, 1, 389, 1978.

57. O.C. Zienkiewicz and J.C. Heinrich, "The Finite Element Method and Convection Problems in Fluid Mechanics," in Finite Elements in Fluids, Vol. 3, Editors R.H. Gallagher et.al., John Wiley and Sons, Ch. 1, 1-22, 1978.

58. J.E. Akin, "The Generation of Elements with Singularities," International Journal of Numerical Methods in Engineering, 10, 1249, 1976.

59. D.M. Tracey and T.S. Cook, "Analysis of Power Type Singularities Using Finite Elements," International Journal of Numerical Methods in Engineering, 11, 1225, 1977.

60. J.R. Rice, "A Path Dependent Integral and the Approximate Analysis of Strain Concentration by Notches and Cracks," Journal of Applied Mechanics, 90, 379, 1968.

61. J. Knowles and E. Sternberg, "On A Class of Conservation Laws in Linearized and Finite Elastostatics," Archives for Rational Mechanics and Analysis, 44, 187, 1972.

62. B. Budiansky and J.R. Rice, "Conservation Laws and Energy Release Rates," Journal of Applied Mechanics, 95, 201, 1973.

63. O. Gurdogan, Ph.D. Dissertation, Department of Engineering Mechanics, The Ohio State University, in progress.

64. S.H. Advani et.al., "Fluid Flow, Structural, and Fracture Mechanics Modeling Associated with Hydraulic Stimulation Operations," Proc. 1982 SPE/DOE Symposium on Unconventional Gas Recovery, Paper No. SPE/DOE 10846, 1982.

65. S.H. Advani et.al., "Fracture Mechanics and Structural Response Investigations Associated with Energy Resource Recovery," Final Report, Grant No. G1115393, The Ohio State University Research Foundation, Dec. 1982.

66. L.M. Keer and S.H. Chen, "The Intersection of a Pressurized Crack with a Joint," Journal of Geophysical Research, 86, 1032, 1982.

TABLE OF CONTENTS

Part B

STRESS TRAJECTORY SIMULATIONS FOR THE EGSP

ABSTRACT

A brief review of pertinent in situ stress studies and rationale for stress trajectory characterizations for the EGSP is presented. Structural cross sections representing the influence of the Rome trough are analyzed and potential mechanisms for in situ stress reorientation and tectonic relief are identified. Detailed stress simulations of cross-sections through Southeastern Kanawha County extending from the Warfield anticline to the Cabin Creek syncline are also reported. In addition, a discussion of results and their correlation with salient structural features is given.

1.0 INTRODUCTION

The phenomenological theories of gas production, from a rock mechanics vantage point, are related to the inherent characteristics of the natural fractures and their subsequent linking with induced fracturing. A detailed knowledge of the prevalent reservoir in situ stress fields and gradients can provide fundamental data regarding preferential orientations, governing mechanisms, and optimum design of stimulation treatments [1,2]. Several stress mediated mechanisms that generate endogeneous and exogeneous fractures have been postulated in the literature [3,4]. A presentation of basic concepts for the analysis of fracture and fault development has been given by Bombolakis [5]. Considerable research has also been conducted on various methods for mapping fractures/joints, surface measurements, directional physical property measurement of oriented cores, mini-hydraulic fracture tests and their correlation with in situ stress magnitudes and orientations [6,7,8,9]. A comprehensive compilation of pertinent work related to the Eastern Gas Shales Project has been recently conducted by Cliffs Minerals [10]. Representative relationships between structure and stress ratio have been developed by Komar and Bolyard (Fig. 1) with a modified form presented in Reference [10] (Fig. 2). Based on a study by Lewin and Associates, Inc., the stress ratio index appears to serve as a valid indicator for fracture spacing [11].

A study on the influence of burial history on subsurface horizontal stress variation formations with different material properties has been reported by Prats [12]. This work demonstrates the effects of creep, temperature, material property and strain alterations on the current stress state. A related investigation, using laboratory determined material

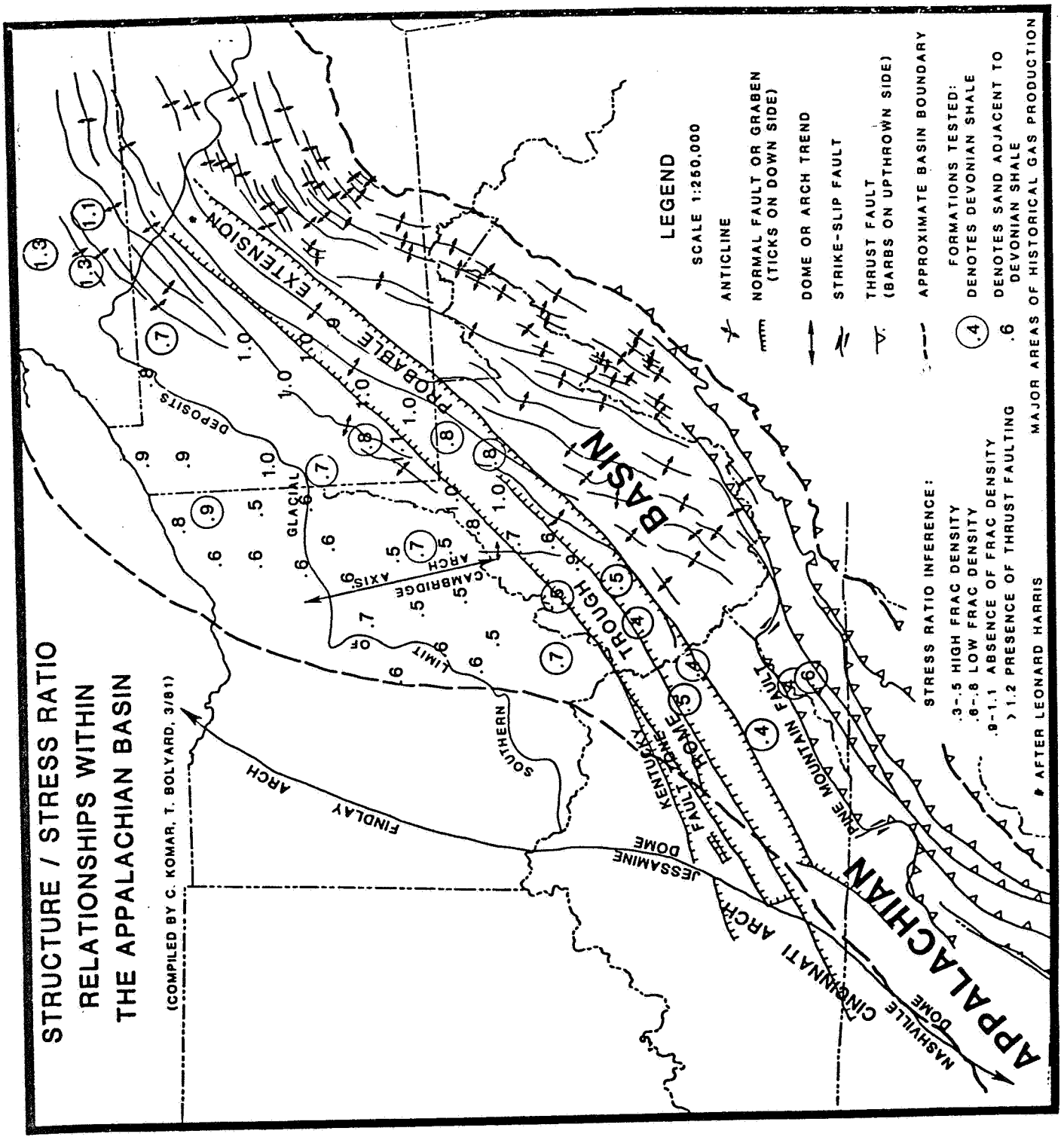

Figure 1. Structure/Stress Ratio Relationships Within the Appalachian Basin.

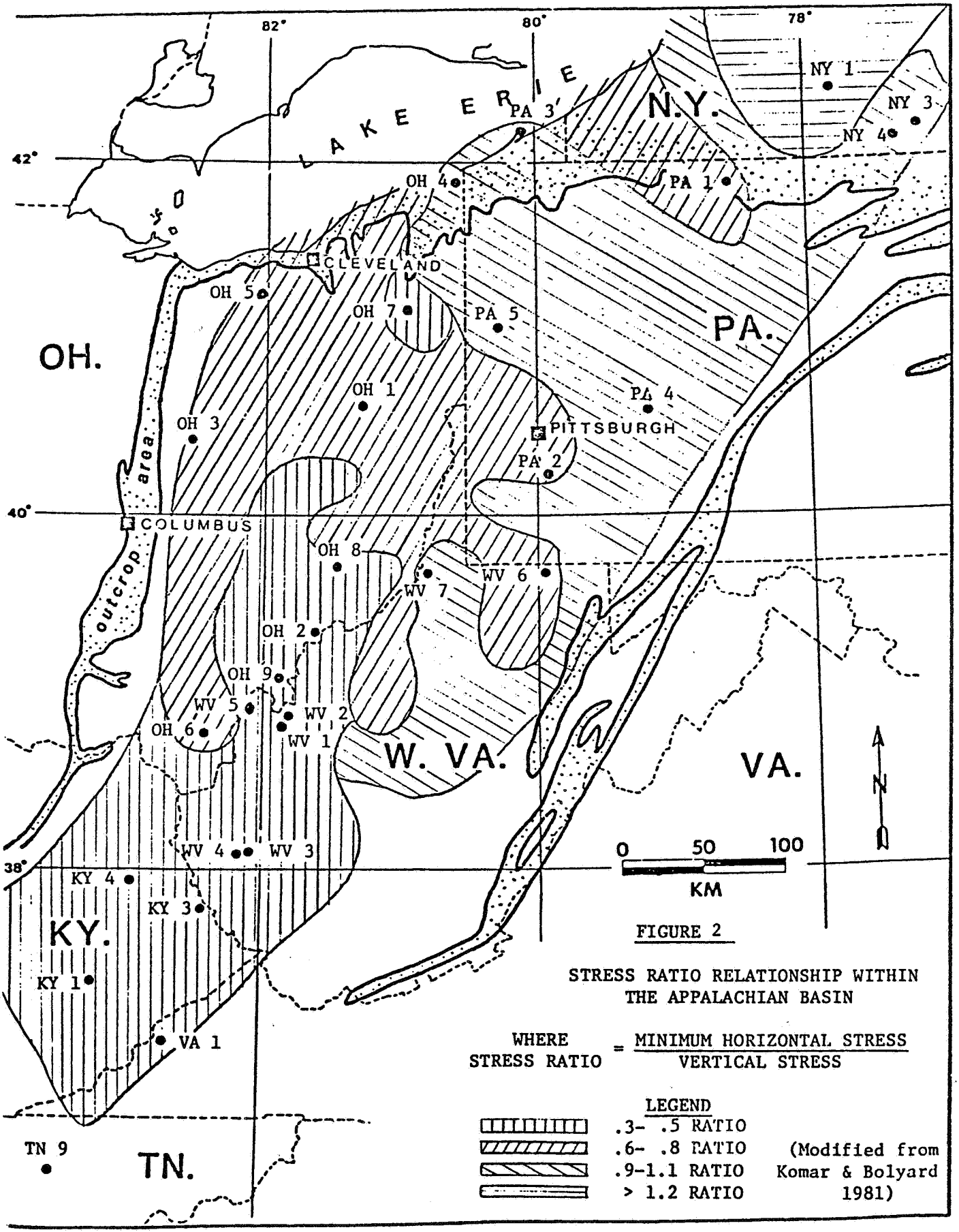

FIGURE 2

STRESS RATIO RELATIONSHIP WITHIN THE APPALACHIAN BASIN

WHERE STRESS RATIO = MINIMUM HORIZONTAL STRESS / VERTICAL STRESS

LEGEND

.3- .5 RATIO	
.6- .8 RATIO	(Modified from Komar & Bolyard 1981)
.9-1.1 RATIO	
> 1.2 RATIO	

properties, correlates field measured horizontal stress data with overburden induced stresses associated with the slope of the confining stress-axial stress curve and vertical temperature gradients [13]. Use of this in situ stress data base for granite, sandstone, limestone shale, and salt as a tool for optimizing fracture containment design has been advanced by Voegele et al. [14]. The stress difference ($\sigma_{OVERBURDEN} - \sigma_{HMIN}$) versus σ_{HMIN} plots can be re-interpreted in terms of stress ratios and are more realistic indicators than Poisson ratio deduced values.

In this report, representative structural cross-sections representing the influence of the Rome trough are analyzed and potential mechanisms for in situ stress orientation and tectonic relief are delineated. Sample stress trajectory simulations of cross-sections through Southeastern Kanawha County extending from the Warfield anticline to the Cabin Creek syncline are reported. Based on these studies, a discussion of the results along with the role of dominant structural mechanisms is presented.

2.0 PRELIMINATRY ROME TROUGH SIMULATIONS

The preliminary stress trajectory simulations for an idealized model of the region overlying the Rome Trough provide a basic understanding of the structural mechanisms governing the in situ stress re-orientations and potential tectonic relief. Fig. 3 illustrates the postulated stress orientations in the Appalachian basin, based on the study by Overbey [15]. The stress trajectories in the region overlying the Rome Trough, a buried rift system (Fig. 4), are of particular interest [16], since they serve as a diagnostic model for several gas producing regions. The maximum horizontal stresses over the Rome Trough parallel the trend of the rift system and appear to be related to the basement faulting. This behavior tends to indicate that the subsurface Rome Trough is influencing the modern state of stress at the surface. If this hypothesis is valid, the state of stress within the Appalachian basin can be analyzed using realistic structural models, i.e. with conditions of basement faulting, boundary conditions, layering, and other geological influences incorporated.

The application of the finite element methodology to the analysis of in situ stresses in reservoir stratigraphic formations is relatively new [17,18]. This approach, however, can be used as an engineering tool for problems with defined boundary conditions, material property data, stratigraphic descriptions, and layer interface conditions.

The geological structure within the Appalachian basin, for this study, is modeled by rigid basement structures containing potentially active faults overlain by passive sedimentary cover with potential slip zones along bedding planes (Fig. 5). The basement faults form the boundaries of the sedimentary cover, as shown in Fig. 5 [19]. The depths of the

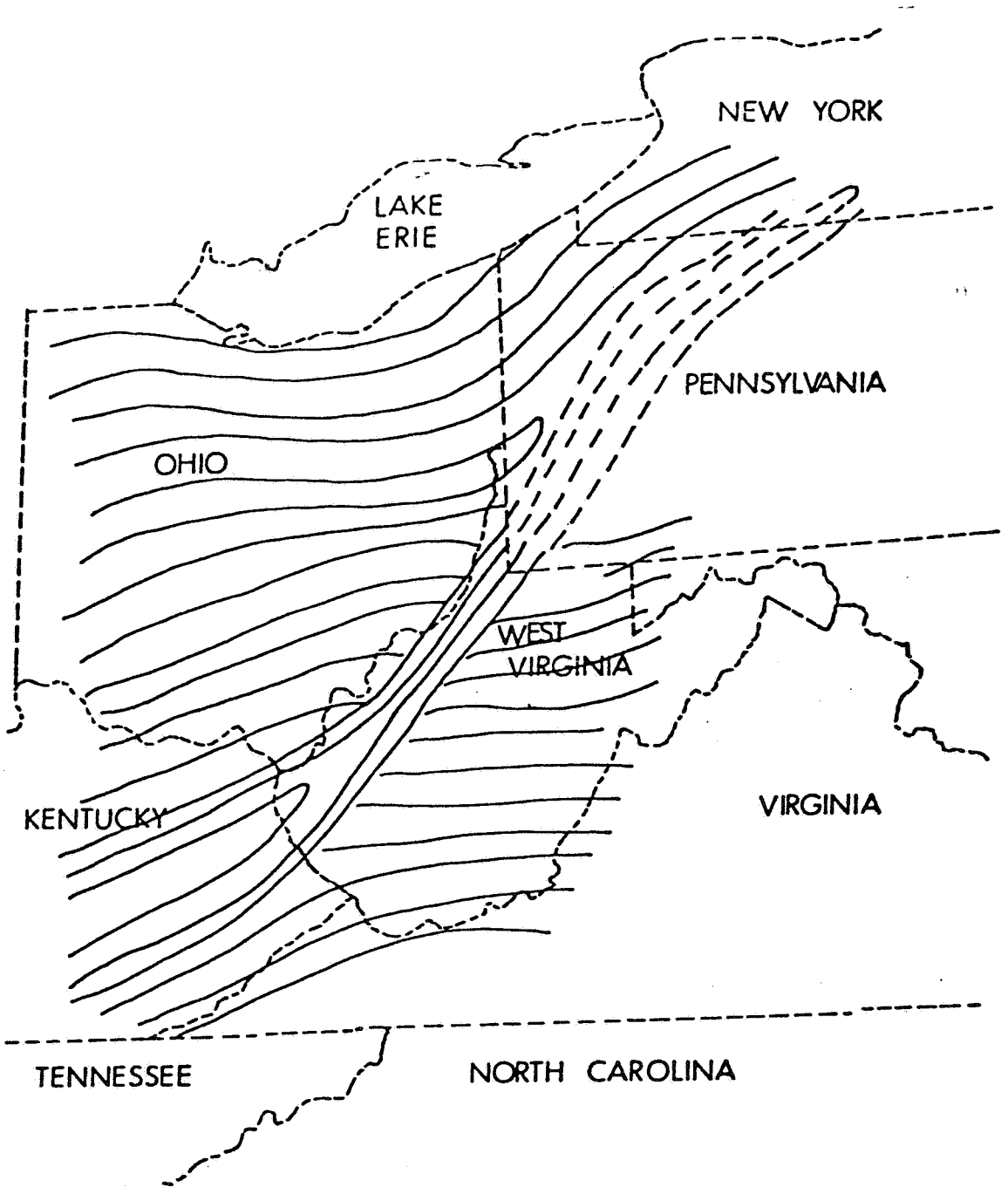

Fig. 3 – Postulated stress trajectories for the Central Appalachian plateau region.

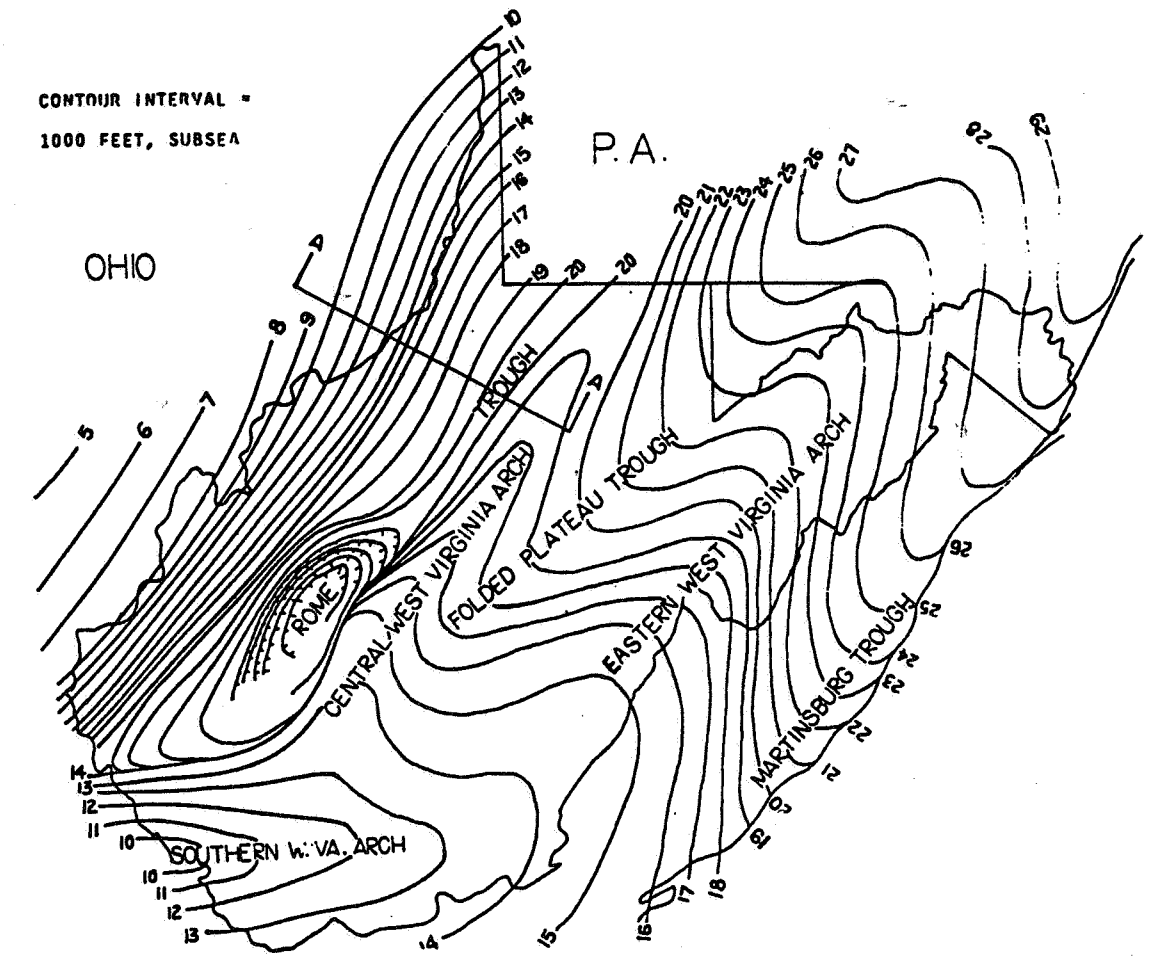

Fig. 4: Basement depth map illustrating Rome trough.

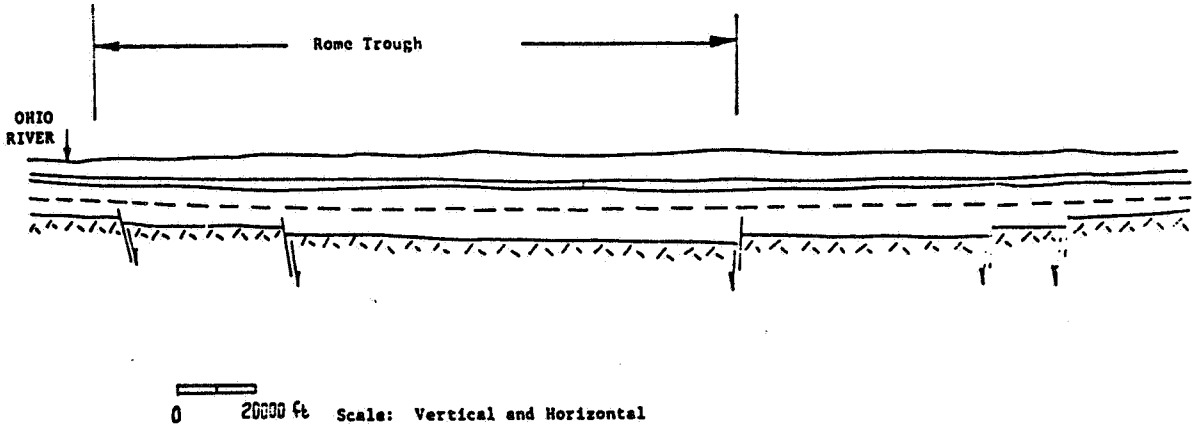

Fig. 5: Schematic of Rome trough tectonics.

sedimentary cover are considerably smaller than the modeled horizontal distances (Section AA in Fig. 4) and a plane strain model idealization is appropriate for the analysis. A layered model with a sequence of composite plate structures (i.e., layers of sandstone, shale, dolomite, limestone, granite, etc.) has been previously studied to demonstrate the effects of buttress and slip loadings [17]. Here, isotropic model characterizations are investigated to provide preliminary trends for separate phenomenological cases characterized by (i) uniform tectonic stress (ii) gravity and associated confining loads and (iii) basement fault slip. These basic cases are illustrated in Figs. 6a, b, c. Selected non-dimensionalized stress trajectories are revealed in Figs. 7a, b, c with resultant stress states shown in Figs. 7d, e. The presence of tensile and/or tectonically relaxed zones is particularly evident in these models and provides a plausible basis for characterizing fracture systems resulting from this basement-cover interaction and resulting stress re-orientation mechanism(s). Detailed studies of pertinent cross-sections are presented in the subsequent section.

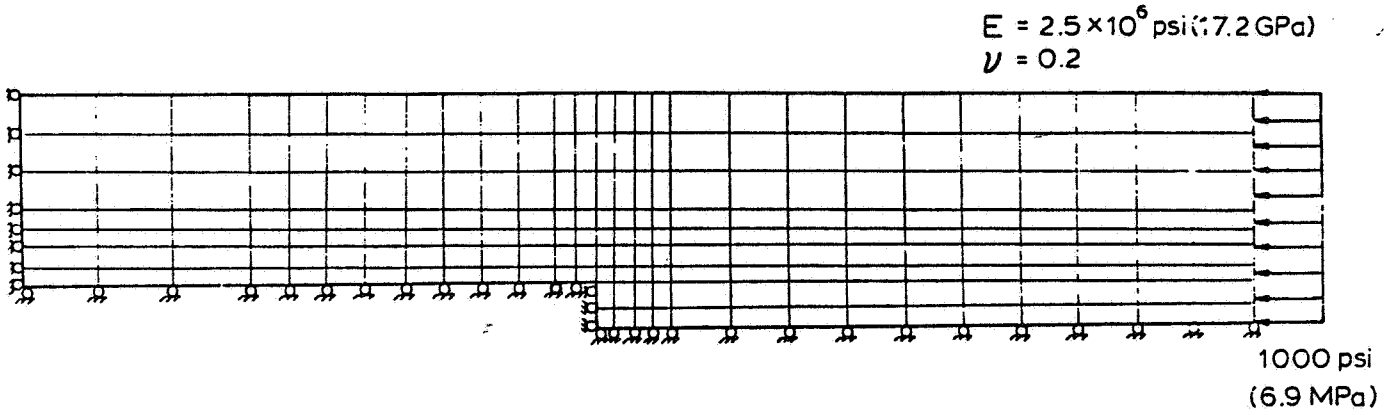

Fig. 6a: Idealized basement-cover model subjected to uniform tectonic stress.

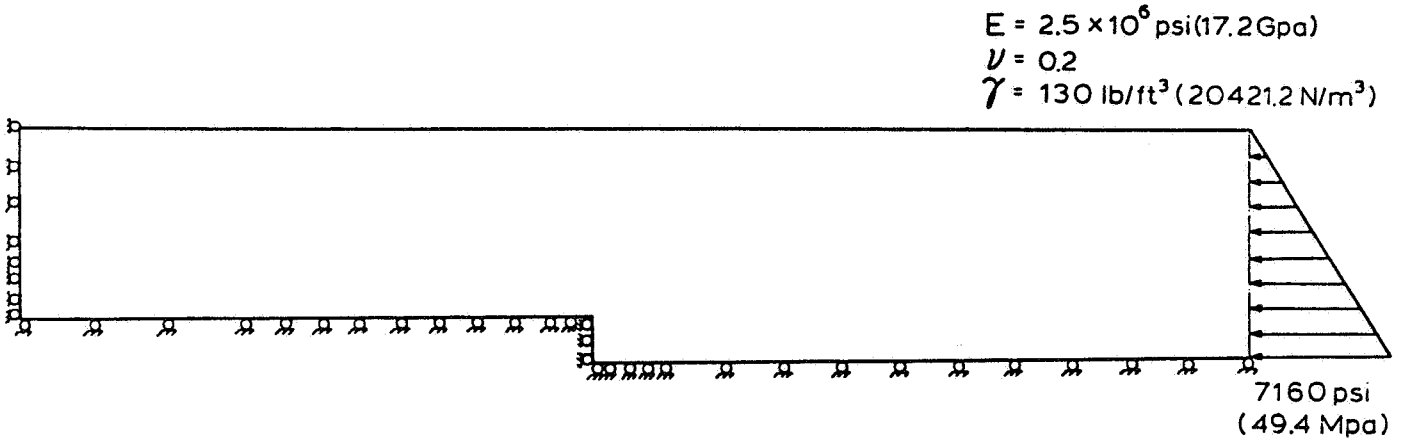

Fig. 6b: Idealized basement-cover model subjected to gravitational loading.

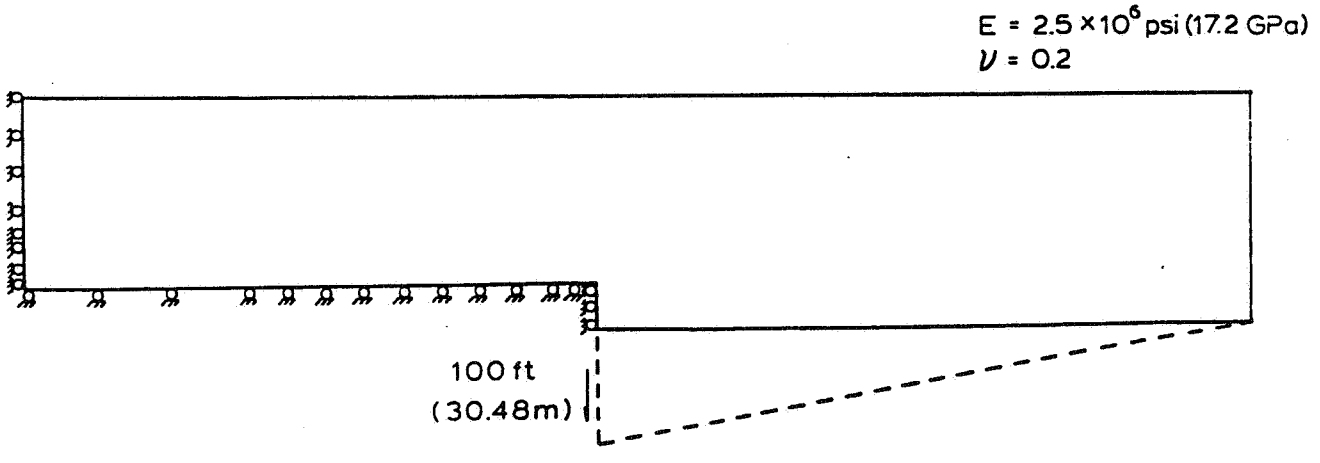

Fig. 6c: Idealized basement-cover model subjected to slip loading.

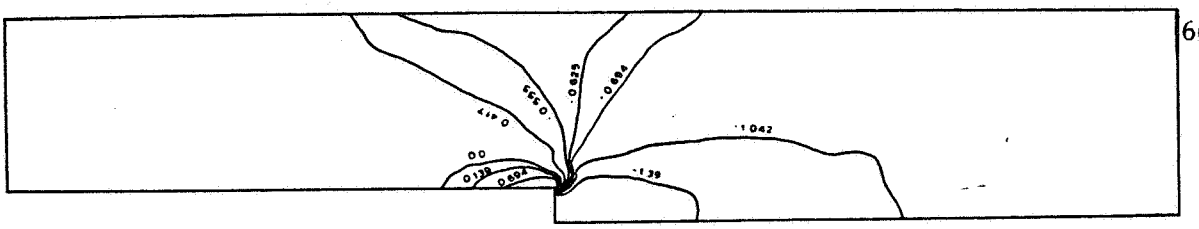

Fig. 7a: Horizontal normal stress magnitudes for model in Fig. 4a for unit tectonic stress.

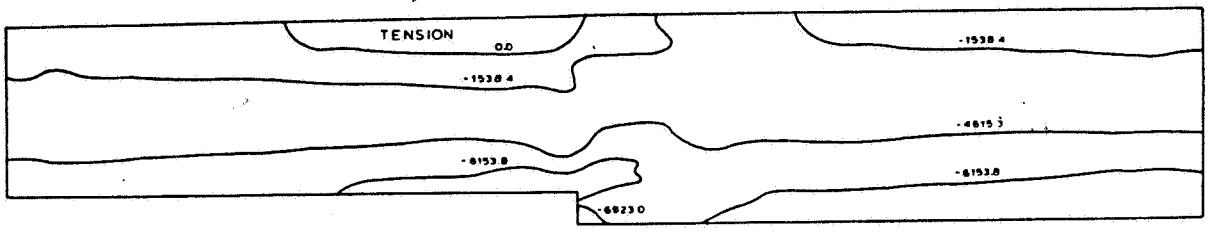

Fig. 7b: Horizontal normal stress magnitudes for model in Fig. 4b normalized with respect to ρg (lb/ft^2 units).

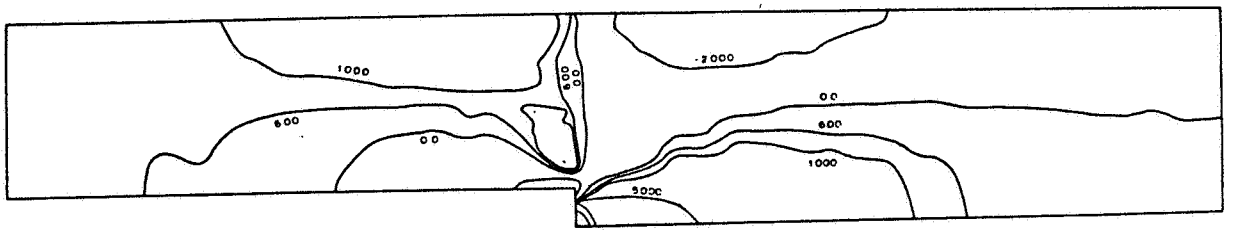

Fig. 7c: Horizontal normal stress magnitudes for model in Fig. 4c for unit slip (lb/ft^2 units).

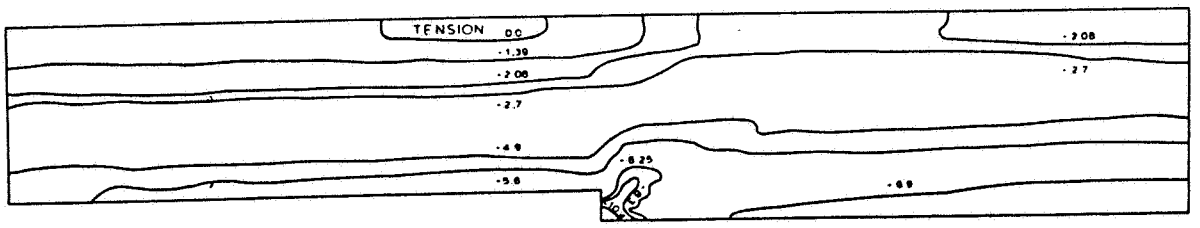

Fig. 7d: Resultant horizontal normal stress magnitudes for superposed tectonic and gravitational loading (1000 psi units).

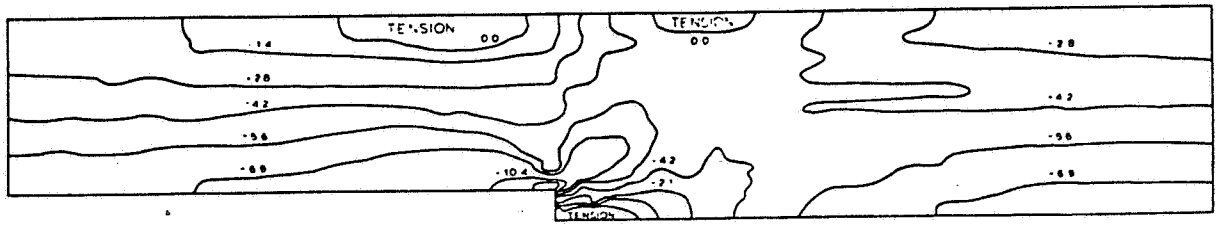

Fig. 7e: Resultant horizontal normal stress magnitudes for superposed tectonic, gravitational, and slip loading (1000 psi units).

3.0 KANAWHA COUNTY CROSS-SECTION SIMULATIONS

The simulations in the previous section, although not directed at a specific locale, demonstrated the general applicability of the finite element method in examining the Rome Trough's marginal abutments on overlying formation stress behavior. This methodology, with prudently defined geologic structural properties, can also serve as a diagnostic tool for the exploration of naturally fractured gas reservoirs in the Devonian Shales of the Appalachian basin. In this section, detailed stress analyses for cross-sections through the southern part of Kanawha County overlying the eastern margin of the Rome Trough is presented. Supplementary observations and results are also reported in Appendix D.

The region selected for this study is the Cabin Creek district of Kanawha County, West Virginia (Fig. 8). This is the largest district of Kanawha County and occupies an area of 235 square miles. It is located south and southeast of Louden, Malden, and Elk districts. Good gas production has been found above the Devonian in the Big Lime and Weir Sand. The exposed rocks throughout Kanawha County are nearly horizontal. The rocks lie in broad gentle folds, modified only by a gentle monoclinical trend which brings older rocks to the surface from the northwest to the southeast. The gentle structures present a strike ranging between N30^{o}E to N45^{o}E. Near the surface, Cabin Creek has two distinguishing structural features; namely, the Warfield anticline to the northwest and the Wake Forest anticline to the Southeast. These anticlines were selected as bounds for the cross-sectional analysis.

Evidence to date suggests that the deepest section of the Rome Trough lies in the Kanawha County. The eastern flank of the Rome Trough through

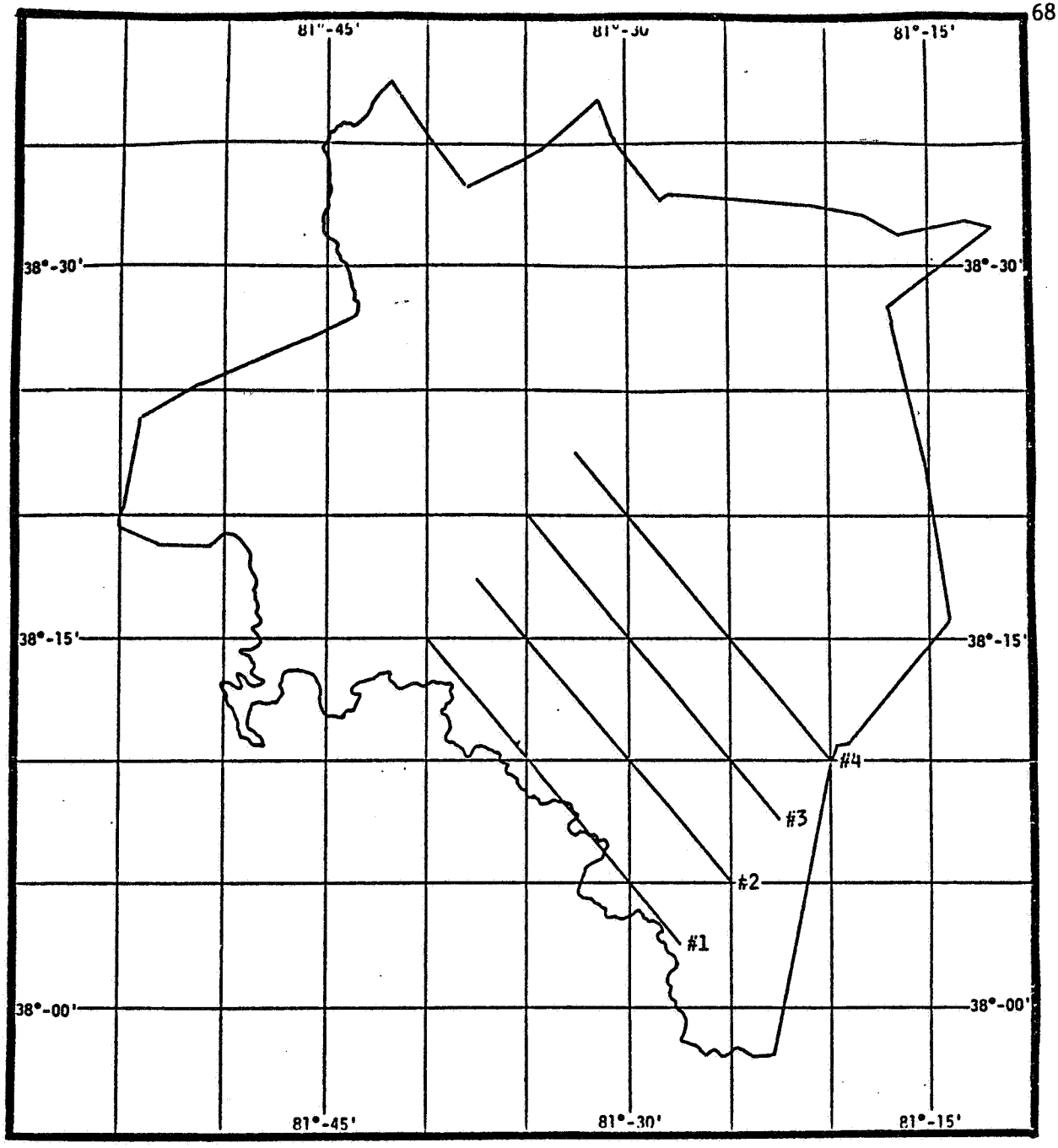

#1 N38-02-30, W81-27-30 TO N38-15-00, W81-40-00
#2 N38-05-00, W81-25-00 TO N38-17-30, W81-37-30
#3 N38-07-30, W81-22-30 TO N38-20-00, W81-35-00
#4 N38-10-00, W81-20-00 TO N38-22-30, W81-32-30

MAP OF
KANAWHA COUNTY
WEST VIRGINIA

CROSS SECTIONS

Figure 8. Map of Kanawha County, W.Va. with Cross-Sections.

scale 1/26400

5 4 3 2 1 0 5 10 miles

this county is steepened by pronounced faulting (Appendix D-Plate 2). Normal faults, down to the West, produce a maximum vertical separation of 7000 ft within a horizontal distance of several miles. Total relief along the eastern margin of the trough in the county is approximately 10,000 ft from the trough axis to the crest of the eastward lying central West Virginia arch. The western trough is also undoubtedly faulted and a zone of increased low amplitude folds in Paleozic strata lies between the trough and arch axis.

The basement faults, including related structural style changes and geophysical anomalies, separate two major fracture domains. Regionally consistent systematic and non-systematic fractures in coal (face and butt cleats) are well developed and alter trend immediately above the basement faults delineating the eastern margin of the Rome Trough. Coal systematic fractures over the Rome Trough trend N45^{o}W. The predominant fracture orientation within the domain southeast of the basement fault zone trends is N70^{o}E (Appendix D-Plate 1). The boundary separating the two major fracture domains is marked and abrupt. Fracture trends common to one domain change within two to ten miles to fracture trends characteristic of the adjoining domain. The fracture domain boundary coincides exactly with the zone of predominant basement faulting and related geophysical anomalies that accentuate the eastern Rome Trough margin. No well-formed fracture sets differing from the regional trends are persistent everywhere along and within the domain boundary.

Kulander [20] assumes that if all systematic fractures formed at approximately the same time, then the basement fault zone would have served as the boundary separating different stress fields responsible for fracturing. The fault zone may have, therefore, contributed to the two distinct

stress fields. If domain boundaries for systematic fractures in other rocks lie over the basement fault zone, photolineaments related to fracture trends and resulting topography could change orientations in this location.

The four cross-sections defined in Fig. 8 were constructed for this study. Figures 9a, b, c, d, illustrating the major lithologic units, indicate that the cross-sections are relatively similar. Hence, the computed stress trajectories, for the same loading and boundary conditions are nearly identical for all cross-sections. Detailed results for cross-section No. 4 are, therefore, presented here. Figure 10a reveals the corresponding finite element discretization using 8-noded isoparametric elements and the node numbering scheme is shown in Fig. 10b. The selected material properties for the basic units are presented below in Table I with detailed property data presented in Appendix D.

TABLE I: Selected Material Properties

Material	Young's Modulus lb/ft^2	Poisson's Ratio ν	Mass Density lbm/ft^3
Sandstone	1.345×10^9	0.112	165.0
Shale	0.658×10^9	0.210	165.0
Limestone/Dolomite	1.555×10^9	0.215	172.8

The considered loadings include (i) gravity, (ii) gravity and specified slip along the fault, (iii) gravity with specified slip along fault and tectonic loading and (iv) gravity with specified tectonic loading. For the case of only gravitational loading, the boundary conditions are zero displacement at the basement and roller supports on the vertical boundaries. Figure 11 illustrates the principal stress magnitudes for this loading with the bold lines indicating tension in some upper shale and sandstone elements.

Figure 9a. Geometry and Structure of Cross-Section #1.

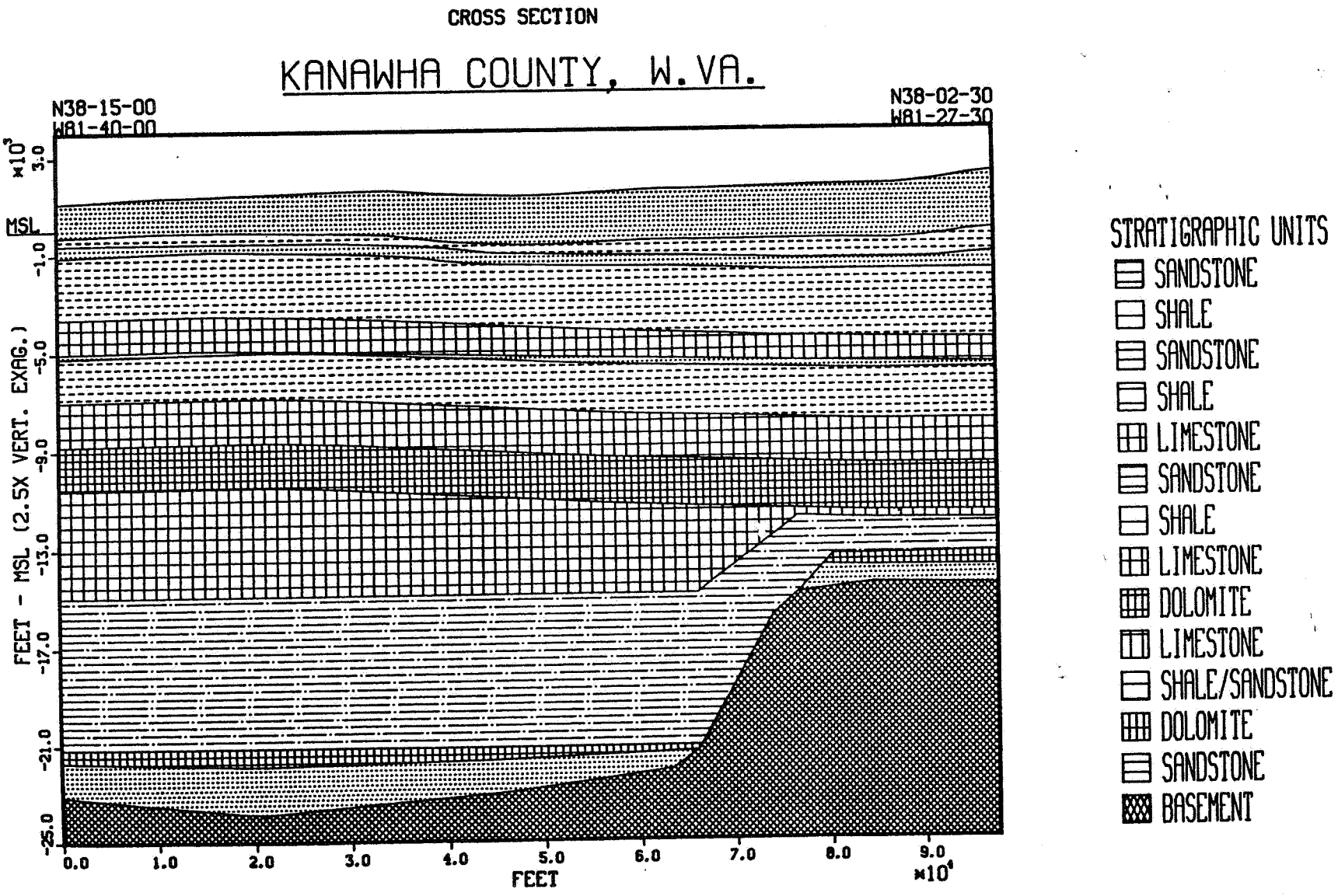

Figure 9b. Geometry and Structure of Cross-Section #2.

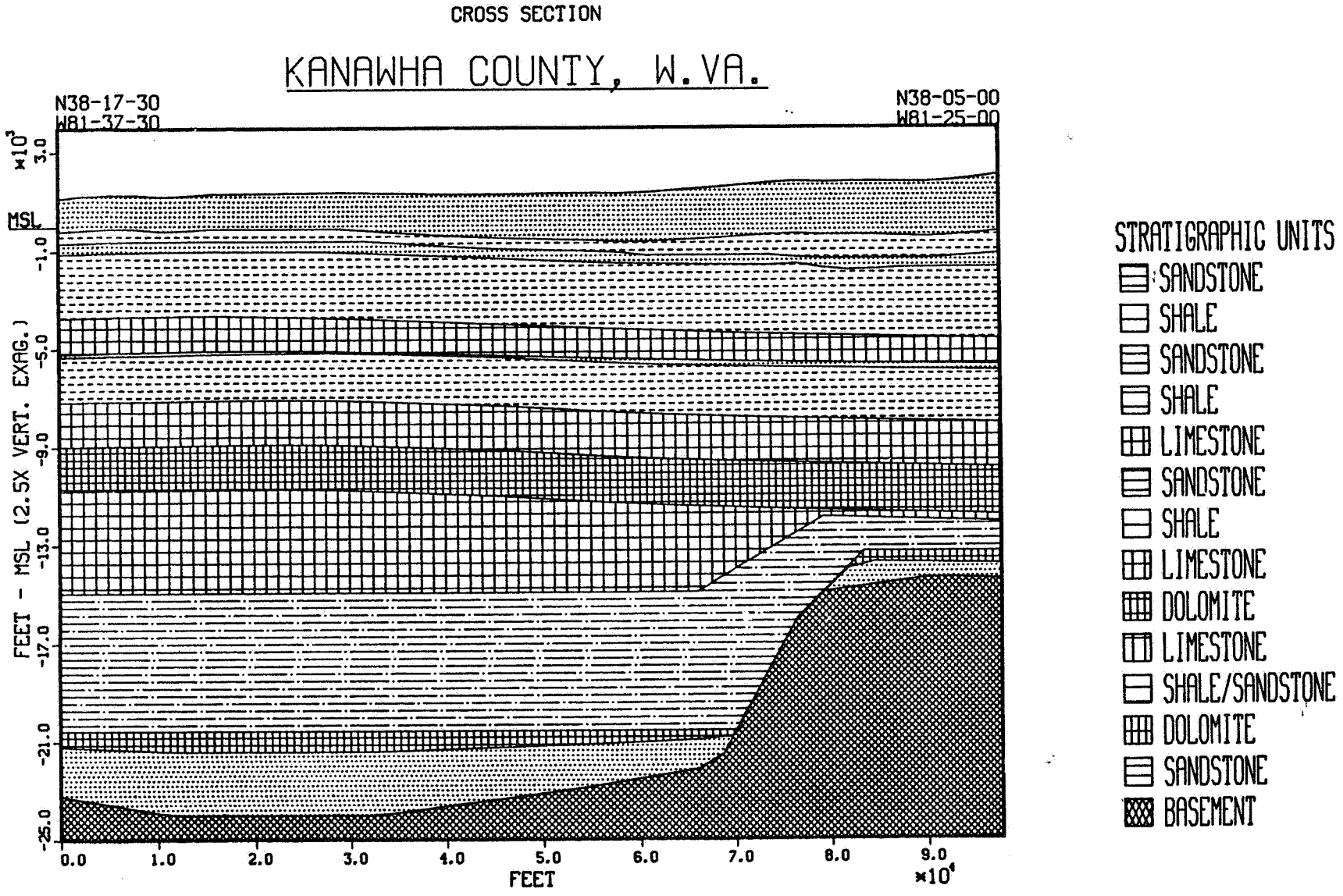

Figure 9c. Geometry and Structure of Cross-Section #3.

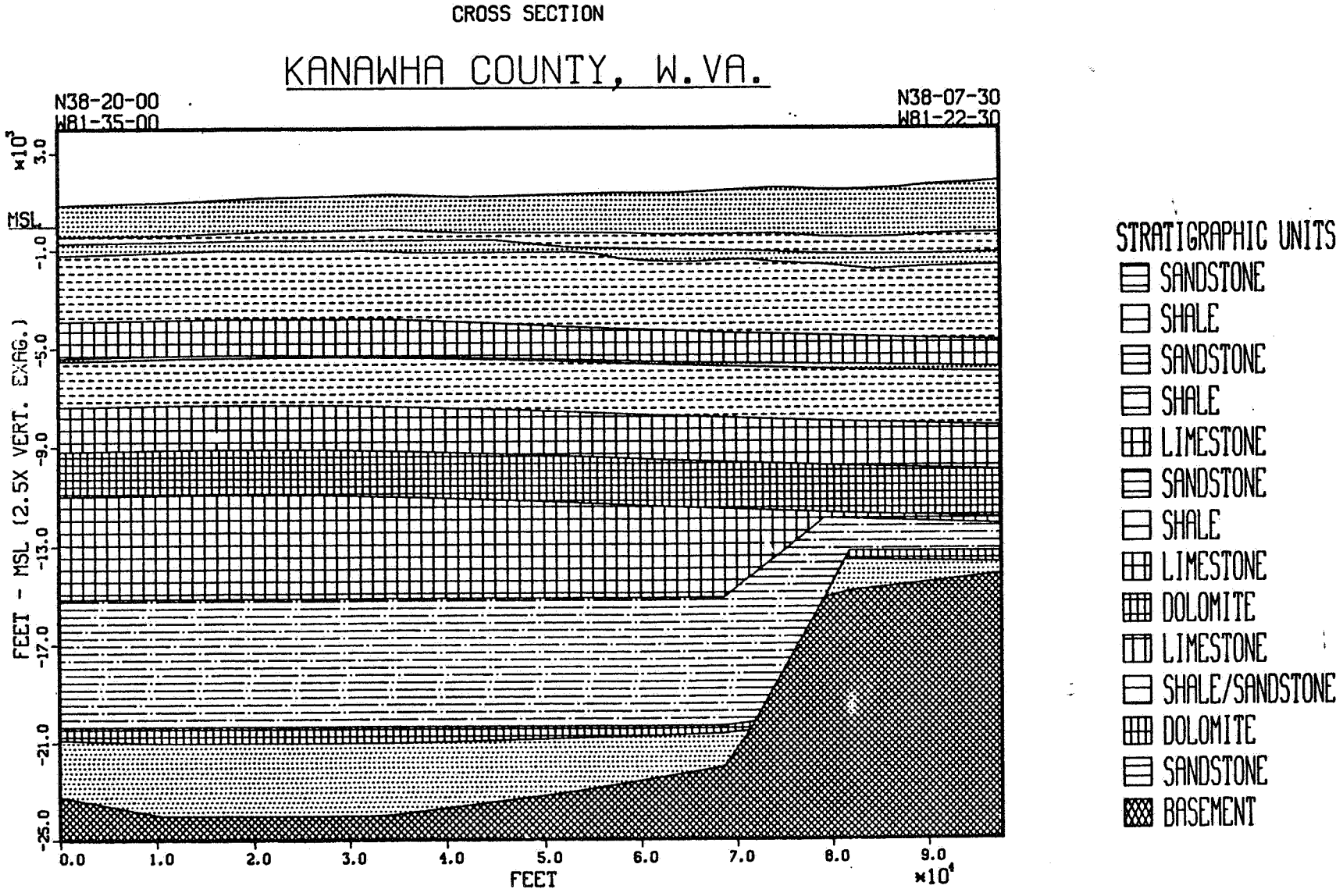

Figure 9d. Geometry and Structure of Cross-Section #4.

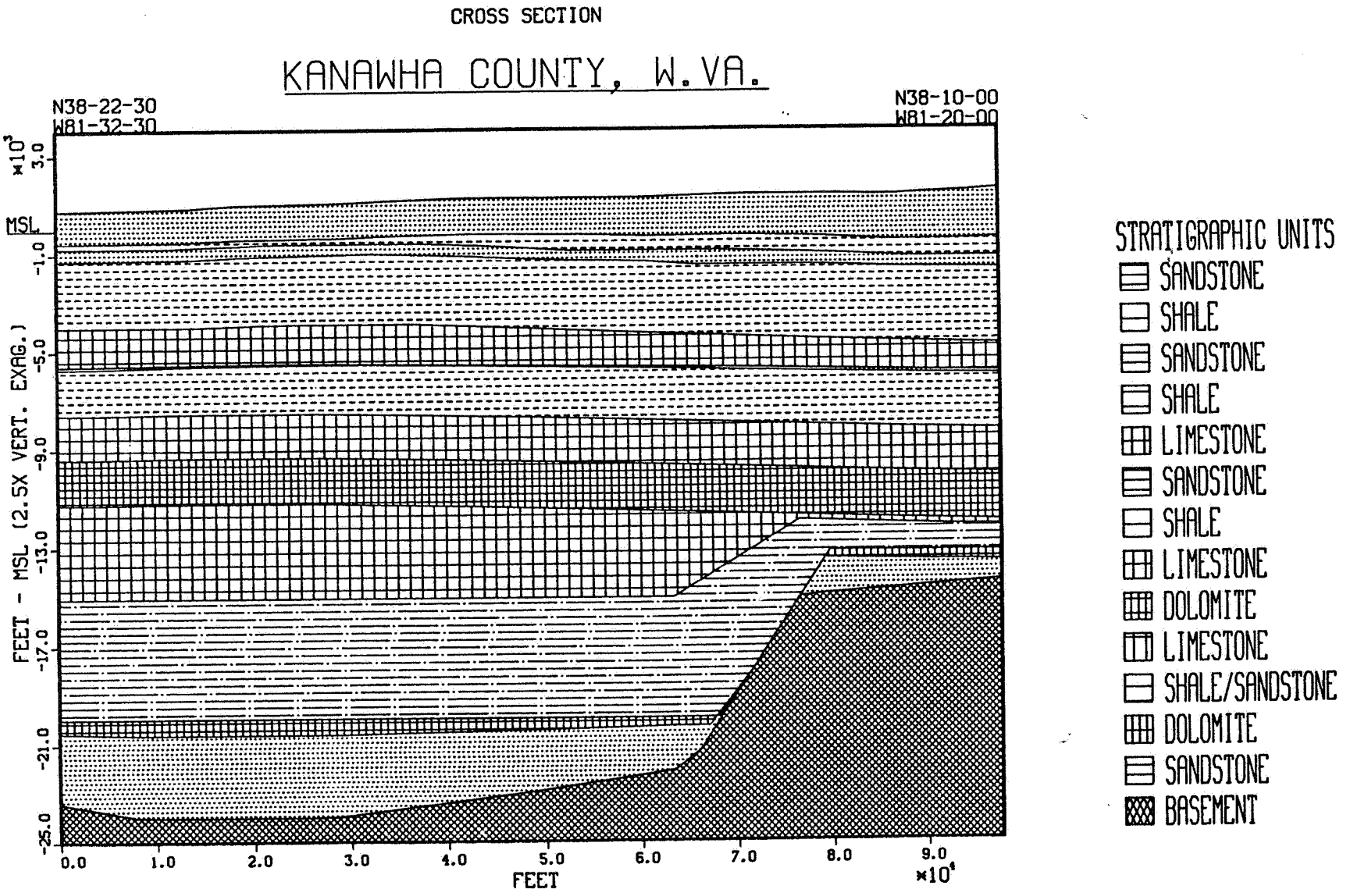

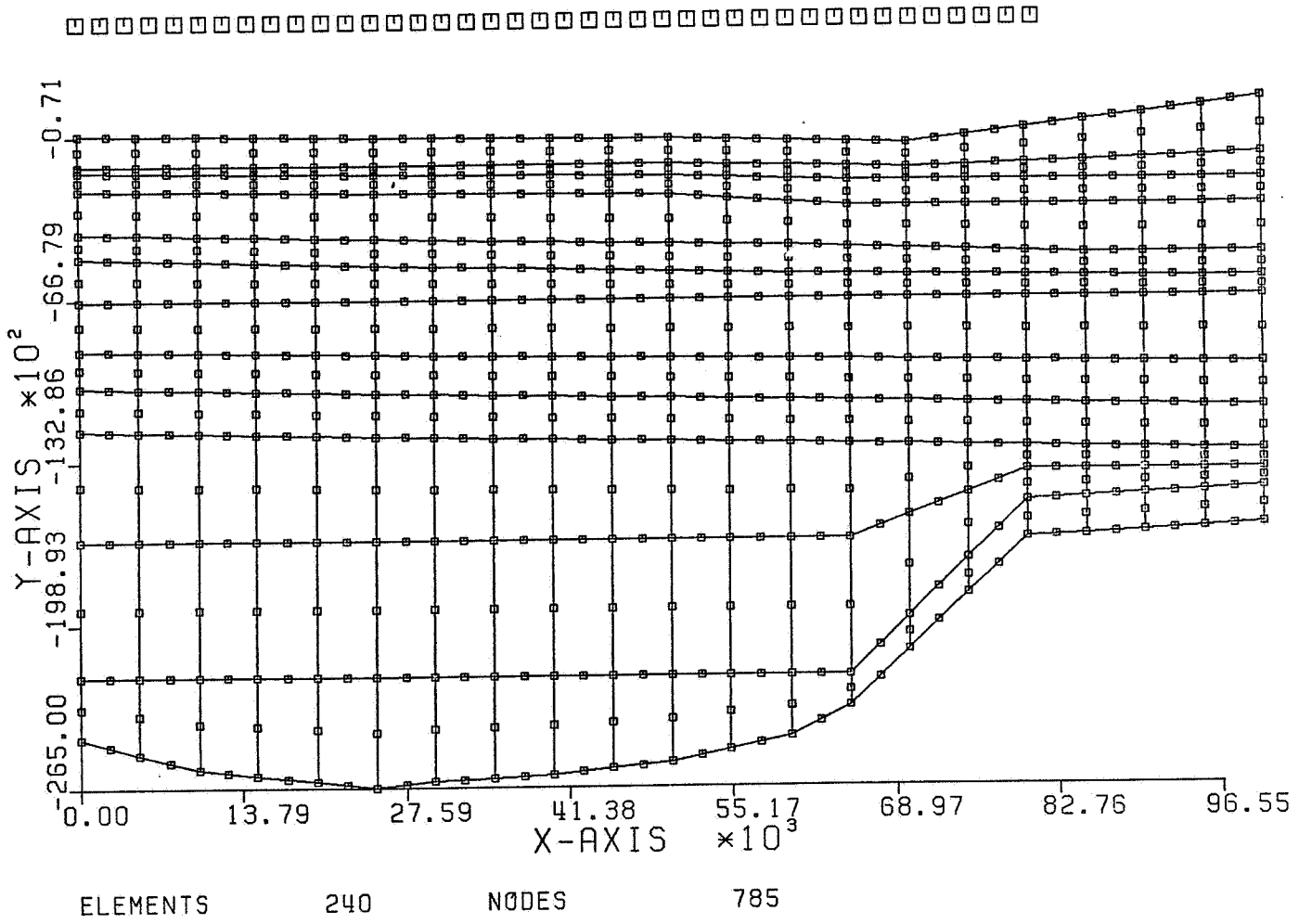

Figure 10a. Finite Element Discretization Using 8-Noded Isoparametric Element of Cross-Section #4.

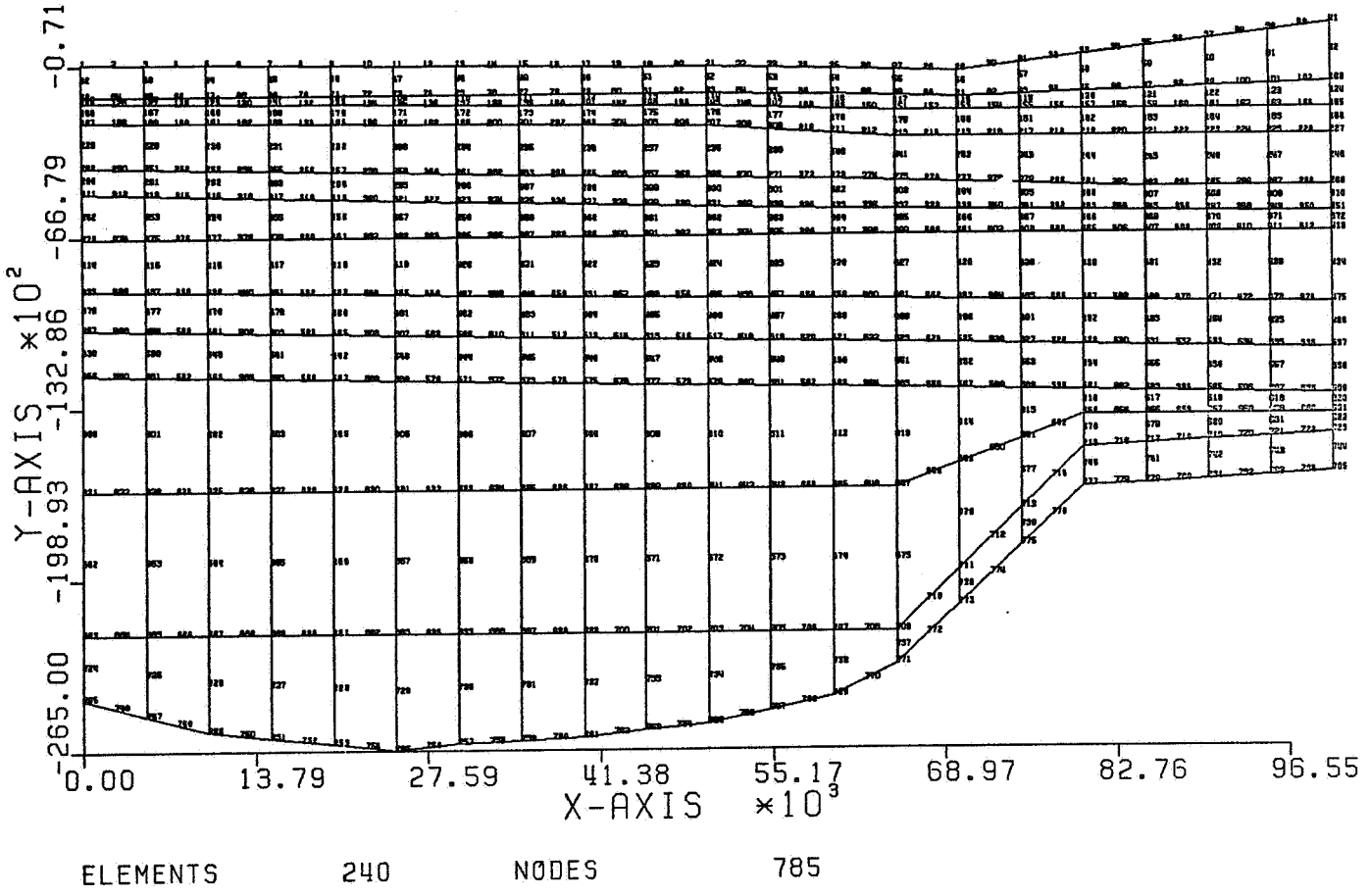

Figure 10b. Nodal Numbering of Finite Element System of Cross-Section #4.

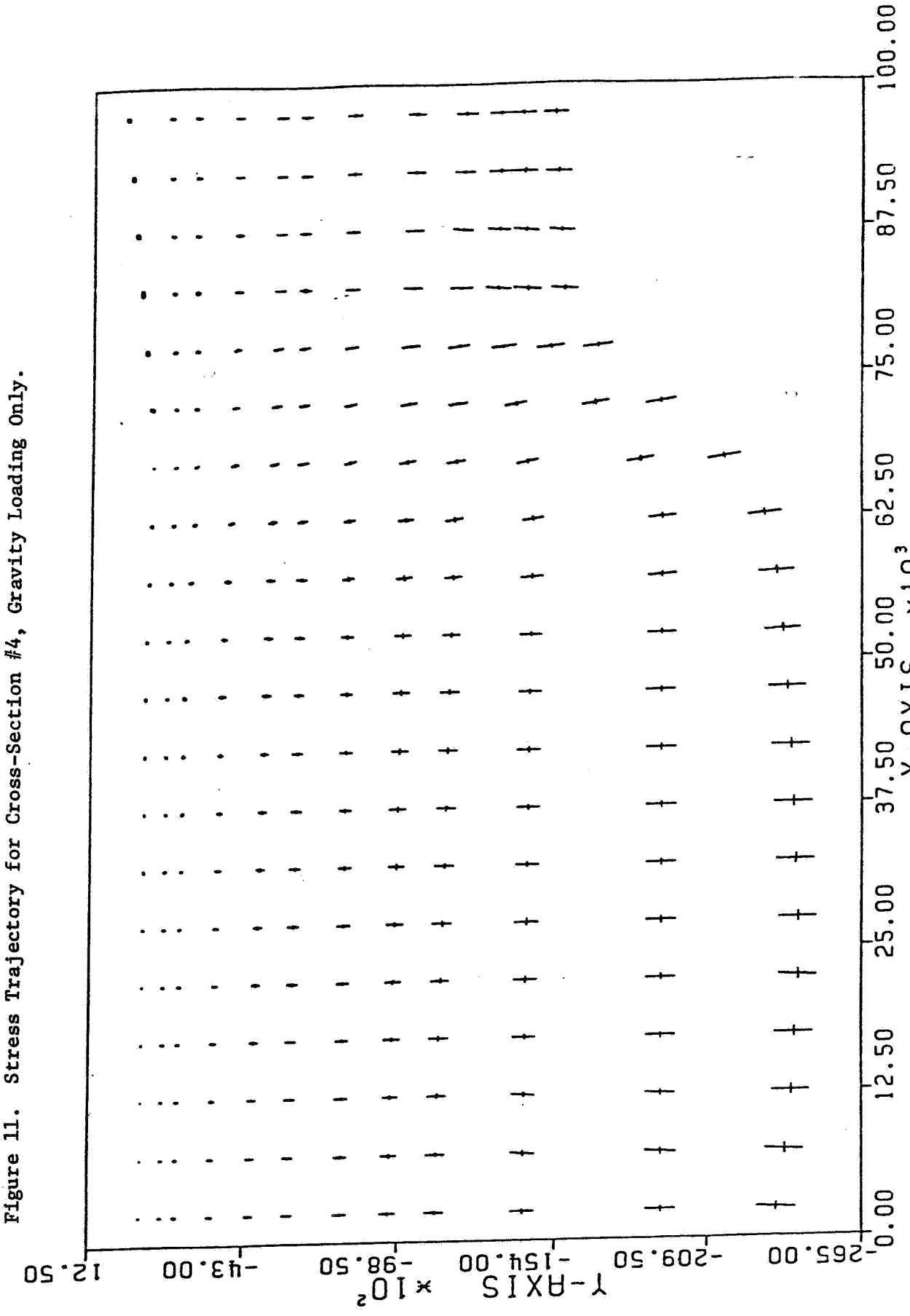

Figure 11. Stress Trajectory for Cross-Section #4, Gravity Loading Only.

The results for the case with a slip of 50 ft at the fault (node 816), in addition to the preceding loading and boundary conditions, are shown in Fig. 12. This slip, with nodes 815 and 817 free, introduces major tensile zones in the vicinity of the fault with some elements near the surface changing from compression to tension. The results for the case with the preceding gravity and slip loading with a tectonic stress of 1000 psi superimposed are shown in Fig. 13. As expected, the tectonic relief is annuled by this applied compressive stress. Finally, Fig. 14 reveals the case of specified horizontal stress on the southeast boundary of the cross-section with gravitational loading prevalent. The computed horizontal stresses, for zero normal displacements, on the northwest section are also shown in Fig. 14. Corresponding cross-sectional principal stress magnitudes are shown in Fig. 15.

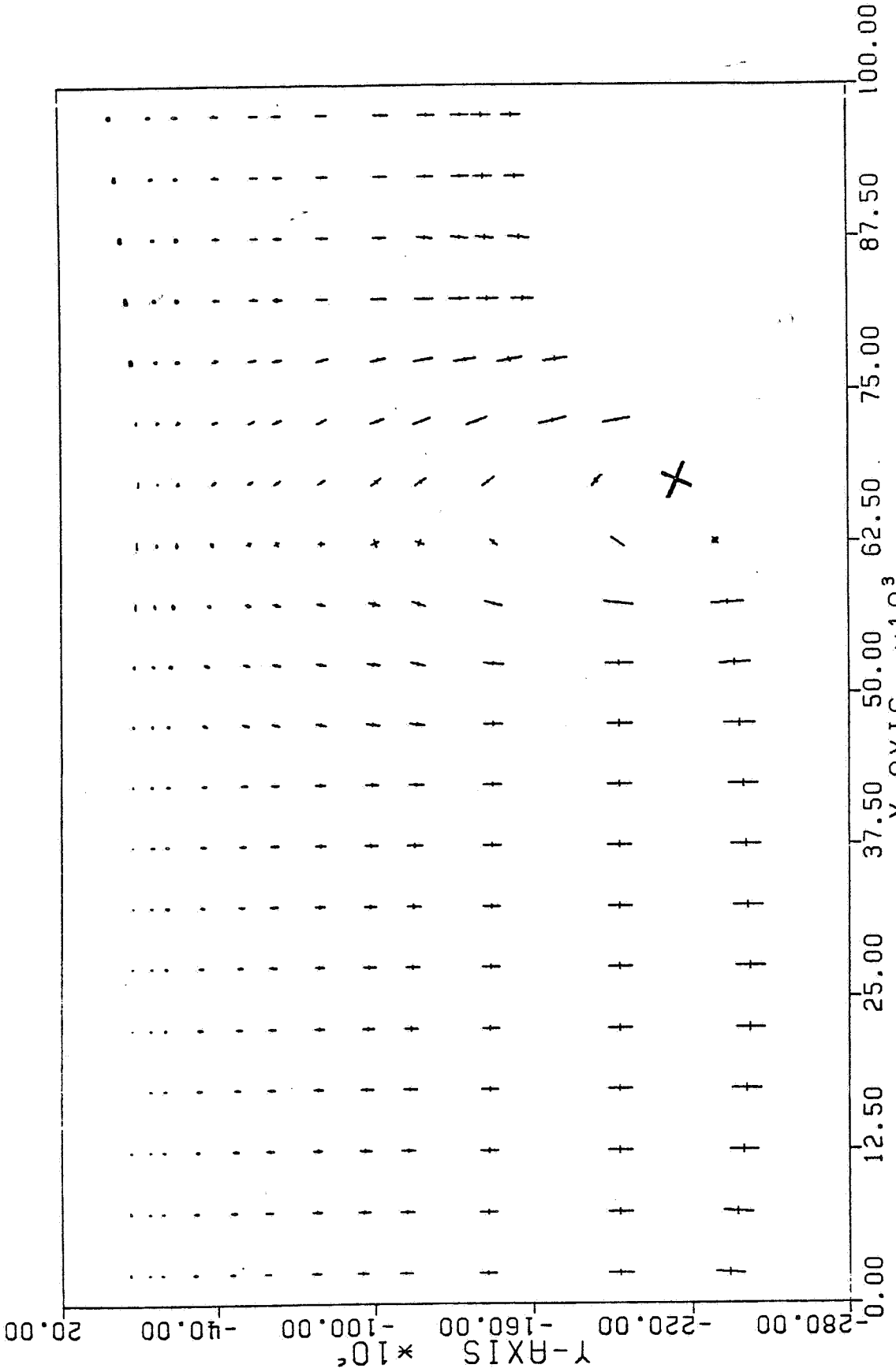

Figure 12. Stress Trajectory for Cross-Section #4, Gravity and 50 ft Slip.

Figure 13. Stress Trajectory for Cross-Section #4, Gravity with 50ft Slip and Tectonic Loading

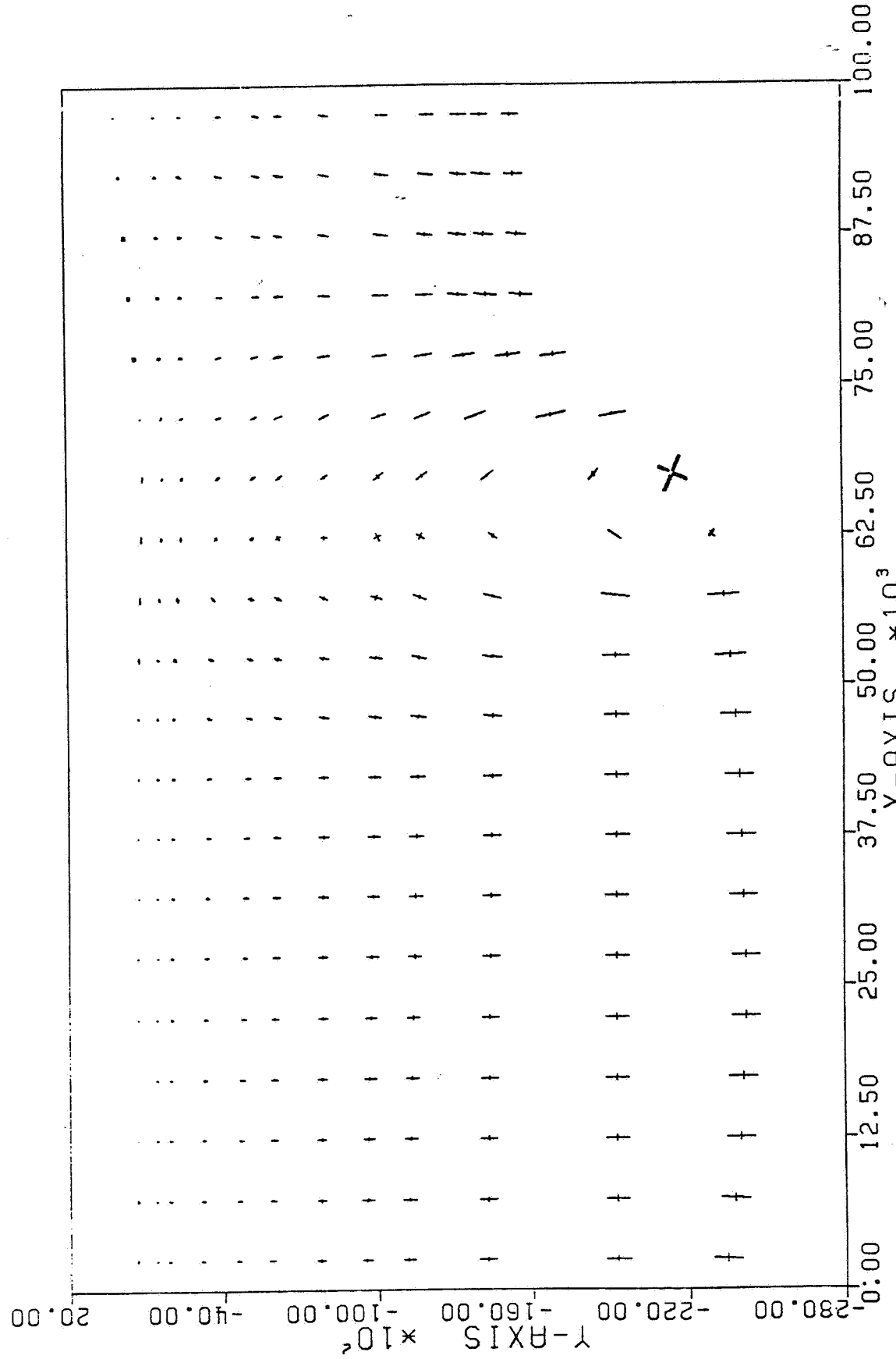

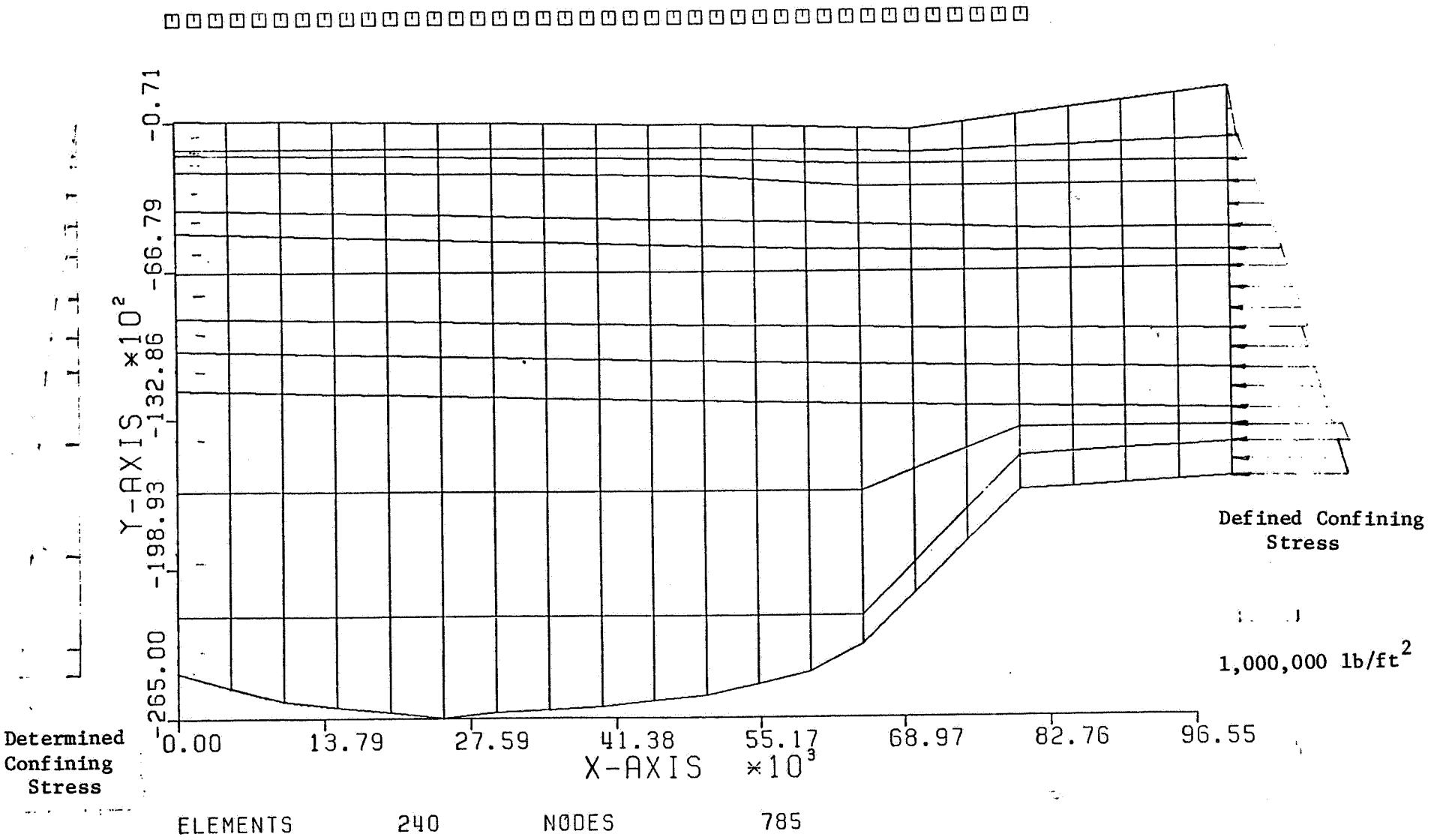

Figure 14. Determined Horizontal Stress on Northwest Section for Specified Stress on Southeast Boundary - Cross-Section #4

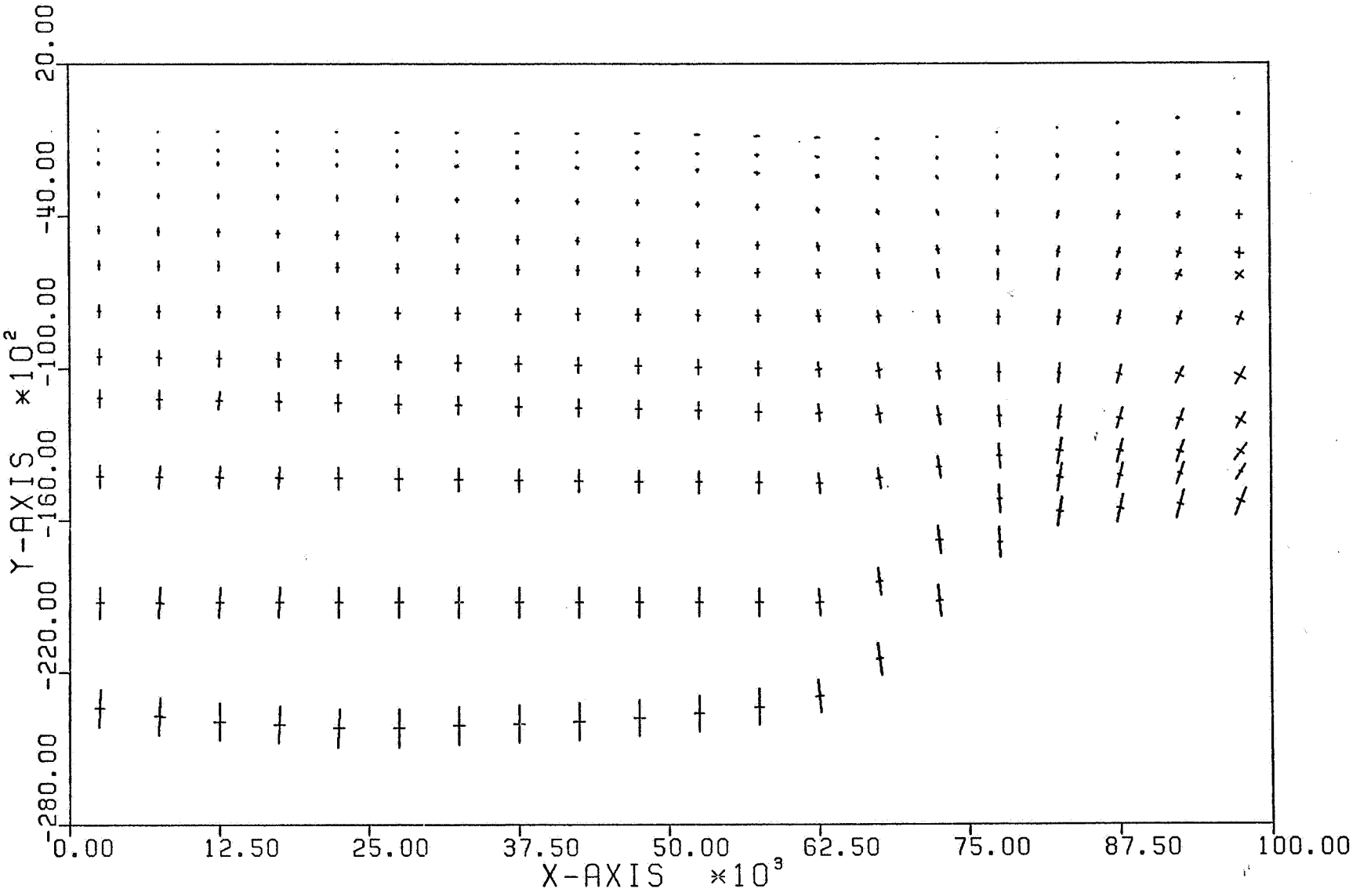

THE STRESS MAGNITUDE OF SECTION TWO --- GRAVITY+RIGHT TECTONIC

+ 4076000.1b/sq ft - PLOT SCALE; THIN LINE-COMP. STR. THICK LINE-TENS

Figure 15. Stress Plots for Cross-Section #4 for Loading in Figure 14.

4.0 DISCUSSION AND CONCLUSIONS

The preceding preliminary Rome Trough and Kanawha County cross-sectional simulations illustrate the facilitating characteristics of the finite element method in predicting governing stress mediated mechanisms and in situ stress trajectories for idealized and layered geological formations. The applicability of this technique for even gross in situ stress predictions and correlations with major domains such as North America [21] can not, however, be demonstrated with the current state-of-the-art in view of the complexities associated with the evolution, stress history, and boundary conditions. Cross-sectional analysis of a large section traversing two major fault zones from Southeast Ashtabula County, Ohio to Central Clearfield County, Pennsylvania (185 miles) was also conducted with various layers overlying the basement. Qualitative stress trends parallel to those obtained in Section 3.0 were similarly obtained.

Towse [22] has discussed the evolution and stress history of the low-permeability upper cretaceous gas reservoirs in the Rocky Mountains by considering the rock properties and associated structures. The development of various faults (normal, overthrust, strike-slip) and reservoir fracture pattern correlations, from the vantage point of the in situ stress fields, is also presented. Similar analysis, in conjunction with finite element evaluations, will be very fruitful in defining joint fracture orientations and extent.

Figure 16 presents the computed stress ratios in the Devonian shales for cross-section #4 with loading defined on the southeast boundary. The stress ratio magnitudes show a considerable variation across the cross-section because of the buttress basement-layered cover interaction. It

should be noted that the stress ratios are relative and are normalized with respect to the applied boundary loading. The presence of defined major fracture systems in the shales and adjacent layers will substantially alter the state of stress. Computations using the singular fracture elements presented in Section 2.3 are recommended for future research.

Finally, the use of the presented techniques as a tool in the selection of mineback field sites [23] and related stimulation treatment design and evaluation can not be overemphasized.

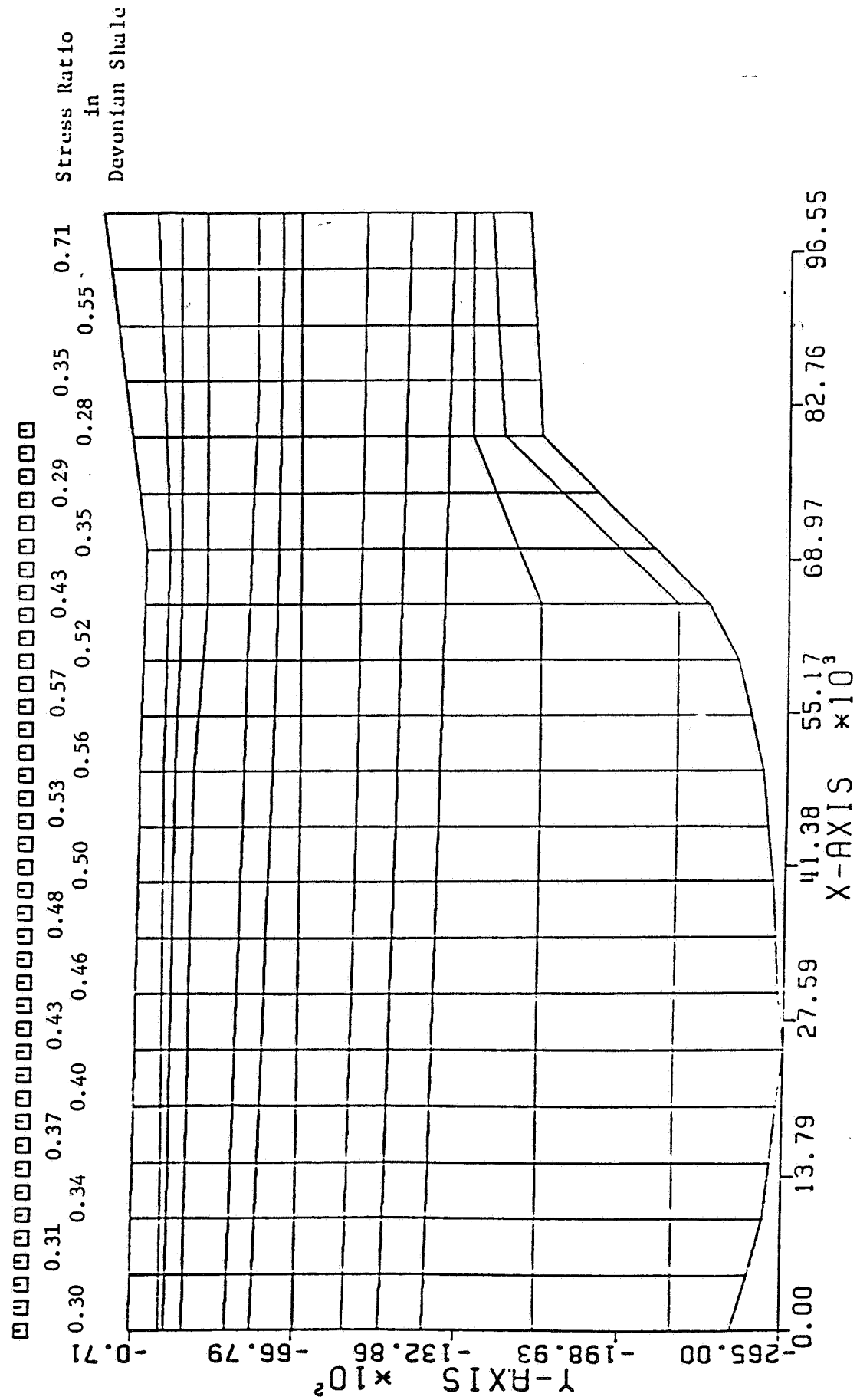

Figure 16. Predicted Stress Ratios in Devonian Shale for Cross-Section #4 for Loading in Figure 14.

5.0 REFERENCES

1. C.A. Komar, "Development of a Rationale for Stimulation Design in the Shale," Society of Petroleum Engineers of AIME, Paper No. SPE 7166, 1978.

2. S.H. Advani et al., "The Role of Rock Mechanics in Optimizing Devonian Gas Production from the Appalachian Basin," Society of Petroleum Engineers of AIME, Paper No. SPE 10370, 1982.

3. W.K. Overbey, Jr., "Effect of In Situ Stress on Induced Fractures," Proceedings of the 7th Annual Appalachian Petroleum Geology Symposium, MERC/SP-72/2, 1976.

4. P.C. Badgley, "Structural and Tectonic Principles," Harper and Row, New York, 1965.

5. E.G. Bombolakis, "Some Constraints and Aids for Analysis of Fracture and Fault Development," Proceedings 2nd International Conference on New Basement Tectonics, 1976.

6. W.K. Overbey, Jr. and R.L. Rough, "Surface Studies Predict Orientation of Induced Formation Fractures," Producers Monthly, 32, 6, 1968.

7. C.E. Brechtel et al., "In Situ Stress Determination in the Devonian Shales (Ira McCoy 20402) Within the Rome Trough Basin," Terra Tek Report TR-77-36, 1977.

8. C. Fairhurst, "Methods of Determining In Situ Rock Stresses at Great Depths," School of Mineral and Metallurgical Engineering Report, University of Minnesota, December 1967.

9. T.L. Blanton et al., "Mechanical Properties of Devonian Shales from the Appalachian Basin," Science Applications, Inc. Final Report, Contract No. DE-AM21-78MC08216, 1981.

10. Anon, "Analysis of the Devonian Shales in the Appalachian Basin," Vol. I, Cliff Minerals Inc. Final Report, Contract No. DE-AC21-80MC-14693, September 1982.

11. Anon, "Analysis of Devonian Shale Gas Production Mechanisms in Application to Devonian Gas Shales of Ohio," Lewin and Associates, Inc. and Consultants Final Report, Contract No. DE-AC21-82MC-19239, January 1983.

12. M. Prats, "Effect of Burial History on the Subsurface Horizontal Stresses of Formations Having Different Material Properties," Society of Petroleum Engineers Journal, 658, December 1981.

13. A.S. Abou-Sayed, "Laboratory Evaluation of In-Situ Stress Contrast in Deeply Buried Sediments," Society of Petroleum Engineers of AIME, Paper No. SPE 11069, 1982.

14. M.D. Voegele et al., "Optimization of Stimulation Design Through the Use of In-Situ Stress Determination," Journal of Petroleum Technology, 1071, June 1983.

15. H.Y. Chang et al., "Feasibility Study on Modeling of Stress Trajectories Across the Appalachian Plateau Province in West Virginia," Final Report, West Virginia University, Contract No. EY-77-X-21-0368, 1978.

16. B.R. Kulander and S.L. Dean, "Gravity, Magnetics, and Structures, Allegheny Plateau/Western Valley and Ridge in West Virginia and Adjacent Slates," West Virginia Geological and Economic Survey, RI-27, 1978.

17. S.H. Advani et al., "Stress Trajectory Simulations Across the Appalachian Plateau Province in West Virginia," Proceedings First Annual Shale Symposium, pp. 320-327, 1977.

18. N.R. Warpinski et al., "Laboratory Investigation on the Effect of In-Situ Stresses on Hydraulic Fracture Containment," 1981 SPE/DOE Low Permeability Symposium, SPE/DOE Paper 9834, 1981.

19. R.C. Shumaker, Private Communication, Department of Geology and Geography, West Virginia University, 1977, 1982.

20. B. Kulander, Private Communication, Department of Geology, Wright State University, 1981, 1982, 1983.

21. E.N. Lindner and J.A. Halpern, "In Situ Stress in North America: A Compilation," International Journal of Rock Mechanics, Mining Sciences and Geomechanics Abstracts, 15, 183, 1978.

22. D. Towse, "The Evolution and Stress History of the Low-Permeability Upper Cretaceous Gas Reservoirs in the Rocky Mountains," Lawrence Livermore Laboratory UCRL Preprint 83514, 1980.

23. Anon, "Determination of Mineback Field Site Availability," The BDM Corporation, Quarterly Report, Contract No. 5082-213-0744, June 1983.

TABLE OF CONTENTS

APPENDIX A

FINITE ELEMENT MODEL SIMULATIONS ASSOCIATED WITH HYDRAULIC FRACTURING

S.H. Advani and J.K. Lee

Department of Engineering Mechanics
The Ohio State University

Finite Element Model Simulations Associated With Hydraulic Fracturing

Sunder H. Advani, Ohio State U.
J.K. Lee, Ohio State U.

Abstract

Recently emphasis has been placed on the development and testing of innovative well stimulation techniques for the recovery of unconventional gas resources. The design of optimal hydraulic fracturing treatments for specified reservoir conditions requires sophisticated models for predicting the induced fracture geometry and interpreting governing mechanisms.

This paper presents methodology and results pertinent to hydraulic fracture modeling for the U.S. DOE's Eastern Gas Shales Program (EGSP). The presented finite-element model simulations extend available modeling efforts and provide a unified framework for evaluation of fracture dimensions and associated responses. Examples illustrating the role of multilayering, in-situ stress, joint interaction, and branched cracks are given. Selected comparisons and applications also are discussed.

Introduction

Selection and design of stimulation treatments for Devonian shale wells has received considerable attention in recent years.[1-3] The production of natural gas from such tight eastern petroliferous basins is dependent on the vertical thickness of the organically rich shale matrix, its inherent fracture system density, anisotropy, and extent, and the communication-link characteristics of the induced fracture system(s). The investigation of stimulation techniques based on resource characterization, reservoir property evaluation, theoretical and laboratory model simulations, and field testing is a logical step toward the development of commercial technology for optimizing gas production and related costs.

This paper reports formulations, methodology, and results associated with analytical simulations of hydraulic fracturing for EGSP. The presented model extends work reported by Perkins and Kern,[4] Nordgren,[5] Geertsma and DeKlerk,[6] and Geertsma and Haafkens.[7] The simulations provide a finite-element model framework for studying vertically induced fracture responses with the effects of multilayering and in-situ stress considered. In this context, Brechtel *et al.*,[8] Daneshy,[9] Cleary,[10] and Anderson *et al.*[11] have done recent studies addressing specific aspects of this problem. The use of finite-element model techniques for studying mixed-mode fracture problems encountered in dendritic fracturing and vertical fracture/joint interaction also is illustrated along with application of suitable failure criteria.

Vertical Hydraulic Fracture Model Formulations

Coupled structural fracture mechanics and fracture fluid response models for predicting hydraulically induced fracture responses have been reported previously.[12,13] These simulations incorporate specified reservoir properties, in-situ stress conditions, and stimulation treatment parameters. One shortcoming of this modeling effort is that finite-element techniques are used for the structural and stress intensity simulations, while a finite-difference approach is used to evaluate the leakoff and fracture-fluid response in the vertical crack. A consistent framework for conducting all simulations using finite-element modeling is formulated here.

The steady-state and transient fracture-width response, governed by the fracture fluid variables, multilayering, and minimum effective horizontal in-situ stress, is determined initially by combining the formulations and solutions presented by Geertsma and Haafkens[7] and Advani *et al.*[12] The plane-strain vertical-crack model is illustrated in Fig. 1, with fluid coupling provided by the crack interface pressure. The one-dimensional width equation, as applied by Nordgren[5] on the basis of the Perkins and Kern model,[4] for a porous-permeable isotropic elastic medium is

0197-7520/82/0004-8941$00.25

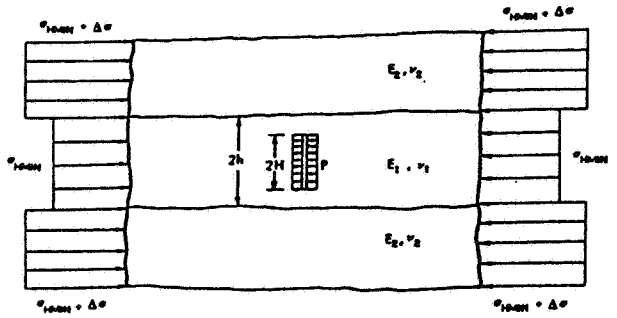

Fig. 1—Plane-strain idealization of vertical-crack model.

$$\frac{E}{128(1-\nu^2)\,(2H)\mu}\,\frac{\partial^2 W^4}{\partial x^2}-\frac{\partial W}{\partial t}=\frac{8C}{\pi\sqrt{t-\tau(x)}}, \quad \ldots\ldots\ldots\ldots\ldots\ldots\ldots\ldots (1)$$

along with the initial condition $W(x,0)=0$ and the boundary conditions

$$W(x,t)=0, \text{ for } x>L(t)$$

and

$$-\left(\frac{\partial W^4}{\partial x}\right)_{x=0}=\frac{256\mu(1-\nu^2)Q}{\pi E}$$

for a two-sided fracture.

The steady-state solution and finite-difference results for the transient problem have been presented by Nordgren[5] and Geertsma and Haafkens.[7] The discretized finite-element weak form of the extended version of Eq. 1, obtained by the conventional Galerkin approach,[14] is

$$K_{ij}(a)a^j(t)+C_{ij}\dot{a}^j(t)+F_i(t)=0, \quad \ldots\ldots\ldots\ldots (2)$$

where

$$K_{ij}(a)=\frac{E}{32(1-\nu^2)\,(2H)\mu}\int N^T_{i,x}(N_k a^k)^3 N_{j,x}\,dx,$$

$$C_{ij}=\int N^T_i N_j\,dx,$$

and

$$F_i(t)=\frac{8C}{\pi}\int\frac{N_i}{\sqrt{t-\tau(x)}}\,dx-\frac{QN_i}{\pi H}\bigg|_{x=0},$$

where N_i is the selected interpolation function associated with the ith node defined by

$$W(x,t)=N_i(x)a^i(t)$$

and commas designate differentiation.

For the steady-state problem, the appropriate equation is

$$K_{ij}(a)a^j+F_i(t)=0, \quad \ldots\ldots\ldots\ldots\ldots\ldots\ldots (3)$$

with

$$K_{ij}=\frac{E}{128(1-\nu^2)\,(2H)\mu}$$

$$\cdot\int N^T_{i,x}N_{j,x}\,dx-\frac{QN_i}{\pi H}\bigg|_{x=0}$$

and

$$F_i=\frac{8C}{\pi}\int\frac{N_i}{\sqrt{t-\tau(x)}}\,dx,$$

where N_i is defined by

$$W^4(x,t)=N_i(x)a^i(t).$$

Eq. 3 is the familiar linear stiffness/force matrix formulation. On the other hand, the nonlinearity inherent in the stiffness matrix for Eq. 2 requires the solution of a nonlinear set of algebraic equations. The isotropic medium steady-state and transient width profiles are modified for the multilayered geometry by introducing the width scaling coefficient.[12] Subsequent cumulative leakoff computations are based on the width response. The fracture height and length evaluations require determination of the vertical crack stress intensity factor and application of the percentage leakoff volume.[12] The appropriate volume-balance equation for a two-sided fracture with an elliptical cross-section is

$$\frac{\pi}{4}(2H)\left[\frac{d}{dt}\int_o^L W(x,t)dx\right]+4HC\int_o^t\frac{dL}{d\tau}\,\frac{d\tau}{\sqrt{t-\tau}}=\frac{Q}{2}. \quad \ldots\ldots\ldots\ldots\ldots\ldots\ldots\ldots (4)$$

Eqs. 1 and 4, coupling the transient width and length, provide an iterative framework for computing $W(x,t)$ and $L(t)$. Finite-element computations for several cases and comparisons with the Perkins and Kern[4] and Geertsma and DeKlerk[6] model results are given by Lee.[15]

Eq. 2 can be reduced to an approximate set of nonlinear algebraic equations by dividing the time range into intervals (t_n, t_{n+1}). For each time interval, the time rate of change of the width extended vector may be approximated by the finite ratio $\dot{a}^*=(a_{n+1}-a_n)/\Delta t$ at a particular time t^* where $\dot{a}^*\approx\dot{a}(t^*)$, $a_n\approx a(t_n)$, $a_{n+1}\approx a(t_{n+1})$, and $\Delta t=t_{n+1}-t_n$. Eq. 2 then becomes

$$Y(a_{n+1})\approx H(a_{n+1})a_{n+1}+f(t_{n+1}), \quad \ldots\ldots\ldots\ldots (5)$$

where

$$H(a_{n+1})=K_{ij}(a_{n+1})+C_{ij}/\Delta t$$

and

$$f(t_{n+1})=F_i(t_{n+1})-C_{ij}a_n/\Delta t.$$

The Newton-Raphson method can be used to solve the nonlinear Eq. 5, following formulation of a curtailed Taylor series expansion, at each time step of the computation. Procedures and results for the simultaneous computation of Eq. 1 and the integral Eq. 4 are given.[15]

Vertical Hydraulic Fracture Model Simulations

For the steady-state case, the width and corresponding pressure profiles for specified parameters are compared with the Perkins and Kern solution[4] in Figs. 2a and 2b, respectively. The transient width profile for equal elapsed propagation time intervals is illustrated in Fig. 2c. The parameters, selected from Geertsma and Haafkens[7] for model calibration, are: flow rate $Q=10$ bbl/min (1.6 m^3/min), injected volume $V=200$ bbl (318 m^3), fracture height $2H=100$ ft (30.48 m), fluid loss coefficient $C=0.0015$ ft/min$^{1/2}$ (0.000 46 m/min$^{1/2}$), Poisson's ratio $\nu=0.20$, shear modulus $G=E/2(1+\nu)=2.6\times10^6$ psi (17.94 GPa), and viscosity $\mu=36$ cp (36 Pa·s).

Maximum width comparisons using the one-dimensional finite element formulations and the Perkins and Kern[4] and Geertsma and DeKlerk[6] models are illustrated in Fig. 3.

The extension of the preceding simulations of the width profile to the case of a multilayered formation with different prevailing layer in-situ stresses necessitates development of width scaling curves. These curves incorporate layer elastic moduli ratio, vertical fracture penetration, and in-situ stress differentials across the layers. Figs. 4A and 4B reveal the developed fracture width scaling curves obtained from finite element simulations of the plane-strain model (Fig. 1). The previously developed isotropic width magnitudes can be converted to the layered case by multiplication with the pressure and tectonic stress scale factors and appropriate superposition.

The corresponding fracture height is obtained by use of the stress intensity factor concept. For the layered case, fracture penetration, arrest or interfacial propagation can depend on several factors, such as material property ratio, in-situ stress differences, effective bottomhole pressure magnitude, and interface friction/slip characteristics. Figs. 5A and 5B illustrate the computed stress intensity factors based on an $r^{1/2}$ singularity and induced by uniform crack pressure and differential tectonic stress. The interface is assumed to be bonded perfectly. The stress intensity trend in Fig. 5A departs considerably from that of Erdogan and Biricikoglu[16] for $H/h>1$, since in the latter the crack pressures are scaled to accommodate the imposed displacement compatibility for the closed form solution. Stress intensity factor

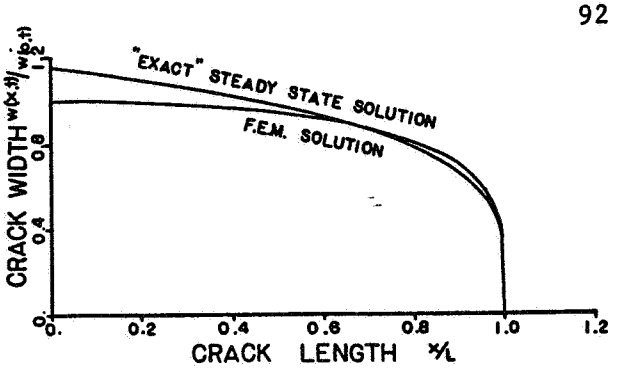

Fig. 2A—Comparison of steady-state width profiles.

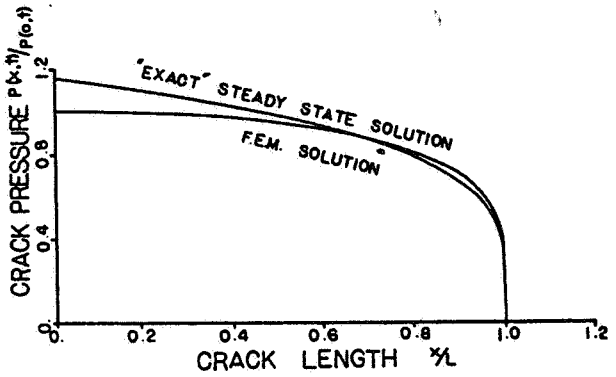

Fig. 2B—Comparison of steady-state pressure profiles.

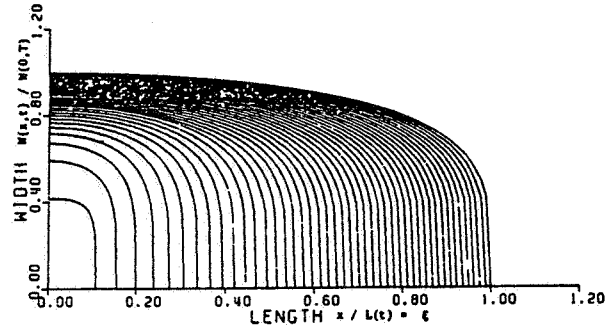

Fig. 2C—Transient width profile development for equal time steps.

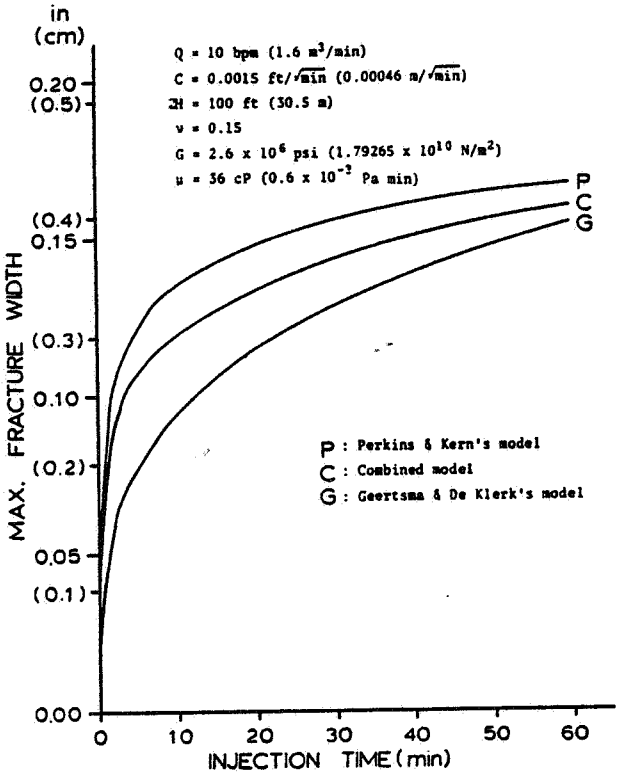

Fig. 3—Comparison of instantaneous maximum fracture width.

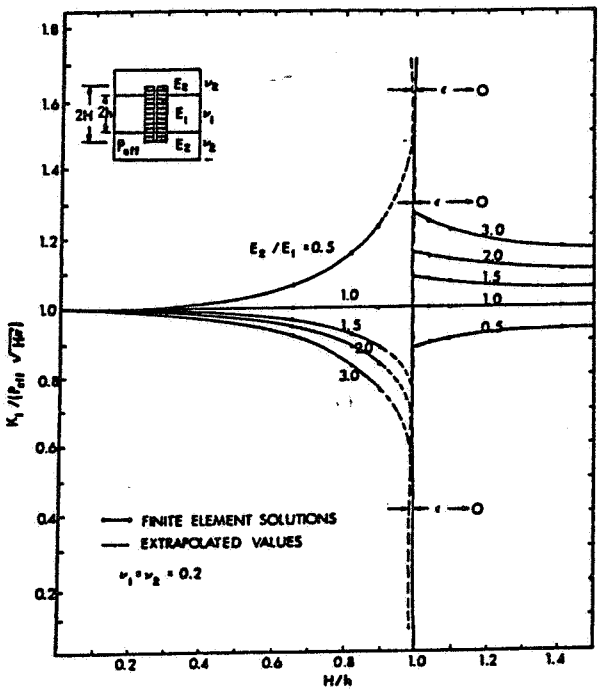

Fig. 5A—Stress intensity factor plots for induced pressures.

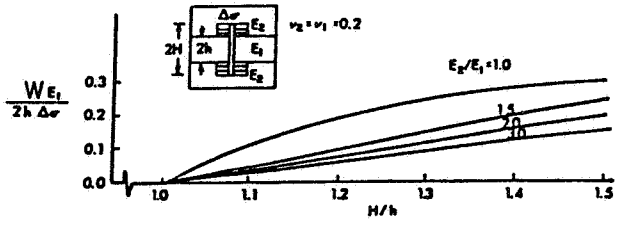

Fig. 4A—Average fracture width plots for induced pressures.

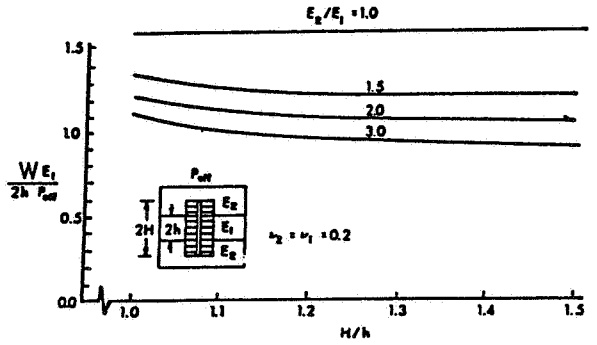

Fig. 4B—Average fracture width plots for in-situ stress differentials.

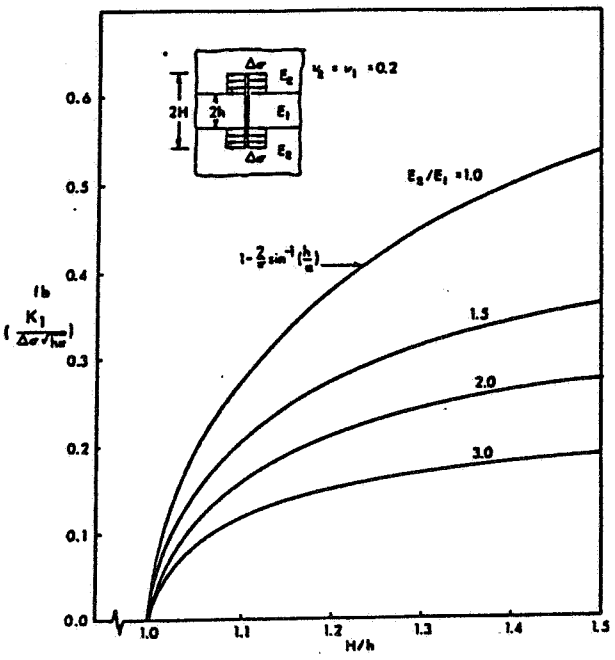

Fig. 5B—Stress intensity factor plots for in-situ stress differentials.

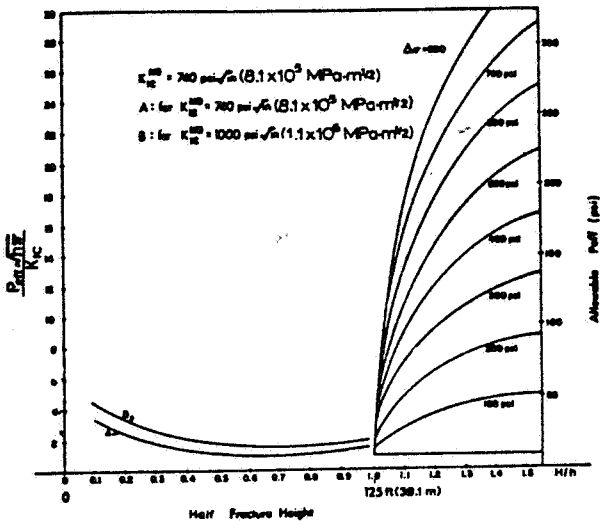

Fig. 6—Nondimensional pressure plots for fracture height estimation corresponding to well stratigraphy with $E_2 = 1.25E_1$. Fracture toughness for middle gray (MG) and middle brown (MB) shales are indicated.

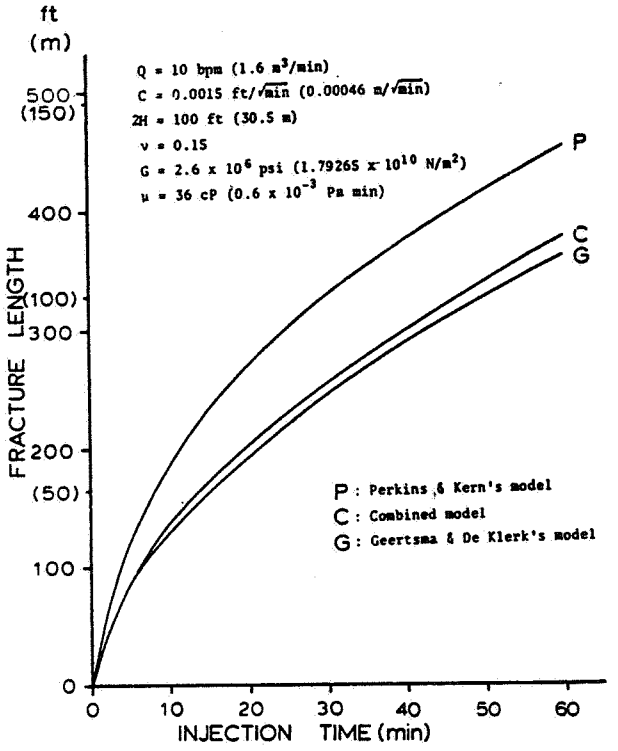

Fig. 7—Comparison of instantaneous fracture half-lengths.

magnitudes for the crack terminating at the interface are not indicated here because the stress singularity for this case is of the order $r^{\lambda_1^{(1)}-1}$, where $\lambda_1^{(1)}$ is the lowest eigenvalue of the characteristic equation involving ratios of the bimaterial constants.[17] However, the computed stress intensity factor magnitudes compare favorably with the values in the literature.[16,17] Fig. 6 reveals typical effective pressure vs. fracture height penetration curves deduced from Fig. 5A and 5B for $E_2/E_1 = 1.25$ and different tectonic stresses.

With the fracture width and height determined, the time-dependent fracture length can be computed from the imposed fracture fluid volume-balance requirements. Two different forms of fracture length simulations have been conducted. The first type of finite-difference fluid flow simulation entails application of Bernoulli's equation in the crack with suitable viscous friction losses governed by Reynolds number, coupled with use of Darcy's flow equation in the formation.[12] The other simulation iteratively solves the coupled Eqs. 1 and 4 with finite-element methods. Comparison of the predicted fracture lengths through use of the preceding data is illustrated in Fig. 7. The corresponding crack tip stress intensity factor obtained from

$$K_I(t) = \frac{1}{\sqrt{\pi L}} \int_{-L}^{L} \Delta p(x,t) \left(\frac{L+x}{L-x} \right)^{1/2} dx$$

$$= \frac{E}{4(1-\nu^2)L\sqrt{\pi L}} \int_{-L}^{L} W(x,t) \left(\frac{L+x}{L-x} \right)^{1/2} dx \quad \ldots\ldots (6)$$

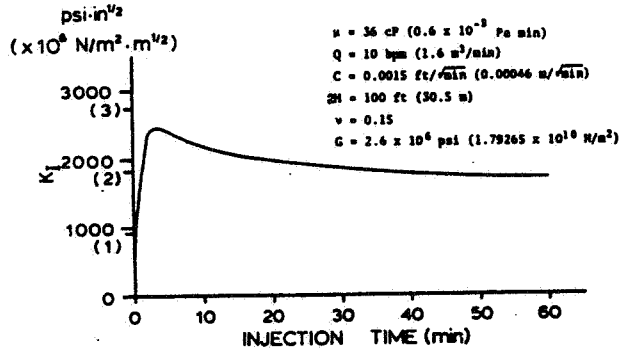

Fig. 8—Stress intensity factor variation with time.

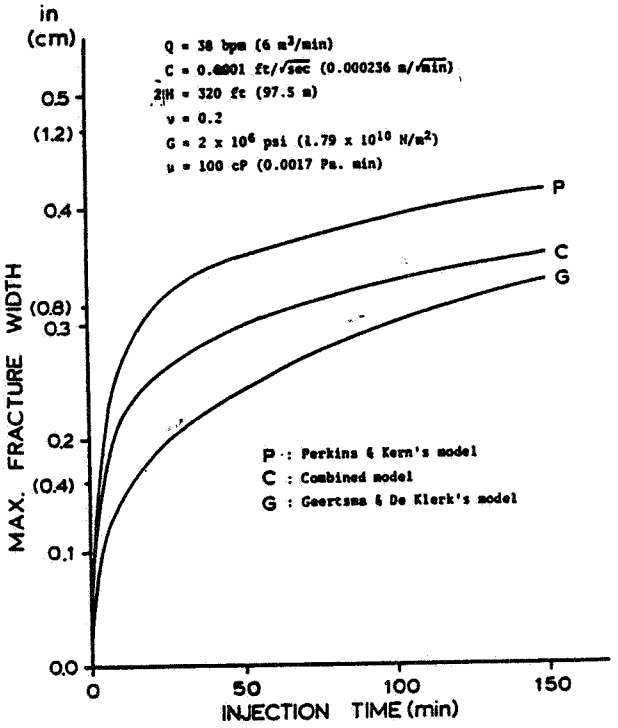

Fig. 9A—Comparison of instantaneous fracture widths for EGSP model.

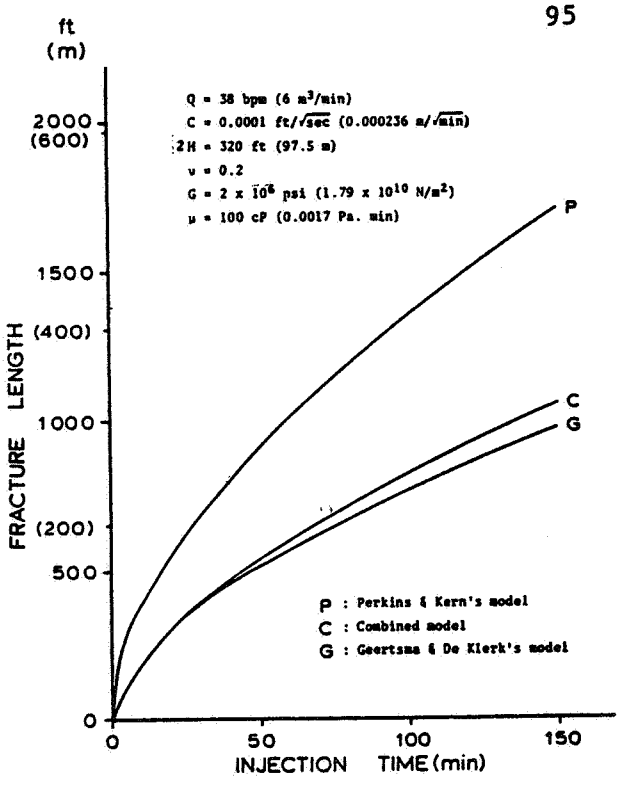

Fig. 9B—Comparison of instantaneous half fracture length for EGSP model.

is profiled in Fig. 8. Note that the crack opening mode stress intensity factor remains reasonably uniform during fracture propagation and that its value is representative of fracture toughness magnitudes for rocks.

As an example of the applicability of the developed model simulations to EGSP, computations on selected Columbia Gas Co. experiments[18] in Lincoln County, WV, have been performed for the simulated zones associated with Wells 20401, 20402, and 20403. In addition, criteria for vertical fracture containment of the fracture in the desired pay zone have been analyzed in terms of the prevailing in-situ stresses and the bottomhole treatment pressure. An example of foam fracturing of Well 20403 in the interval of 3,851 to 4,031 ft (1174 to 1229 m) is considered here. The computed in-situ stresses are σ_{OVBD}=3,590 psi (24.77 MPa), σ_{HMIN}=1,589 psi (10.96 MPa), and σ_{HMAX}=2,528 psi (17.44 MPa). The following is assumed: foam quality=0.80, adjusted flow rate=38 bbl/min (6.08 m^3/min), treatment time=150 minutes, effective pressure=341 psi (2.35 MPa), and shear modulus=2.0×10^6 psi (13.8GPa). Poisson's ratio=0.20, fluid viscosity=100 cp (100 Pa·s), and fluid loss coefficient =0.0001 ft/$s^{1/2}$ (0.0003 m/$s^{1/2}$) on the basis of reservoir porosity, permeability, and foam compressibility.

Available data on the differential in-situ stress across the formation layers[19] and material properties yield a fracture height of 320 ft (94.54 m). The computed maximum transient fracture width, employing the isotropic finite-element model simulations for Eqs. 1 and 4, are compared in Fig. 9A. The fracture width scaling factor for multilayer and differential in-situ stress is 0.76. The corresponding half fracture length plots are revealed in Fig. 9B. The simulated finite-element fracture length of 2,100 ft (640.08 m) compares with the simulated finite difference value of 2,050 ft (624.84 m) from the fracture area monographs.[12]

Mixed-Mode Hydraulic Fracture Model Simulations

Relatively few investigations have been conducted on mixed-mode fracture propagation in hydraulic fracture applications since a single vertical fracture generally is considered in the analysis. Simulations associated with dendritic fracturing, natural secondary fracture intersection, or vertical-crack interface joint interaction, however, entail mixed-mode conditions. The principal novelty in dendritic fracturing is the procedure of stopping the injection of fracture fluid and subsequently relieving the fluid pressure by allowing the fluid to flow back.[20] It is assumed in this analysis that secondary fractures are either created or initially present. With the increased occurrence of these secondary fractures, there is a greater tendency for branching fractures and formation spalling. Predictive calculations for spalling depths with specified minimum horizontal stress, tensile strength, pore pressure, and injection pressure have been reported.[13] Fig. 10 illustrates the selected dendritic fracture model with a primary fracture and secondary crack subjected to in-situ and pressure loading. Stress intensity factors, stress magnitudes, and associated contours for these loadings have been detailed using the finite-

TABLE 1—STRESS INTENSITY FACTORS FOR DENDRITIC FRACTURE MODEL

c/b	0.00			0.25			0.50			0.75			1.00		
Loading	P	S_x	S_y	P	S_x	S_y	P	S_x	S_y	P	S_x	S_y	P	S_x	S_y
$K_I^b/(P,S_x,S_y)\sqrt{a}$	0.762	-0.460	-0.320	0.730	-0.465	-0.280	0.672	-0.473	-0.217	0.590	-0.483	-0.120	0.489	-0.488	-0.021
$K_{II}^b/(P,S_x,S_y)\sqrt{a}$	-0.510	-0.030	0.547	-0.592	-0.040	0.630	-0.472	-0.026	0.500	-0.300	-0.130	0.360	-0.248	-0.025	0.257
$K_I^a/(P,S_x,S_y)\sqrt{a}$	-	-	-	1.025	0.210	-1.310	1.471	0.193	-1.681	1.710	0.150	-1.874	1.839	0.107	-1.966

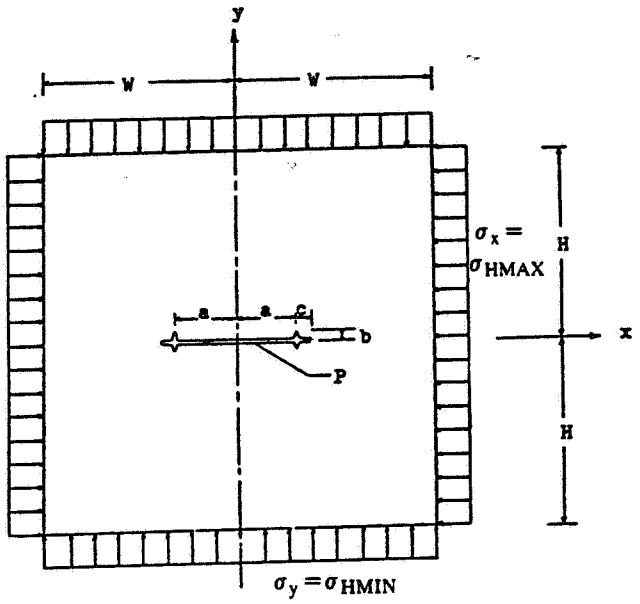

Fig. 10—Two dimensional dendritic fracture model.

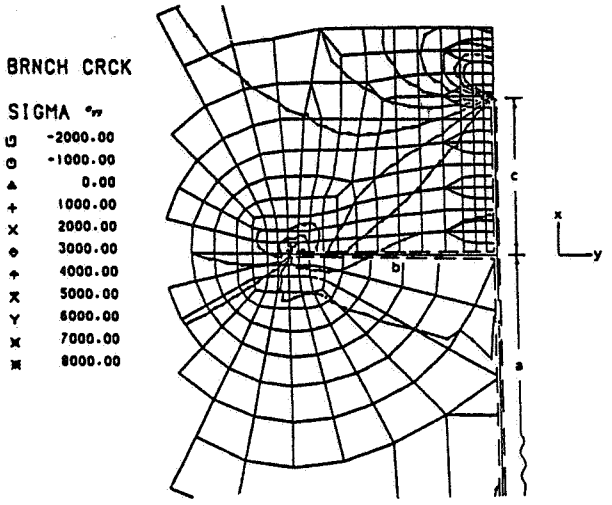

Fig. 11B—Stress contours σ_{yy} induced by fracture fluid pressure p = 1,000 psi (6.9 MPa).

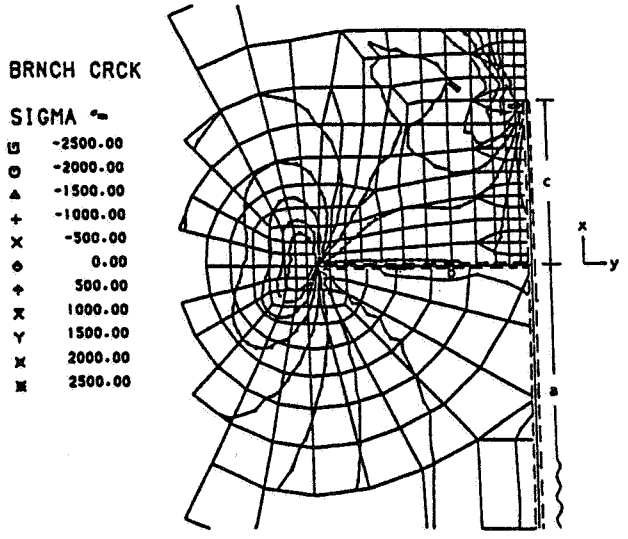

Fig. 11A—Stress contours σ_{xx} induced by fracture fluid pressure p = 1,000 psi (6.9 MPa).

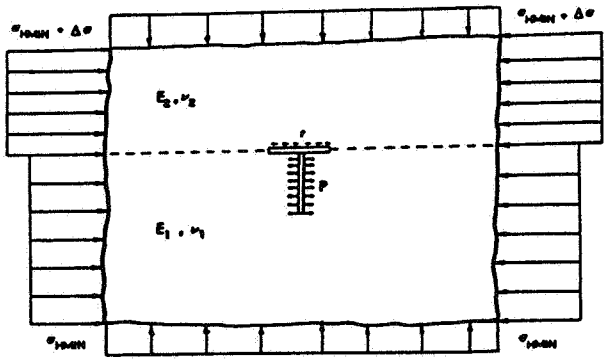

Fig. 12—Joint interaction at bi-material interface (E_2/E_1 = 1.25) and vertical-crack model.

element method. Table 1 shows the computed stress intensity factors for the pressure and in-situ stress loadings with $c/b=0$, 0.25, 0.50, 0.75, and 1.00. The magnitude of the normalized Mode II stress intensity factor significantly contributes to the secondary crack propagation. As an example, the analysis in Table 1 demonstrates that the secondary crack tip effective stress intensity factor $K_{eff}=[(K_I^b)^2+(K_{II}^b)^2]^{1/2}$ exceeds the corresponding primary tip value K_I^c for $0\le c/b\le 0.075$ with $S_x/P=2$ and $S_y/P=1$. Also, even for $c/b=1$, secondary crack propagation can be shown for selected ratios of in-situ stresses and crack pressure. Various mixed-mode fracture propagation criteria are presented in the subsequent text. Stresses induced by the fracture fluid loading are shown in Figs. 11A and 11B.

Another example of mixed-mode conditions results from the interaction of the induced vertical fracture with a bedding layer interface or joint. Fig. 12 illustrates a vertical crack intersecting a horizontal joint at the material interface. This bimaterial problem, in the absence of shear tractions, has been studied by Goree and Venezia.[21] The shear tractions at the joint interface coupled with the interaction of fracture fluid pressure and tectonic stresses produces conditions favorable to interfacial crack propagation. In this context, conditions for crack confinement, penetration, or interfacial crack propagation have been studied experimentally by Teufel and Clark.[22] For an interface crack subjected to uniform shear stress τ, the computed values of $K_I/\tau\sqrt{a}$ and $K_{II}/\tau\sqrt{a}$ at the joint tip are -0.198 and 0.593. These values, when superposed with the in-situ and fracture fluid pressure stress intensity, produce conditions similar to the dendritic fracture model, with $c/b=0$.

Mixed-Mode Fracture Criteria

Several mixed-mode fracture initiation criteria are available in the literature. Ingraffea[23] has presented a comparison of the maximum hoop tensile stress,[24] minimum strain energy density,[25] and maximum strain energy release rate[26] theories. In addition, a fracture criterion for rock media with crack closure and frictional effects has been developed by Advani and Lee.[27] These criteria are reviewed in the following.

Maximum Tensile Hoop Stress Theory.[24] In this theory, the fracture envelope is governed by

$$\cos\frac{\theta}{2}\left(K_I\cos^2\frac{\theta}{2}-\frac{3}{2}K_{II}\sin\theta\right)=K_{IC}, \quad \ldots\ldots(7a)$$

where the fracture initial angle, θ, is governed by

$$K_I\sin\theta+K_{II}(3\cos\theta-1)=0. \quad \ldots\ldots(7b)$$

Maximum Strain Energy Density Theory.[25]

$$K_I^2(3-4\nu-\cos\theta)(1+\cos\theta)$$
$$+4K_IK_{II}\sin\theta[\cos\theta-(1-2\nu)]$$
$$+K_{II}^2[4(1-\nu)(1-\cos\theta)+(1+\cos\theta)(3\cos\theta-1)]$$
$$=4(1-2\nu)K_{IC}^2, \quad \ldots\ldots(8a)$$

with θ determined from

$$K_I^2\sin\theta(2\cos\theta+4\nu-2)+4K_IK_{II}[\cos2\theta-(1-2\nu)\cos\theta]$$
$$+K_{II}^2(2-4\nu-6\cos\theta)\sin\theta=0 \quad \ldots\ldots(8b)$$

and imposition of the condition for stable crack propagation.

Maximum Strain Energy Release Rate Theory.[26] The fracture locus for this theory is defined by

$$K_I^4+6K_I^2K_{II}^2+K_{II}^4=K_{IC}^4. \quad \ldots\ldots(9)$$

Crack Closure and Frictional Effects Theory.[27] This theory, based on the maximum circumferential stress, includes the effects of crack closure and friction. The failure threshold is defined by

$$\left(\frac{K_{II}}{2K_{I_c}}\right)^2+\frac{K_I}{K_{IC}}=1. \quad \ldots\ldots(10)$$

Although this theory departs considerably from the aforementioned conventional theories, reasonable correlation of this theory with available experimental data for rock media with shear and compressive loading has been obtained.[27] Further controlled experiments on mixed-mode testing under simulated in-situ conditions are necessary. Fig. 13 illustrates the variation between the theories defined by Eqs. 7, 8, 9, and 10.

Conclusions

The theoretical simulations of the induced crack-opening mode and mixed-mode propagation responses provide interpretive, qualitative, and comparative information on the governing hydraulic-fracture mechanisms and fracture-geometry prediction. The transient vertical hydraulic fracture formulations and results for crack width, height, and length are applicable to layered formulations with differential in-situ stress. Vertical migration of the fracture in the overburden can be minimized by discrete control of the treatment pressure and/or alteration of the local effective minimum horizontal stress by means of successive pressure drawdown followed by sequential fracture propagation. The mixed-mode evaluations suggest a possible rationale for the effectiveness of dendritic fracturing for reservoirs with a large number of pre-existing systematic fractures, joint systems, and favorable horizontal in-situ stresses with local fracture fluid pressure modification.

Several characteristics for the assignment of conventional, foam, dendritic, or explosive treatments have recently emerged.[13,28-30] These factors include consideration of fracture density and extent, shale thickness, relative in-situ stresses, energy assist mechanisms, well cleanup, shale/fracture fluid interaction, proppant selection, and vertical fracture migration. Preliminary results indicate that correlation with the prevailing in-situ stress gradients or isotropy indices are promising diagnostic indicators for fracture-treatment selection and design. The comprehensive development of a cost-effective stimulation strategy, however, requires extensive and controlled

field testing with supportive laboratory and predictive analysis.

Nomenclature

a, b, c = crack dimensions for dendritic model
a^i = width vector component
$\dot{a}^*$ = time derivative of width vector
C = fluid loss coefficient
C_{ij} = transient width coefficient
E = elastic modulus
$F_i(t)$ = leakoff forcing function
G = shear modulus
h = half pay zone height
H = half fracture height
K_I, K_{II} = Mode I and II stress intensity factors, respectively
K_{IC} = critical Mode I stress intensity factor
L = fracture half length
N_i = interpolation function
p = crack pressure
Q = fracture fluid injection rate
S_x, S_y = horizontal in-situ stresses
t = time
$W(x,t)$ = fracture width
x = horizontal coordinate in fracture direction
y = transverse coordinate
θ = angular coordinate
μ = fluid effective viscosity
ν = Poisson's ratio
σ = stress component
$\Delta\sigma$ = horizontal in-situ stress differential
$\tau(x)$ = fluid loss delay time
τ = joint shear stress

Superscripts

i, j, k = indicial components
T = transpose

Subscripts

eff = effective magnitude
HMAX = horizontal maximum value
HMIN = horizontal minimum magnitude
i, j, k = indicial components
n = time step designator
OVBD = overburden magnitude

Acknowledgments

The support of the U.S. DOE under Contract No. DE-AC 21-79 MC 10514 is gratefully acknowledged. Computational assistance was provided by E.Y. Lee.

References

1. Komar, C.A.: "Development of a Rationale for Stimulation Design in the Devonian Shale," paper SPE 7166 presented at the SPE Regional Gas Technology Symposium, Omaha, NB, June 7-9, 1978.
2. Creman, S.P.: "Novel Fracturing Treatments in the Devonian Shale," *Proc.*, U.S.DOE First Eastern Gas Shales Symposium, Morgantown, WV (1977) 288-308.
3. McKetta, S.F.: "Investigation of Hydraulic Fracturing Technology in the Devonian Shale," *Proc.*, U.S. DOE Second Eastern Gas Shales Symposium, Morgantown, WV (1978) **1**, 25-34.
4. Perkins, T.K., and Kern, L.R.: "Widths of Hydraulic Fractures," *J. Pet. Tech.* (Sept. 1961) 937-949; *Trans.*, AIME, **222.**
5. Nordgren, R.P.: "Propagation of a Vertical Hydraulic Fracture," *Soc. Pet. Eng. J.* (Aug. 1972) 306-314; *Trans.*, AIME, **253.**
6. Geertsma, J., and DeKlerk, F.: "A Rapid Method of Predicting Width and Extent of Hydraulic Induced Fractures," *J. Pet. Tech.* (Dec. 1969) 1571-1581; *Trans.*, AIME, **246.**
7. Geertsma, J., and Haafkens, R.: "A Comparison of the Theories for Predicting Width and Extent of Vertical Hydraulically Induced Fractures," *J. Energy Resource Tech.* (March 1979) 8-19.
8. Brechtel, C., Abou-Sayed, A.S., and Clifton, R.J.: "In Situ Stress Determination in the Devonian Shales (IRA McCOY 20402) within the Rome Basin," Terra Tek Report TR 76-36, Salt Lake City (July 1976).
9. Daneshy, A.A.: "Hydraulic Fracture Propagation in Layered Formations," *Soc. Pet. Eng. J.* (Feb. 1978) 33-41.
10. Cleary, M.P.: "Primary Fractures Governing Hydraulic Fractures in Heterogeneous Stratified Porous Formations," paper ASME 78-PET-47 presented at the Energy Technology Conference and Exhibition, Houston, Nov. 5-9, 1978.
11. Anderson, G.D., Hanson, M.E., and Shaffer, R.J.: "Theoretical and Experimental Analyses of Hydraulic Fracturing," *Proc.*, U.S. DOE Third Eastern Gas Shales Symposium, Morgantown, WV (1979) 225-246.
12. Advani, S.H., GangaRao, H.V.S., Chang, H.Y., Komar, C.A., and Khan, S.: "Hydraulic Fracture Modeling for the Eastern Gas Shales Project," *Proc.*, U.S. DOE Second Eastern Gas Shales Symposium, Morgantown, WV (1978) **1**, 84-98.
13. Advani, S.H., Komar, C.A., Chang, H.Y., and Stonesifer, R.: "Rock Mechanics Aspects of Hydraulic Fracturing in the Devonian Shale," *Proc.*, U. of Missouri-Rolla, 21st U.S. Symposium on Rock Mechanics, The State of the Art in Rock Mechanics, Rolla, MO (1980) 701-709.
14. Oden, J.T.: *Finite Elements of Non-linear Continua*, McGraw-Hill Book Co. Inc., New York City (1972) 123.
15. Lee, E.Y.: "One Dimensional Finite Element Modal Simulator for Predicting Hydraulic Fracture Widths and Lengths," MS thesis, Ohio State U., Columbus (1981).

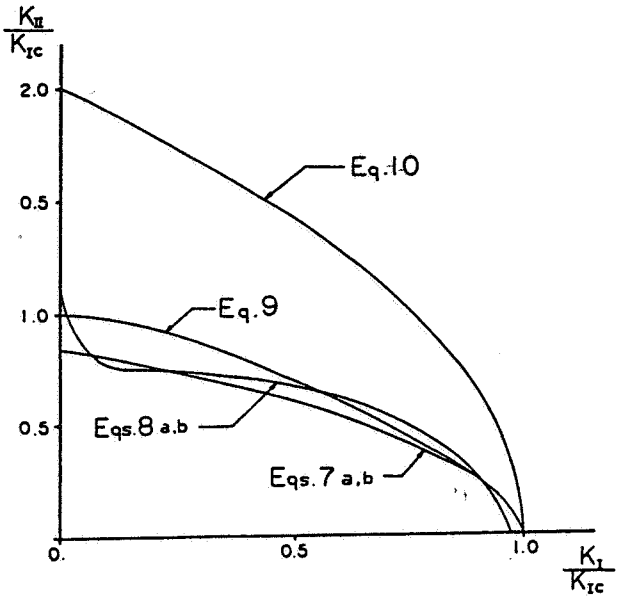

Fig. 13—Comparison of mixed-mode fracture envelopes.

16. Erdogan, F., and Biricikoglu, V.: "Two Bonded Half Planes with a Crack Going Through the Interface," *Int. J. Eng. Sci.* (1973) **11**, No. 7, 745–766.
17. Erdogan, F.: "Fracture Problems in Composite Materials," *Eng. Frac. Mech.* (1972) **4**, No. 4, 811–840.
18. Cremean, S., McKetta, S.F., Owens, G.L., and Smith, E.C.: "Massive Hydraulic Fracturing Experiments of the Devonian Shale in Lincoln County, West Virginia," Final Report to U.S. DOE, Contract E(46-1)-8014, Columbia Gas Co. (Jan. 1979).
19. Swolfs, H.S., Lingle, R., and Thomas, J.M.: "Determination of the Strain Relaxation and their Relation to Subsurface Stresses in the Devonian Shale," Terra Tek Final Report TR 77-12, Salt Lake City (Feb. 1977).
20. Kiel, O.M.: "Hydraulic Fracturing Process Using Reverse Flow," U.S. Patent No. 3,933,205 (1976).
21. Goree, J.G., and Venezia, W.A.: "Bonded Elastic Half-Planes with an Interface Crack and a Perpendicular Intersecting Crack that Extends Into the Adjacent Material—I," *Int. J. Eng. Sci.* (1977) **15**, No. 1, 1–17.
22. Teufel, L.W., and Clark, J.A.: "Hydraulic Fracture Propagation in Layered Rock: Experimental Studies of Fracture Containment," paper SPE 9878 presented at SPE/DOE Low-Permeability Gas Symposium, Denver, May 27–29, 1981.
23. Ingraffea, A.R.: "On Discrete Fracture Propagation in Rock Loaded in Compression," *Proc.*, U. C. Swansea, First Intl. Conference on Numerical Methods in Fracture Mechanics, Swansea, U.K. (1978) 235–248.
24. Erdogan, F., and Sih, G.C.: "On the Crack Extension in Plates Under In Plane Loading and Transverse Shear," *J. Basic Eng.* (Dec. 1963) 519–527.
25. Sih, G.C.: "Strain-Energy Density Factor Applied to Mixed Mode Crack Problems," *Int. J. Frac.* (1974) **10**, No. 3, 305–321.
26. Hellen, T.K., and Blackburn, W.S.: "The Calculation of Stress Intensity Factors for Combined Tensile and Shear Loading," *Int. J. Frac.* (Aug. 1975) 605–617.
27. Advani, S.H., and Lee, K.Y.: "Thermo-mechanical Failure Criteria for Rock Media," *Proc.*, U. of Texas, 20th U.S. Symposium on Rock Mechanics, Austin (1979) 19–25.
28. Komar, C.A., Yost, A.B., and Sinclair, A.R.: "Practical Aspects of Foam Fracturing in the Devonian Shale," paper SPE 8345 presented at the SPE 54th Annual Technical Conference and Exhibition, Las Vegas, Sept. 23–26, 1979.
29. Schmidt, R.A., Warpinski, N.R., and Cooper, T.W.: "In-Situ Evaluation of Several Tailored-Pulse Well Shooting Concepts," paper SPE 8934 presented at SPE/DOE Unconventional Gas Recovery Symposium, Pittsburgh, May 18–21, 1980.
30. Horton, A.I.: "A Comparative Analysis of Stimulations in the Eastern Gas Shales," Morgantown Energy Technology Center Report DOE/METC-145 (1981).

SI Metric Conversion Factors

ft	×	3.048*	E−01	= m
in.	×	2.54*	E+00	= cm
psi	×	6.894 757	E+03	= Pa

*Conversion factor is exact.

SPEJ

Original manuscript received in Society of Petroleum Engineers office March 17, 1980. Paper accepted for publication Sept. 11, 1981. Revised manuscript received Dec. 22, 1981. Paper (SPE 8941) first presented at the 1980 SPE/DOE Symposium on Unconventional Gas Recovery held in Pittsburgh May 18–21.

APPENDIX B

INTERFACE ELEMENT AND ROCK JOINT MODELING

J. K. Lee and H. Khattab
Department of Engineering Mechanics
The Ohio State University

INTERFACE ELEMENT AND ROCK JOINT MODELING

Most rock failures occur on defects on discontinuities embedded in the system. These defects may be rock joints, faults and interfaces. The behavior of these discontinuities result in debonding and slip along the interface. The term debonding describes the separation of the two adjacent blocks and the slip defines the relative motion along the joint surface or fault when the shearing forces exceeds the shear strength of the joint. To account for this discontinuity in the finite element analysis of rock systems, a joint element is used between the blocks. The joint element stiffness properties are presented in this section.

Consider an interface between two materials and oriented along the s-axis as shown in Fig. B.1.

The displacement along the joint is assumed as linear and is given by

$$u = b_1 + b_2 s$$
$$v = b_3 + b_4 s \qquad \text{(B.1)}$$

when the constants b_1 b_4 are determined in terms of the nodal displacements, top and bottom displacements can be written as

$$u_{top} = \frac{1}{2}(u_3 + u_4) + \frac{s}{\ell}(u_3 - u_4)$$
$$v_{top} = \frac{1}{2}(v_3 + v_4) + \frac{s}{\ell}(v_3 - v_4)$$
$$u_{bot} = \frac{1}{2}(u_1 + u_2) + \frac{s}{\ell}(u_2 - u_1) \qquad \text{(B.2)}$$
$$v_{bot} = \frac{1}{2}(v_1 + v_2) + \frac{s}{\ell}(v_2 - v_1)$$

The relative displacements of the two faces measured at the joint center can be expressed as

$$\{w_j\} = \begin{Bmatrix} u_{top} - u_{bot} \\ v_{top} - v_{bot} \end{Bmatrix} = \begin{Bmatrix} \Delta u_o \\ \Delta v_o \end{Bmatrix} \tag{B.3}$$

Substituting (B.2) in (B.3), we get

$$\{w_j\} = \frac{1}{2} \begin{bmatrix} -A & 0 & -B & 0 & B & 0 & A & 0 \\ 0 & -A & 0 & -B & 0 & B & 0 & A \end{bmatrix} \begin{Bmatrix} u_1 \\ v_1 \\ \vdots \\ u_4 \\ v_4 \end{Bmatrix} \tag{B.4}$$

where $A = 1 - \frac{2s}{\ell}$

$B = 1 + \frac{2s}{\ell}$

or simply,

$$\{w_j\} = \frac{1}{2}[N]\{q\} \tag{B.5}$$

The forces per unit length, {p}, acting through the displacements, {w}, are related through the joint stiffness per unit length [k] by

$$\{p\} = [k]\{w\} \tag{B.6}$$

here $\{p\} = \begin{Bmatrix} p_s \\ p_n \end{Bmatrix}$

and $[k] = \begin{bmatrix} k_s & 0 \\ 0 & k_n \end{bmatrix}$

The normal and tangential stiffnesses k_n and k_s are determined from direct shear test. The stored energy E is given by

$$E = \frac{1}{2}\int_{-\ell/2}^{\ell/2} \{w\}^T\{p\}ds \qquad (B.7)$$

$$= \frac{1}{2}\int_{-\ell/2}^{\ell/2} \{q\}^T[N]^T[k][N]\{q\}\, ds$$

from which the stiffness matrix for the joint element oriented along s-direction is identified as

$$[K]' = \int_{-\ell/2}^{\ell/2} [N]^T[k][N]ds \qquad (B.8)$$

The global stiffness (referring to the global x- and y-axis) matrix [K] of the joint element can be obtained by the transformation

$$[K] = [R]\,[K]'\,[R]^T \qquad (B.9)$$

where [R] defines the transformation between s-n axis and x-y axis.

The normal and tangential stiffness used in the stiffness matrix are usually determined by laboratory tests. These constants play a vital role in the finite element stress analysis of the jointed rock system and they are to be properly determined for a reasonable result. Further details can be found in Refs. [B.1,2].

An interface element such as this, according to published results and our experience, can model opening and/or slipping modes relatively well. However, material penetration can occur under compression as shown in Fig. B.2. When penetration occurs during an analysis, stress fields below the interface can be erroneous when major loading is from the top portion. To avoid such physically unrealistic penetration, one must assign a small thickness Δh for the interface element and an iterative solution process must be used. In general the normal stiffness k_n would be greater in compression than in tension.

REFERENCES

B.1 R.E. Goodman, R.L. Taylor and T.L. Brekke, "A Model for the Mechanics of Jointed Rock," Journal of the Soil Mechanics and Foundations Division Proc. ASCE, pp. 637-659, May, 1968.

B.2 T.J. Chung and J.K. Lee, "Incremental Plasticity Theory Applied to Boundary Value Problems in Soil," Proc. Conf. Applications of Finite Element Method in Geotechnical Engineering, USAEWES, 1972.

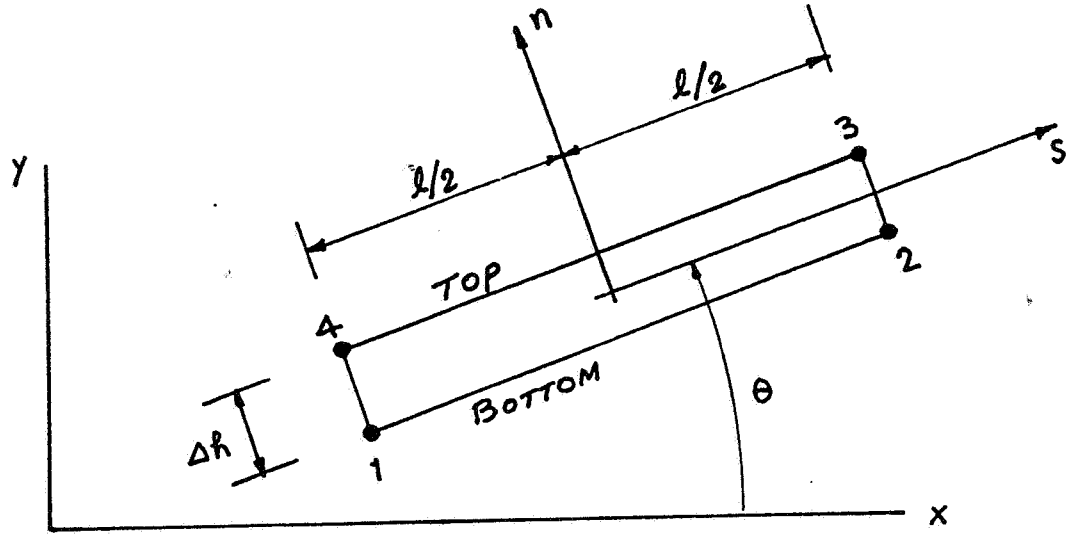

Figure B.1 Interface element geometry.

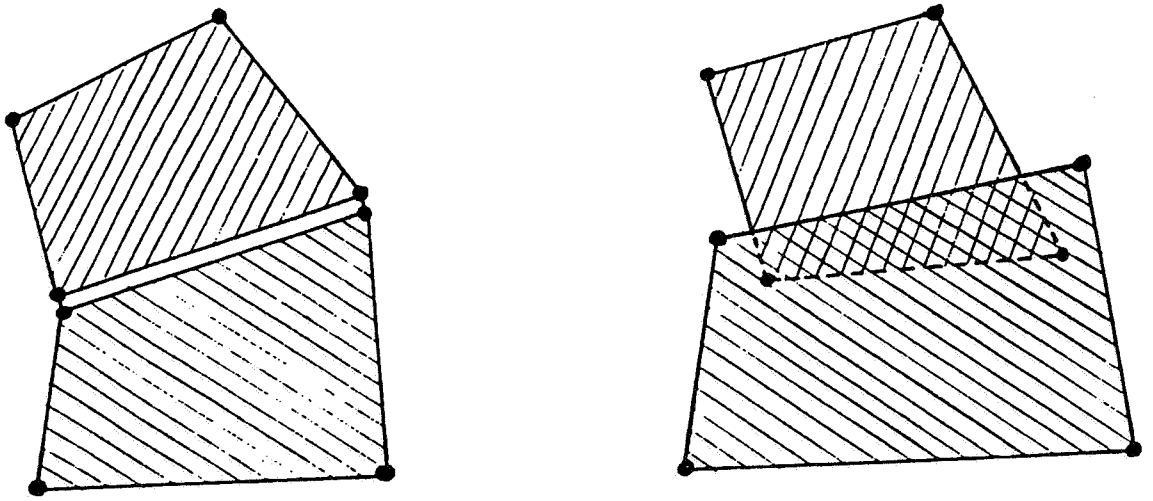

Figure B.2 Possible penetration mode.

APPENDIX C

EFFECT OF VERTICAL FRACTURE HEIGHT ON TRANSIENT WELL FLOW BEHAVIOR

D.A. Mendelsohn[1] and M.Y. Soliman[2]

[1]Department of Engineering Mechanics
The Ohio State University

[2]Chemical Research Department
Halliburton Services

THE EFFECT OF VERTICAL FRACTURE HEIGHT ON TRANSIENT WELL FLOW BEHAVIOR

(A1) Problem Formulation

The problem of unsteady single-phase Darcy flow from a porous reservoir of finite height into a finite conductivity vertical hydraulic fracture is shown in Fig. 1 for one-half of the fracture. The reservoir is infinite in the x'-y' directions and of finite height H' in the z'-direction. The fracture has width w in the y'-direction and has a rectangular contour as shown. Conductivities, k, compressibilities, c, and porosities, ϕ will be subscript free when referring to the reservoir and will have the subscript f when referring to the fracture. The following assumptions are made concerning the flow in the reservoir and fracture.

(a) Analysis is limited to short time periods following the onset of flow

(b) Flow in both reservoir and fracture is governed by Darcy's law of flow in porous media

(c) The fracture width is very narrow compared to the height and length.

(d) The fracture height ($h'=z'_u - z'_\ell$) may be less than or equal to the reservoir height H'.

(e) The reservoir boundaries, $z'=0$ and $z'=H'$ are impermeable.

(f) The fluid is a compressible Newtonian fluid.

(g) The pressure at the wellbore ($x'=y'=0$) is held constant (P_o).

Assumptions (e,g) are not restrictive as other cases are easily treated in the same manner. Assumptions (a,d) lead to two-dimensional planar flow in planes of constant x'. This is the analog of linear flow (y'-only) for the short time flow when $h'=H'$. Assumption (a) also means that all the fluid

will enter the wellbore through the fracture only. Also, there is no flow in the fracture in the y' direction due to Assumption (c).

The following common non-dimensionalization procedure is introduced for the space variables, time and fracture and reservoir pressures, (see e.g. [1] for the case of constant wellbore pressure):

$$(x,y,z) = \frac{1}{x_f}(x',y',z') \tag{1}$$

$$t = \frac{k_r t'}{\phi_r \mu c_r x_f^2} \tag{2}$$

$$P_f(x,z) = \frac{1}{P_o} P_f'(x',z') \tag{3}$$

$$P_r(y,z) = \frac{1}{2P_o} P_r'(y',z') \tag{4}$$

where a prime denotes a dimensional variable or pressure and the subscripts f and r refer to the fracture and reservoir respectively. The constants k, ϕ, c refer to permeability, porosity and compressibility and μ is the fluid viscosity, assumed the same in the reservoir and fracture. The fracture length, width and height are denoted by x_f, w and h'. All quantities of length are non-dimensionalized like the space-coordinates in (1), e.g. $H=H'/x_f$, $z_\ell=z'/x_f$ ... P_o is the prescribed wellbore dimensional pressure.

The non-dimensional coupled boundary value problems describing flow in the fracture and reservoir may now be written. The fracture flow equation is [2]

$$\frac{\partial^2 P_f}{\partial x^2} + \frac{\partial^2 P_f}{\partial z^2} + \frac{2}{k_D w_D}\left[\frac{\partial P_r}{\partial y}\bigg|_{y=o}\right] = \frac{1}{\eta_D}\frac{\partial P_f}{\partial t} \tag{5}$$

for $0 < x < 1$ and $z_\ell < z < z_u$. The initial condition is

$$P_f = 0 \quad , \quad t = 0 \qquad \begin{matrix} 0 < x < 1 \\ z_\ell < z < z_u \end{matrix} \tag{6}$$

and the boundary conditions are

$$\left.\begin{aligned} P_f &= 1 \quad , \quad x = 0 \\ \frac{\partial P_f}{\partial x} &= 0 \quad , \quad x = 1 \end{aligned}\right\} \quad z_\ell < z < z_u \quad , \quad t>0 \tag{7, 8}$$

$$\frac{\partial P_f}{\partial z} = 0 \quad , \quad z = z_\ell, z_u \qquad 0 < x < 1 \quad , \quad t>0 \tag{9}$$

The constants k_D, w_D and η_D are given by

$$k_D = k_f/k_r \ , \ w_D = w/x_f \ , \ \eta_D = \left(\frac{\phi_r}{\phi_f}\right)\left(\frac{c_r}{c_f}\right)k_D \tag{10}$$

The last term on the left-hand-side of (5) is the non-dimensional flow rate from the reservoir into the fracture. The reservoir flow equation is

$$\frac{\partial^2 P_r}{\partial y^2} + \frac{\partial^2 P_r}{\partial z^2} = \frac{\partial P_r}{\partial t} \tag{11}$$

for $0 < y < \infty$ and $0 < z < H$. The initial condition is

$$P_r = 0 \quad , \quad t = 0 \quad , \quad \begin{matrix} 0 < y < \infty \\ 0 < z < H \end{matrix} \tag{12}$$

and the mixed boundary conditions are, after considering the symmetry about the plane y=0 and the position of the fracture,

$$\left.\begin{aligned} \frac{\partial P_r}{\partial y} &= 0 \qquad \begin{matrix} 0 < z < z \\ z_u < z < H \end{matrix} \\ P_r &= P_f \qquad z_\ell < z < z_u \end{aligned}\right\} \quad y=0 \quad , \quad t>0 \tag{13, 14}$$

$$\frac{\partial P_r}{\partial z} = 0 \qquad z=0 \text{ and } z=H \ , \ 0 < y < \infty, \quad t>0 \tag{15}$$

$$\lim_{y\to\infty} P_r = 0 \quad , \quad 0 < z < H \quad , \quad t>0 \ . \tag{16}$$

where $H=H'/x_f$ is the non-dimensional reservoir height. Note that coupling is through the pressure continuity condition (14) and through the source term in (5). Hence, while P_r depends explicitly on y and z only, it will depend implicitly on x through the condition (14). Figure 2 illustrates planar views of the fracture problem (x-z plane) and the reservoir problem (yz plane), drawn for any plane of constant x.

(A2) Derivation of Integral Equations

First, the time variable is eliminated by applying a Laplace transform to each of equations (5), (7-9), (11), and (13-16), noting the initial conditions (6) and (12). Defining for any function g(t), its Laplace transform, $\bar{g}(s)$,

$$\bar{g}(s) = \int_o^\infty g(t)e^{-st}dt \tag{17}$$

the transformed versions of equations (5), (7-9), become

$$\frac{\partial^2 \bar{P}_f}{\partial x^2} + \frac{\partial^2 \bar{P}_f}{\partial z^2} - \gamma \bar{P}_f = \alpha \left.\frac{\partial \bar{P}_r}{\partial y}\right|_{y=o} \tag{18}$$

for $0 < x < 1$ and $z_\ell < z < z_u$,

$$\left.\begin{aligned} \bar{P}_f &= 1/s \quad , \quad x=0 \\ \frac{\partial \bar{P}_f}{\partial x} &= 0 \quad , \quad x=1 \end{aligned}\right\} \quad z_\ell < z < z_u \tag{19, 20}$$

$$\frac{\partial P}{\partial z} = 0 \quad , \quad z=z_\ell \text{ and } z=z_u \, , \; 0 < x < 1 \, . \tag{21}$$

The constant α and the function γ of the transform variable are given by

$$\alpha = \frac{-2}{k_D w_D} \quad , \quad \gamma = \frac{s}{\eta_D} \quad . \tag{22}$$

Equations (11) and (13-16) become

$$\frac{\partial^2 \overline{P}_r}{\partial y^2} + \frac{\partial^2 \overline{P}_r}{\partial z^2} - s\overline{P}_r = 0 \tag{23}$$

for $0 < y < \infty$ and $0 < z < H$,

$$\left.\begin{aligned} \frac{\partial \overline{P}_r}{\partial y} = 0 \qquad & 0 < z < z_\ell \\ & z_u < z < H \end{aligned}\right\} \quad y = 0 \tag{24}$$

$$\overline{P}_r = \overline{P}_f \qquad z_\ell < z < z_u \tag{25}$$

$$\frac{\partial \overline{P}_r}{\partial z} = 0 \qquad z = 0 \text{ and } z=H , \qquad 0 < y < \infty \tag{26}$$

$$\lim_{y \to \infty} \overline{P}_r = 0 \qquad 0 < z < H \ . \tag{27}$$

The reservoir problem is formulated first, assuming that the function $\overline{P}_f(z,s)$ is known for the time being. The following solution to the differential equation (23) is assumed

$$\overline{P}_r = \int_0^\infty A(\xi) \frac{\cosh(\nu z)}{\cosh(\nu H)} \cos(\xi y) d\xi + \int_0^\infty C(\xi) e^{-\nu y} \cos(\xi z) \frac{d\xi}{\xi \nu} \tag{28a}$$

where

$$\nu = (\xi^2 + s)^{1/2} \ . \tag{28b}$$

which already satisfies condition (26a). Upon making the substitution

$$C(\xi) = - \int_{z_\ell}^{z_u} \phi(u) \sin(\xi u) du \ , \tag{29}$$

and imposing that

$$\int_{z_\ell}^{z_u} \phi(u) du = 0 \tag{30}$$

it may be shown that for any integrable function $\phi(u)$, $\left.\frac{\partial \overline{P}_r}{\partial y}\right|_{y=0}$ is zero outside of

$z_\ell < z < z_u$ and non-zero in this region, so conditions (24) are automatically satisfied for any $\phi(u)$. Application of the Fourier cosine transform to the condition (26b) yields the result

$$A(\xi) = \frac{\text{ctnh}(\nu H)e^{-\nu H}}{\nu^2} \int_{z_\ell}^{z} \sinh(\nu u)\phi(u)du \tag{31}$$

The ensuing expression for $\overline{P}_r$ in terms of the unknown function ϕ may be shown to vanish in the limit $y \to \infty$, hence (27) is satisfied as well, leaving the following integral equation of Fredholm type representing the pressure condition (25),

$$\int_{z_\ell}^{z_u} K(z,u)\phi(x,u)du = \overline{P}_f(x,z) \tag{32a}$$

valid over the region $0 < x < 1$, $z_\ell < z < z_u$. The kernel is given by

$$K(z,u) = \int_o^\infty \frac{e^{-\nu H}}{\nu^2 \sinh(\nu H)} \sinh(\nu u)\cosh(\nu z)d\xi - \int_o^\infty \frac{\sin(\xi u)\cos(\xi z)}{\nu\xi} d\xi \ . \tag{32b}$$

If $\overline{P}_f$ were known, the integral equation could be solved easily for a grid of values over the fracture for ϕ. Also, note that

$$\left.\frac{\partial \overline{P}_r}{\partial y}\right|_{y=o} = \frac{\pi}{2}\int_z^{z_u} \phi(u)du \tag{33}$$

for $z_\ell < z < z_u$, therefore ϕ may be interpreted as a flow intensity or density function defining for each plane of constant x the flow intensity per unit fracture height and is a function of position z, $z_\ell < z < z_u$.

The solution to the fracture problem (18-21) may be solved by assuming the total fracture pressure is given by

$$\overline{P}_f = \overline{P}_H + \overline{P}_p \tag{34}$$

where $\overline{P}_H$ is the solution to (18-21) for the right hand side of (18) identically zero and $\overline{P}_p$ is the solution to (18-21) for the right hand side of (19) identically zero. The homogeneous solution $\overline{P}_H$ is found immediately to be

$$\bar{P}_H = \frac{1}{s}\left[\left(1 - \frac{e^{\sqrt{\gamma}}}{2\cosh(\sqrt{\gamma})}\right)e^{\sqrt{\gamma}x} + \frac{e^{\sqrt{\gamma}(1-x)}}{2\cosh(\sqrt{\gamma})}\right] \tag{35}$$

The particular solution $\bar{P}_p$ is found by assuming the Fourier series representation

$$\bar{P}_p = \sum_{k=o}^{\infty}\sum_{j=o}^{\infty} P_{kj}\sin\left[(2k+1)\frac{\pi}{2}x\right]\cos\left[\pi j\frac{z-z_\ell}{h}\right] \tag{36}$$

where $h = z_u - z_\ell$ is the non-dimensional fracture height. This solution automatically satisfies the boundary conditions for the particular problem and if the coefficients are chosen as

$$P_{kj} = \frac{-f_{kj}}{\left[(2k+1)^2\frac{2\pi^2}{4} + j^2\frac{2\pi^2}{h^2} + \gamma\right]} \tag{37}$$

where the Fourier coefficients of the right hand side of (18) are given by

$$f_{kj} = \frac{4}{h}\int_o^1\int_{z_\ell}^{z_u}\left[\alpha\frac{\partial\bar{P}_r}{\partial y}\bigg|_{y=o}\right](x,z)\sin\left[(2k+1)\frac{\pi}{2}x\right]\cos\left(\pi j\frac{z-z_\ell}{h}\right)dzdx\,, \tag{38}$$

then the differential equation is also satisfied.

Noting (33) and substituting (38) into (37), then into (36) and along with (35) into (34) gives the pressure in the fracture in terms of ϕ. Substitution of this $\bar{P}_f$ form into (32a) yields the two-dimensional integral equation

$$\int_{z_\ell}^{z_u} K(z,z')\phi(x,z')dz' + \int_o^1\int_{z_\ell}^{z_u} L(x,z;x',z')\phi(x',z')dz'dx' = \bar{P}_H(x) \tag{39}$$

for $0 < x < 1$ and $z_\ell < z < z_u$. Dummy integration variables are denoted by primes, not to be confused with the original dimensional variables of Figure 1.

The following additional equation obtained from (30) must also be applied over $0 < x < 1$

$$\int_{z_\ell}^{z_u}\phi(x,z')dz' = 0\,. \tag{40}$$

The kernel $K(z,z')$ is given in (32b) and the kernel $L(x,z;x',z')$, after much

manipulation and evaluation of the summation over j in closed form, is given

$$-\frac{L(x,z;x',z')}{\alpha h} = \sum_{k=o}^{\infty} [h(FS_k + FA_k) + \frac{4z'}{\pi^3}] \frac{\sin[(2k+1)\frac{\pi}{2} x]\sin[(2k+1)x']}{a_k^2} \tag{41}$$

where

$$FS_k = \frac{(z_u+z_\ell)}{h} - \frac{(z'+z)}{h} - \frac{\sinh[a_k \frac{\pi}{h}(z_u+z_\ell-z'-z)]}{\sinh(a_k\pi)} \tag{42a}$$

$$FA_k = \text{sgn}(z'-z) \{ 1 - \frac{|z'-z|}{h} - \frac{\sinh[a_k \frac{\pi}{h}(z_u+z_\ell-|z'-z|)]}{\sinh(a_k\pi)} \} \tag{42b}$$

and

$$a_k^2 = (2k+1)^2 \frac{\pi^2}{4} + \gamma \ . \tag{42c}$$

(A3) Numerical Analysis

The integral equation (39) with subsidiary condition (40) is solved by assuming the integrals over x' and z' are approximated by finite Gauss-Legendre quadratures using the integration points

$$\begin{aligned} &x_m && m = 1,M \\ &z_n && n = 1,N \ . \end{aligned} \tag{43}$$

If the free collocation variables x and z are also assumed to take on the values x_m and z_n then (39) and (40) will yield M*(N+1) equations for the M*N unknowns

$$\phi(x_m,z_n) \qquad m = 1,M \qquad n=1,N \tag{44}$$

Since the behavior of the function ϕ is expected to be smooth for z in the center of the fracture, the equation corresponding to $z = z_{N+1/2}$ obtained from (39) will be dropped from the formulation and the equation representing (40) will be put in its place. Also N will be restricted to be odd.

The calculation of the kernels K and L at the appropriate values of x, z, x' and z' is straightforward. The integrand of the first term of K in (32b) are suitable for approximation by a Gauss-Laguerre quadrature and except for values of z'+z close to $2z_u$ the convergence is quite fast and even for z'+z close to $2z_u$ convergence is acceptable for reasonably small values of N. The second term of K in (32b) may be transformed into a semi-infinite exponential integral whose integrand decays at best as $\exp[-c_o\cosh(\xi)]$ and at worst as $\exp[-\xi]$, where ξ is the variable of integration and c_o is a constant, and therefore is also suitable for application of the Gauss-Laguerre quadrature and has excellent convergence properties. The summation in L involves terms that decay as slowly as $(1/(2k+1)^2)$ and as quickly as $\exp[-c_o(2k+1)^2]/(2k+1)^2$. It is straightforward to improve the convergence of the poorly converging terms by subtraction of appropriate terms whose sum is known.

The solution of the ensuing (NxM)x(NxM) linear system is carried out by standard techniques. Once the values (x_m, z_n) are known, the transformed pressure in the fracture may be found by noting (33) and approximating the integrals in (38) again by Gaussian quadrature and substituting successively into (37) and (36) and along with (35) into (34). This of course involves a double summation over k and j. However, the quantity of interest is the net transformed non-dimensional wellbore flow rate, or

$$\overline{Q}(s) = \int_{z_\ell}^{z_u} [\frac{\partial \overline{P}_f}{\partial x}(x,z;s)]_{x=o} dz \qquad (45)$$

The differentiation and integration may both be carried out in closed form and one is left with outer double finite sums over x_m and z_n and inner infinite sums over k which converge even faster than similar terms of the kernel L. The above procedure is repeated for each value of s to be used in the Laplace transform inversion routine which itself will involve a finite sum over values

of s of the function $\overline{Q}(s)$ given in (45). The inversion scheme is based on a method due to Bellman, et.al. [3].

REFERENCES

[1] Heber-Cinco, L.; F. Samaniego, V.; N. Dominquez, A., "Transient pressure behavior for a well with a finite-conductivity vertical fracture," Soc. Pet. Eng. J., Vol. 18, 1978, p. 253-264.

[2] Matthews, C.S. and Russel, D.J., "Pressure build-up and flow tests in wells," Soc. Pet. Eng. Monograph, Vol. 1, 1967, p. 4-8.

[3] Bellman, R.E., et.al., Numerical Inversion of the Laplace Transform, American Elsevier, New York, 1966.

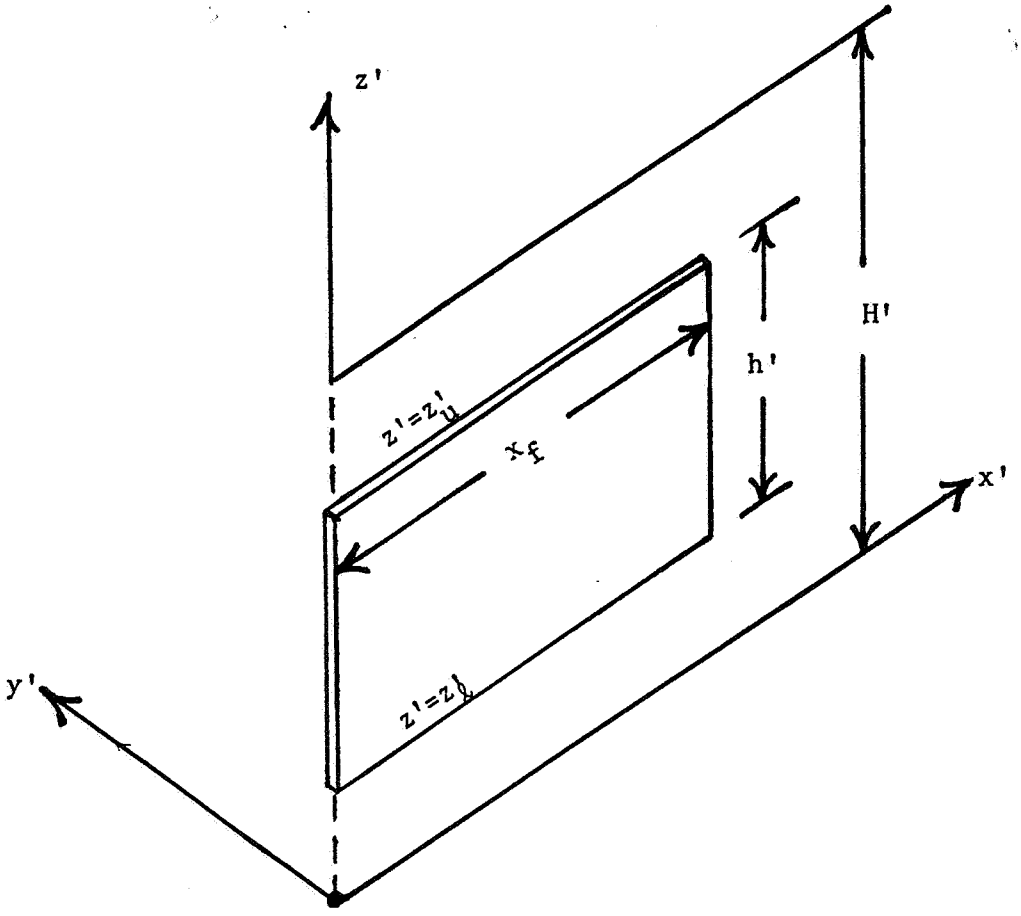

Figure 1. A rectangular fracture of width w $[0<x'<x_f,\ z'_\ell<z'<z'_u]$ in a semi-infinite slab reservoir $[-\infty<y'<\infty,\ 0<x'<\infty,\ 0<z'<H']$. Wellbore is located along the z' axis.

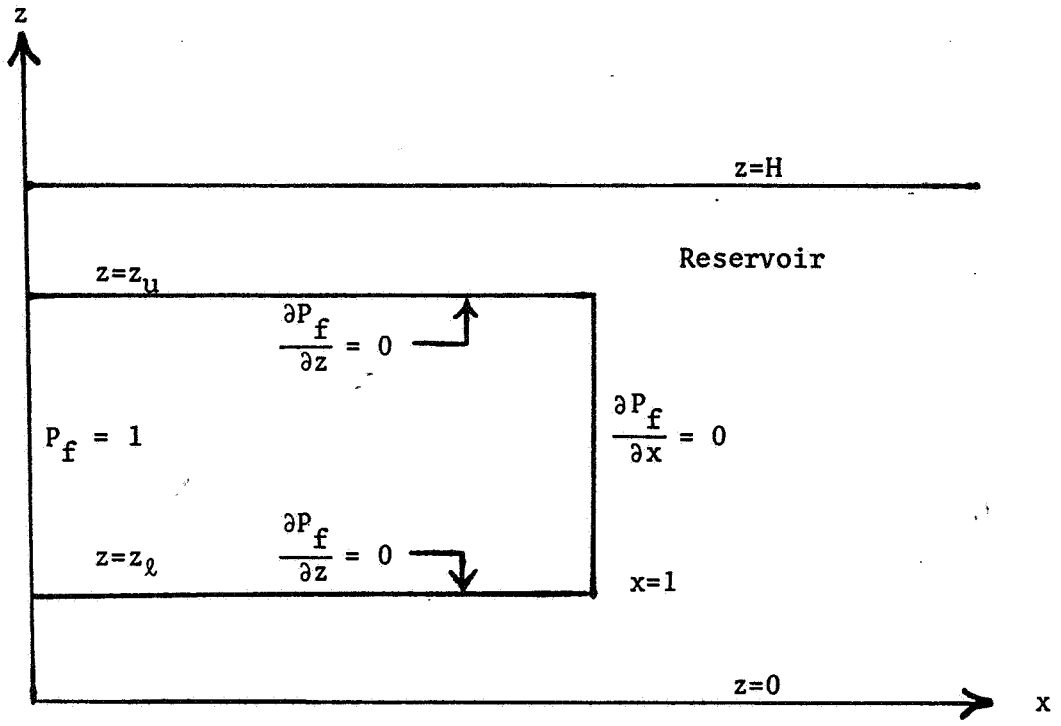

(a) Fracture Plane, y = 0

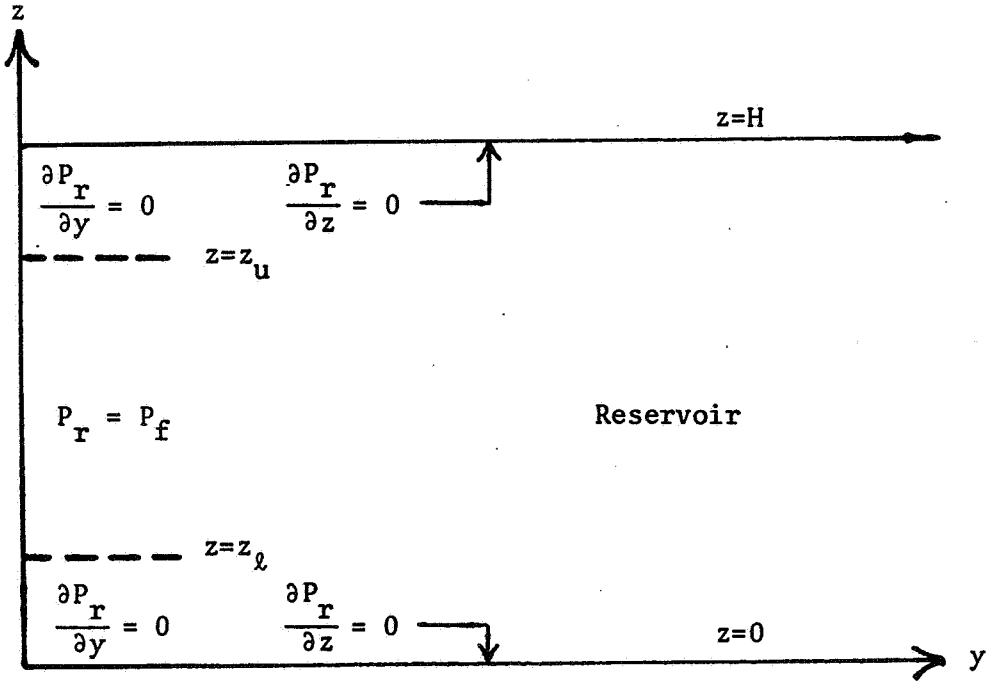

(b) Plane x = constant, 0<x<1

Figure 2. Planar views of the fracture (a) and reservoir (b) boundary value problems.

APPENDIX D

PRELIMINARY ANALYSIS OF GEOLOGIC PARAMETERS CONTROLLING FRACTURE IN THE DEVONIAN SHALES FOR KANAWHA COUNTY, WEST VIRGINIA

Anthony Andrews
The Ohio State University

PRELIMINARY ANALYSIS OF GEOLOGIC PARAMETERS CONTROLLING FRACTURE IN THE DEVONIAN SHALES FOR KANAWHA COUNTY, WEST VIRGINIA

This Appendix reported supplementary information and results obtained by Mr. A. Andrews. The detailed results will be presented in an M.S. thesis.

In accordance with elasticity theory, the horizontal stresses at a given depth are related to the overburden stress by a factor of $\nu/(1-\nu)$. In situ stress measurements have demonstrated that this is not true, as evidenced by the anisotropic stress conditions depicted in Plates 1 and 2 developed for this study. The presence of the underlying Rome Trough and Appalachian orogeny play an important role in the development of this stress anisotropy. Maximum natural fracturing density should be prevalent in regions of tectonic relief, indicated by low stress ratios. Parts of southwestern W.Va. lie within an area with the stress ratio values ranging from 0.43 to 0.70. In situ stress measurements corresponding to sites in Plate 1 are given in Table D-1. For this study, cross-section No. 1 was analyzed with 481 elements (Figure D-1). Four separate cases were examined with variations in material properties and in situ stresses. The basement was assumed to be fixed with skewed roller supports in the abutment (fault slope). Representative material properties, selected from literature, are listed in Table D-2. Values selected for E and ν were based on the maximum values measured for specific sedimentary rock types. To evaluate the sensitivity with respect to these values, analyses were conducted by first using these maximum values and then repeating with E reduced by 50% and ν reduced to 0.25 below the Devonian Shale.

Evaluations for the following cases were conducted:

Case 1A

Based on the stress ratios suggested by the literature, the horizontal stresses assumed from the surface to the basement (Fig. D-2) were:

Left (NW basin) $\sigma_{Horizontal} = 0.70\ \sigma_{Overburden}$

Right (SE basin margin) $\sigma_{Horizontal} = \sigma_{Overburden}$

The material properties are listed in Table D-2.

Case 1B

The stress conditions for Case 1A were assumed with E reduced by 50% and ν reduced to 0.25 below the Devonian.

Case 2A

For this case (Fig. D-3), the stress conditions for case 1A were applied only down to the base of the upper Silurian (unit 5). Below this unit, it was assumed that the horizontal stresses were based on

$$\sigma_{Horizontal} = \frac{\nu}{1-\nu}\ \sigma_{Overburden}$$

Case 2B

For this case, case 2A was modified in the manner described in Case 1B (Fig. D-4).

Figures D-5 through D-8 graphically compare the stresses used in each case. The actual values used are shown in Table D-3.

It is apparent from Figs. D-9 through D-12 that the most pronounced effects are evident above the basement fault due to the support conditions, i.e. the skewed roller support with the most extreme being Case 2B. For this case, at a distance of 75,200 ft from the northwest, within the Devonian the stress ratio approaches a value of 0.24 and is comparable with the value of 0.37 for Case 2A. This appears to have some significance, if the assumed support condition approximates the actual condition. This implies that there may be some degree of higher fracture density then presumed from the stress trajectory ratio. It takes on added significance when correlated with the geologic conditions shown in Plates 1 and 2. As

☆U.S. GOVERNMENT PRINTING OFFICE:1983 -746 -081/ 2168 REGION NO. 4

shown in Plate 1, this location approximately correlates with the boundary between two coal fracture domains 4 and 6. On its own merit, the boundary of these domains is sufficient in terms of suggesting some stress concentration and also correlates with the axis of the Cabin Creek syncline.

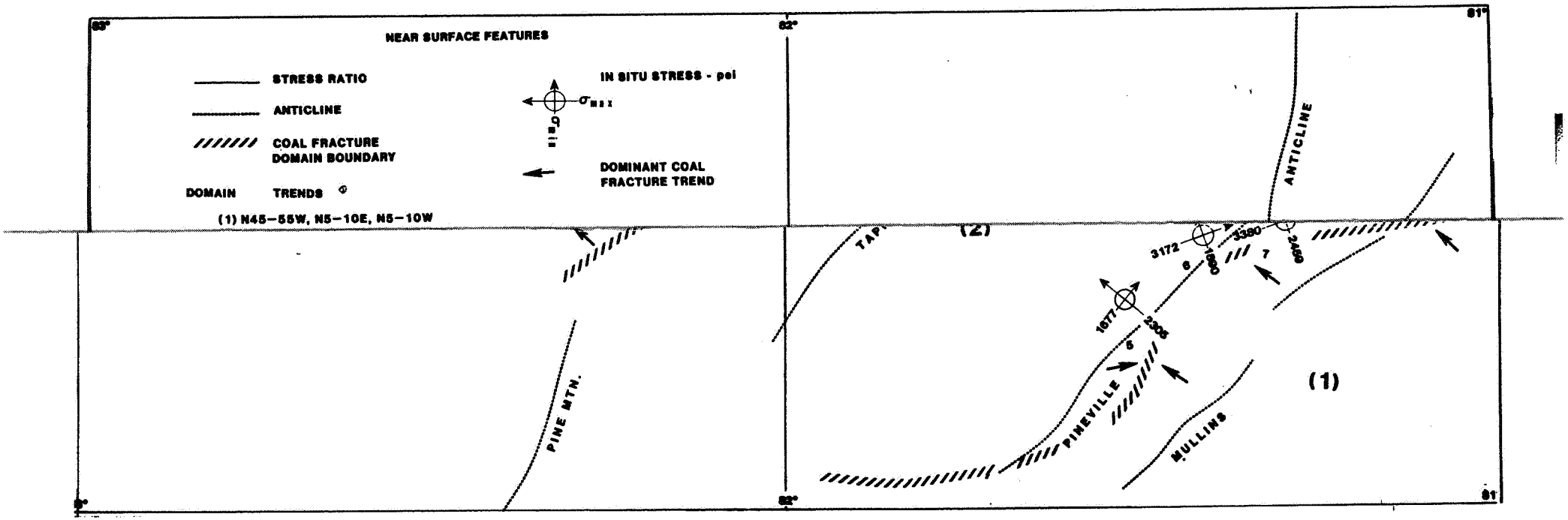
NEAR SURFACE FEATURES
STRESS RATIO
ANTICLINE
COAL FRACTURE DOMAIN BOUNDARY
DOMAIN TRENDS
(1) N45–55W, N5–10E, N5–10W
IN SITU STRESS - psi
DOMINANT COAL FRACTURE TREND
82°
81°
ANTICLINE
(2)
3172
1690
3390
2469
1677
2308
PINEVILLE
MULLINS
PINE MTN.
(1)

PLATE 1

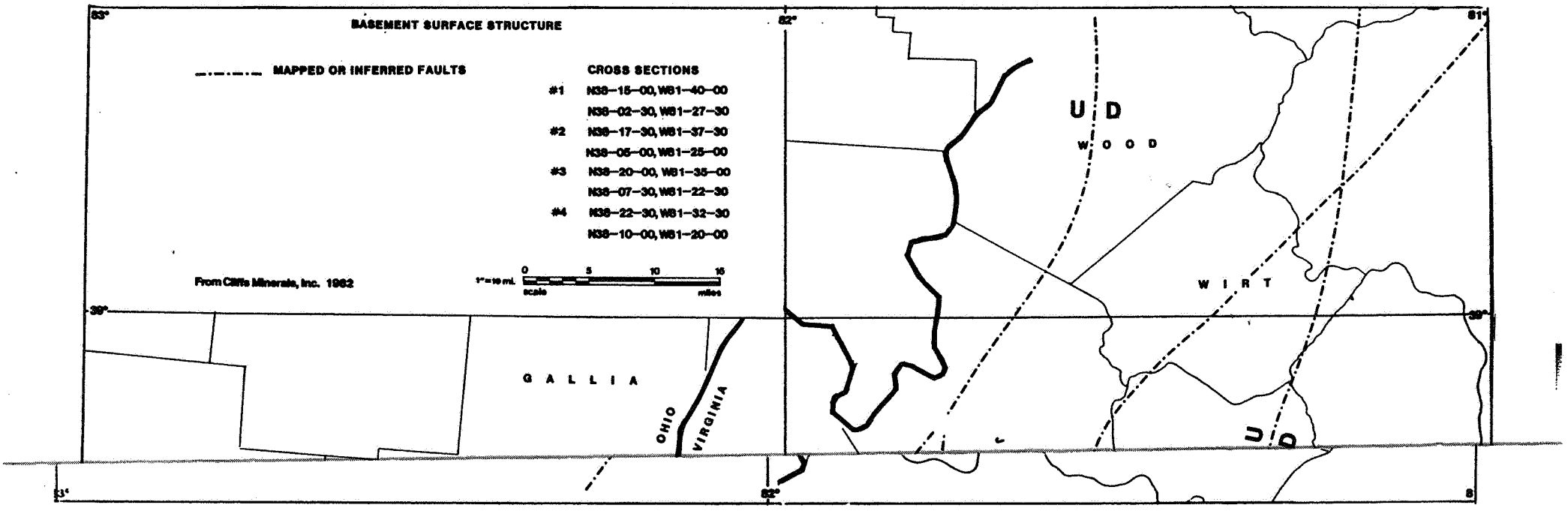
BASEMENT SURFACE STRUCTURE
MAPPED OR INFERRED FAULTS
CROSS SECTIONS
#1 N38–15–00, W81–40–00
N38–02–30, W81–27–30
#2 N38–17–30, W81–37–30
N38–05–00, W81–25–00
#3 N38–20–00, W81–35–00
N38–07–30, W81–22–30
#4 N38–22–30, W81–32–30
N38–10–00, W81–20–00
From Cliffs Minerals, Inc. 1982
1"=10 mi.
0 5 10 15
scale
miles
83°
82°
81°
39°
38°
U D
WOOD
WIRT
GALLIA
OHIO
VIRGINIA
U D

PLATE 2

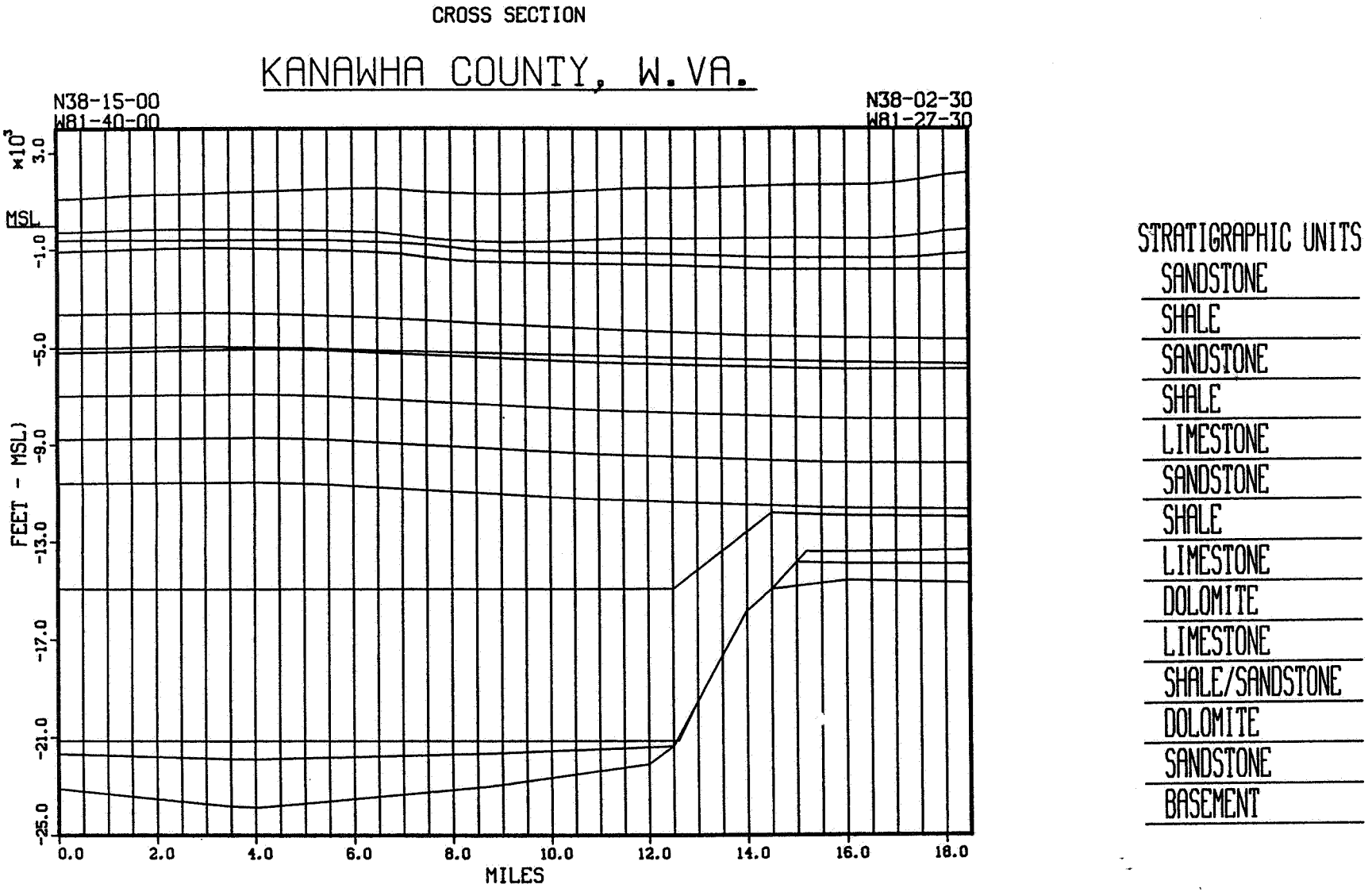

Figure D-1. Finite Element Discretization of Cross-Section #1.

TABLE D-1

IN SITU STRESS MEASURMENTS
REFERENCES TO PLATE 1

Plate Ref.	Hmax (psi)		Hmin (psi)	Depth (feet)	V (psi)	Stress Ratio	Reference
1	5901	N50E 5	2610	2755	3036	.86	Haimson Devonian Shale
2	4390	N50E 5	2360	2745	3210	.73	Terra Tek Devonian Shale
3	3332	N50E %	2374	2746	3095	.77	Lindner & Halprin Devonian Shale
4	-	-	-	-	-	-	Cliffs Minerals
5	2305	N52W	1677	1100	1240	1.35*	Tosco/Agapito Coal - Becklev No2 Mine
6	3172	N75E	1890	1100	1240	1.52*	Tosco/Agapito Coal - Becklev No1 Mine
7	3380	N68E	2459	863	973	2.53*	Tosco/Agapito Coal - Maple Meadows Mine
8	3339	N59E	2515	830	935	2.69*	Tosco/Agapito Coal - Beckley Mining Co Mine
9	3815	N57E	3101	1140	1285	2.41*	Tosco/Agapito Coal - Bonny Mine
10	-	-	-	-	-	-	Cliffs Minnerals
11	-	-	-	-	-	-	Cliffs Minerals
12	-	-	-	-	-	-	Cliffs Minerals

TABLE D-2

MATERIAL PROPERTIES

PERIOD	ROCK TYPE & Series	SPECIFIC WEIGHT (lbs/cf)	ELASTIC MODULUS (10x6 psi)	POISSON'S RATIO
PENNSYLVANIAN	SANDSTONE Pottsville	141.71	2.069	.25**
MISSISSIPPIAN	SHALE Mauch Chunk Greenbrier	171.05	5.0**	.21
MISSISSIPPIAN	SANDSTONE Pocono Weir Berea	142.96	2.069	.38
DEVONIAN	SHALE Huron Java West Falls Sonyea Genesee	162.84	4.4	.21
SILURIAN	LIMESTONE Onondaga Oriskany Cayugan McKenzie Kiefer	171.0*	12.0**	.30+
SILURIAN	SANDSTONE Tuscarora	152.0*	7.0**	.25+
ORDOVICIAN	SHALE Juniata Martinsburg	166.0*	5.0**	.21+
ORDOVICIAN	LIMESTONE Chazy Chambersburg	172.0*	12.0**	.30+
ORDOVICIAN	DOLOMITE Conococheague Stonehenge Beekmantown	174.0*	13.5**	.34+
CAMBRIAN	LIMESTONE Elbrook	172.0*	12.0**	.30+
CAMBRIAN	SHALE Rome	166.0*	5.0**	.21+
CAMBRIAN	DOLOMITE Shady	174.0*	13.5**	.34+
CAMBRIAN	SANDSTONE Unicoi Harpers Antietem	168.0*	7.0**	.25+

* max. assumed (Lama, Vol IV, Table 58) ** max. assumed (Stag and Zienkiewicz, Fig 1.5 and 1.6) + max. assumed (Goodman, Table 3.1)

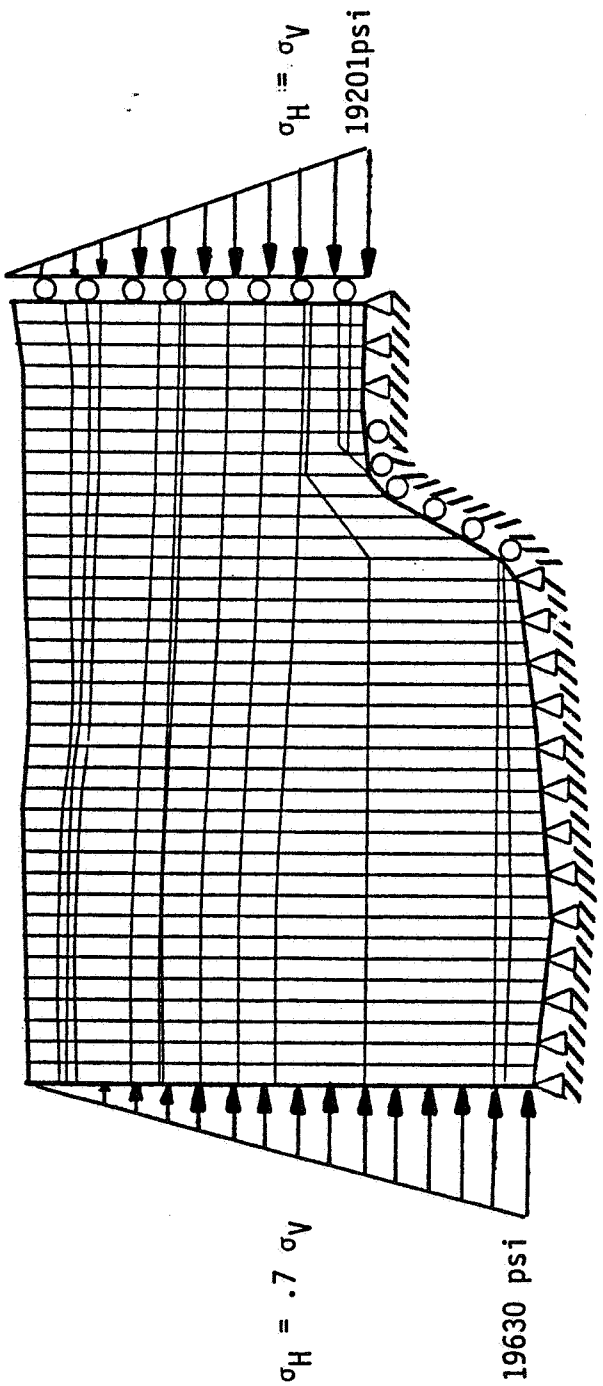

CASE 1A: ν & E remain unchanged

CASE 1B: Below Devonian, ν = .25 & E reduced 50%

Figure D-2. Boundary Conditions for Model Cases 1A and 1B.

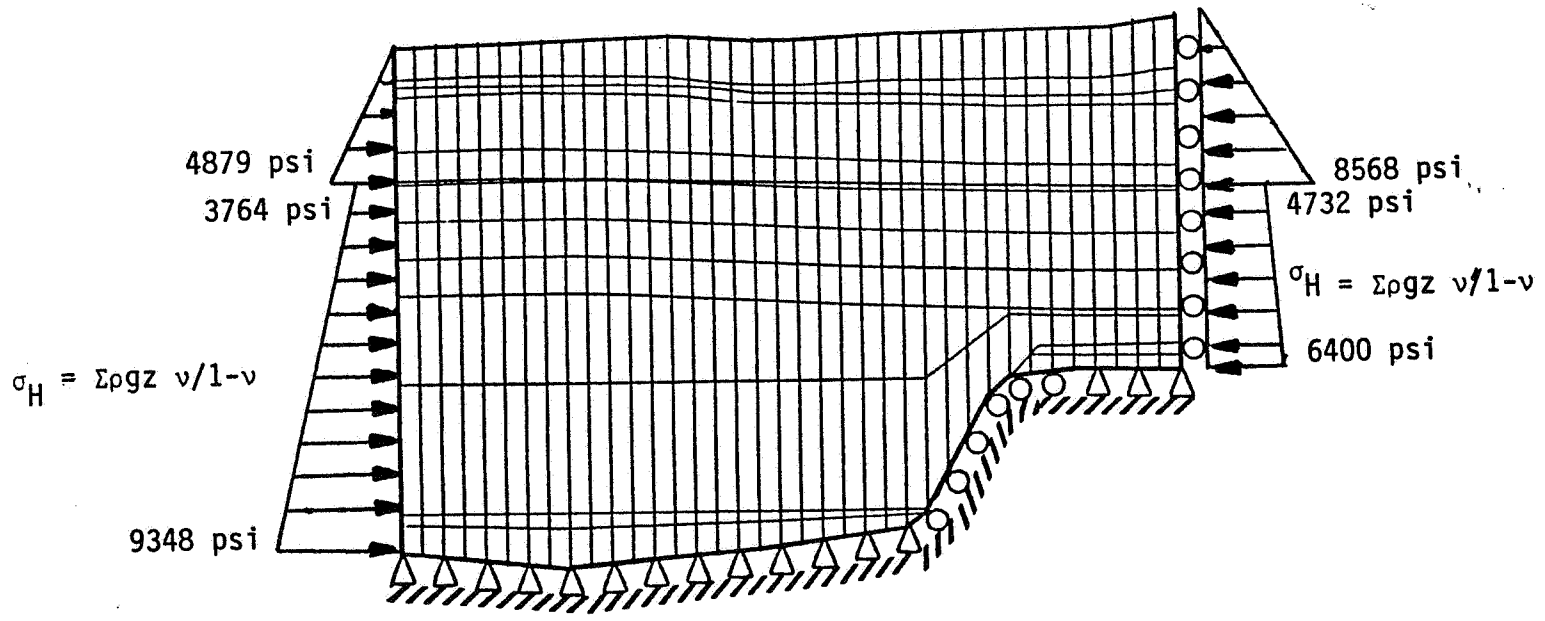

Figure D-3. Boundary Conditions for Model Case 2A.

FIGURE 5

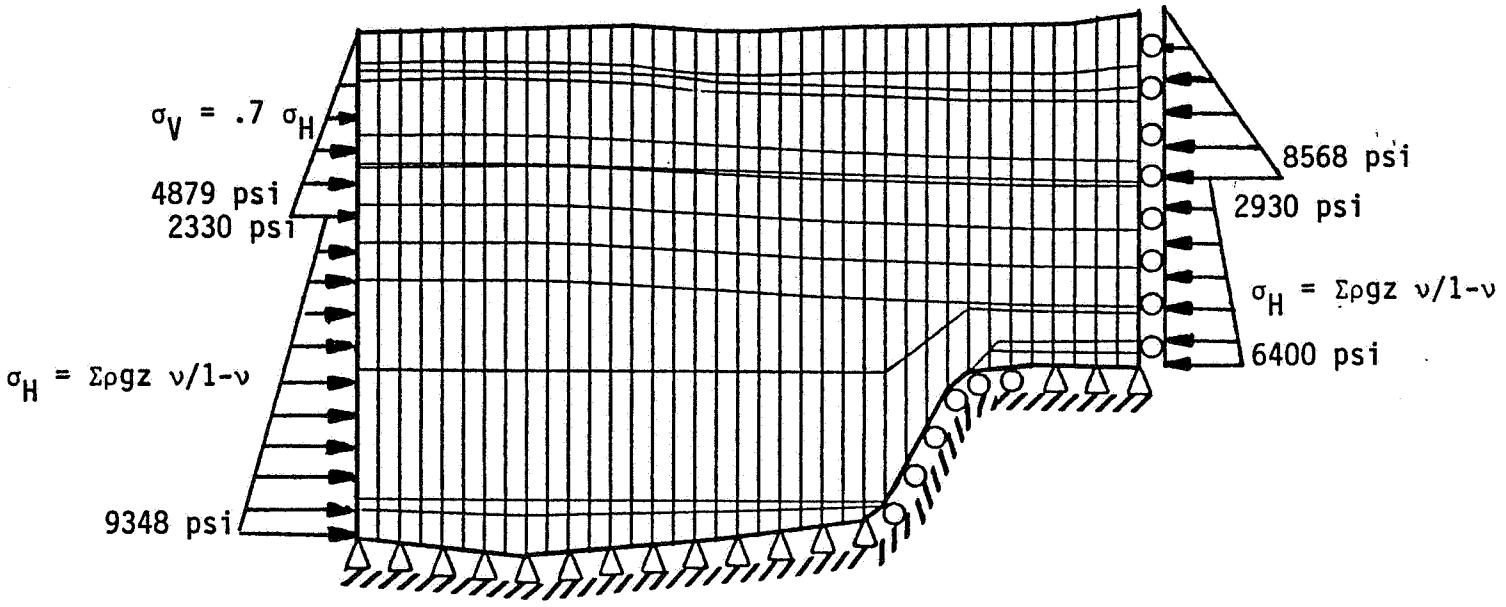

CASE 2B: Below Devonian, ν = .25 & E reduced 50%

Figure D-4. Boundary Conditions for Model Case 2B.

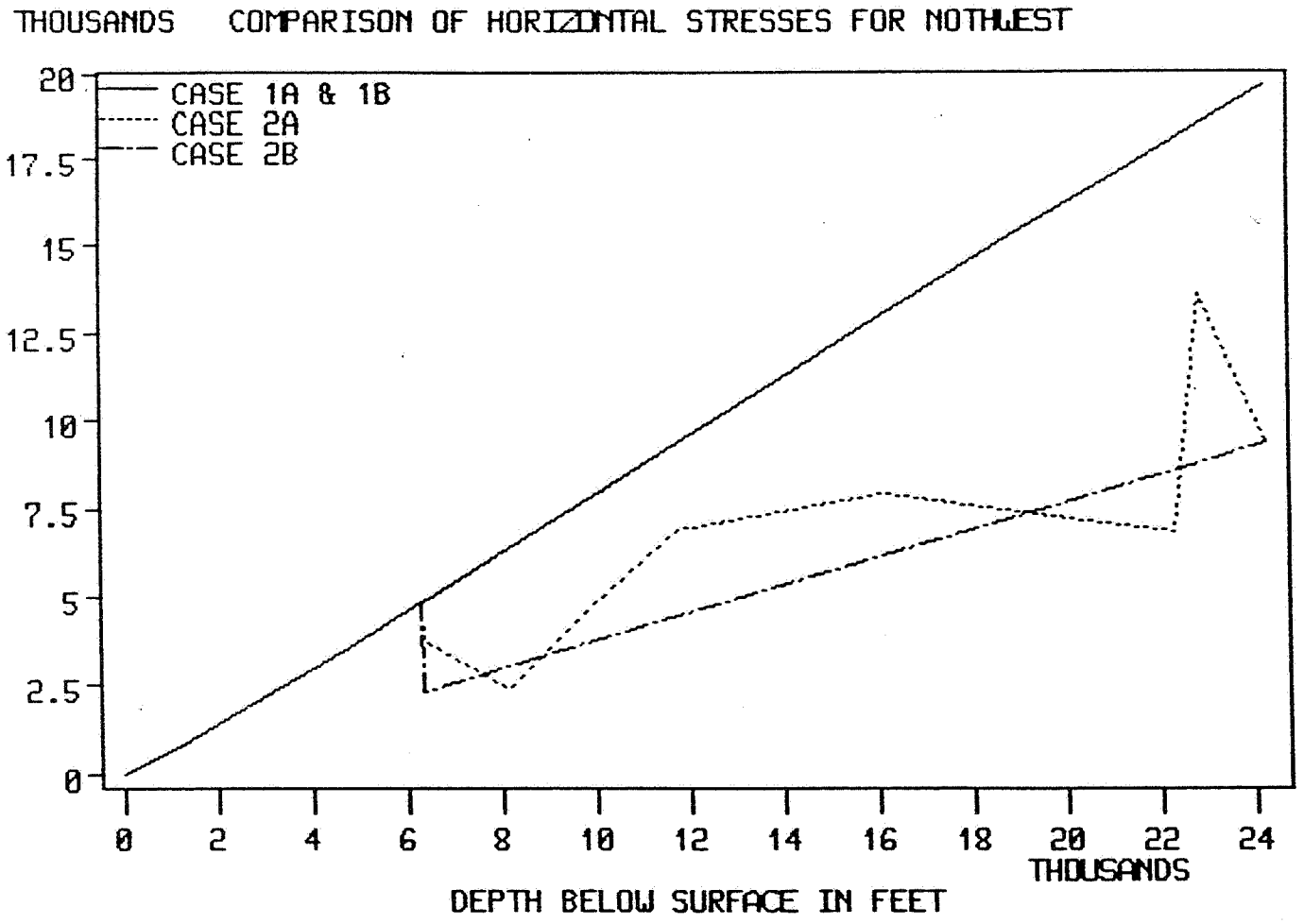

Figure D-5. Comparison of Horizontal Stresses on Northwest Cross-Section for Different Cases.

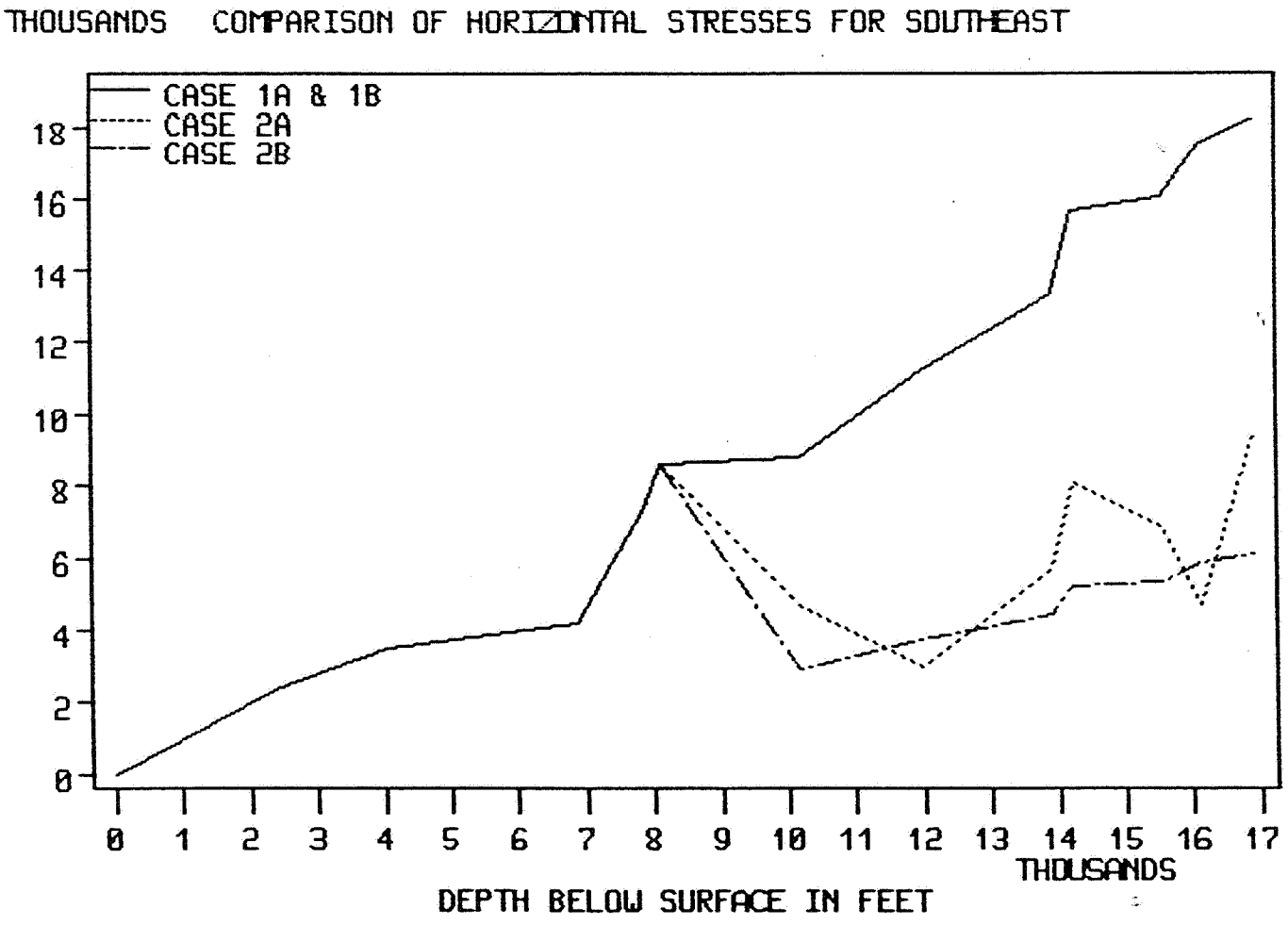

Figure D-6. Comparison of Horizontal Stresses on Southeast Cross-Section for Different Cases.

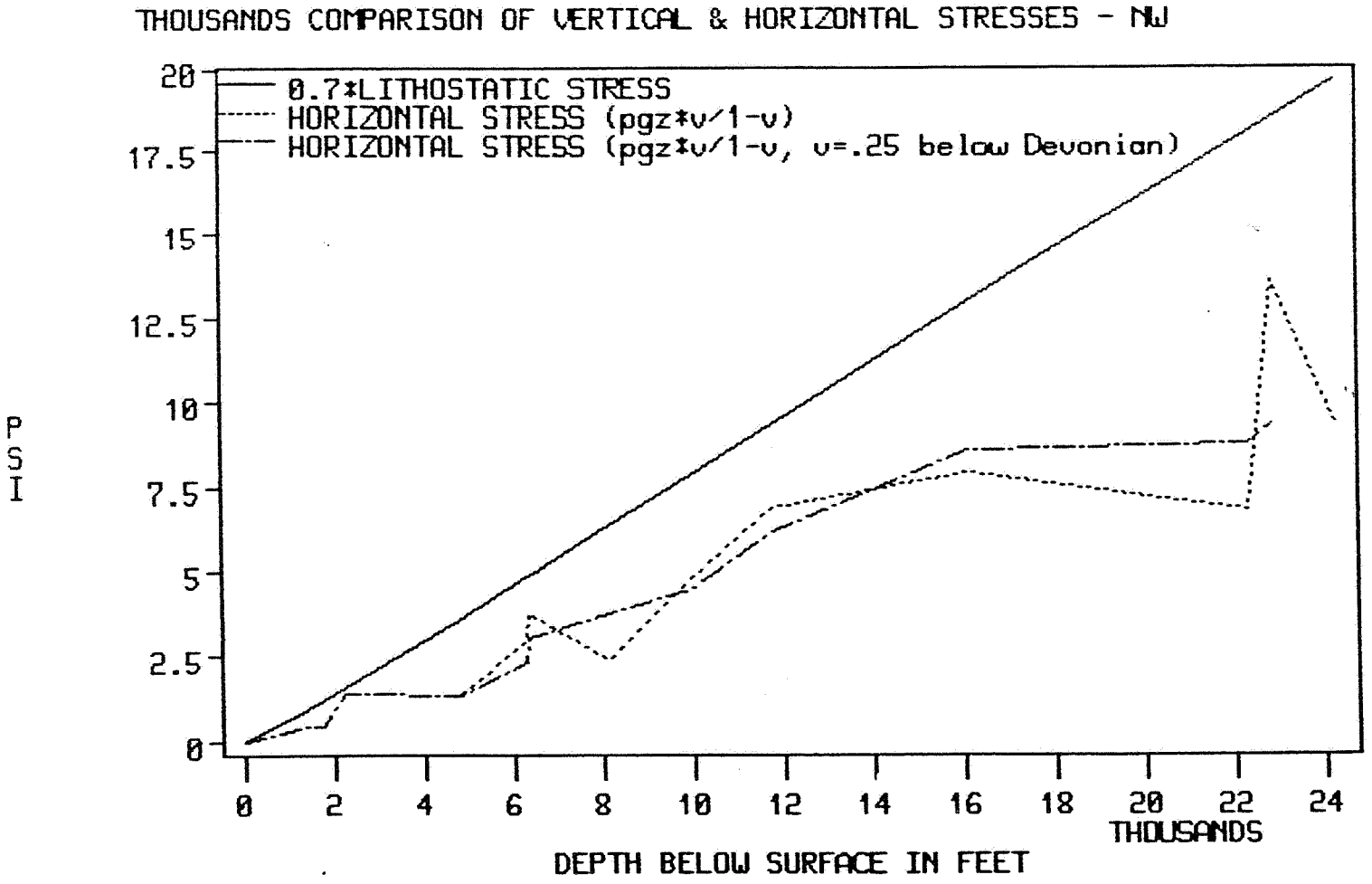

Figure D-7. Comparison of Vertical and Horizontal Stresses on Northwest Cross-Section.

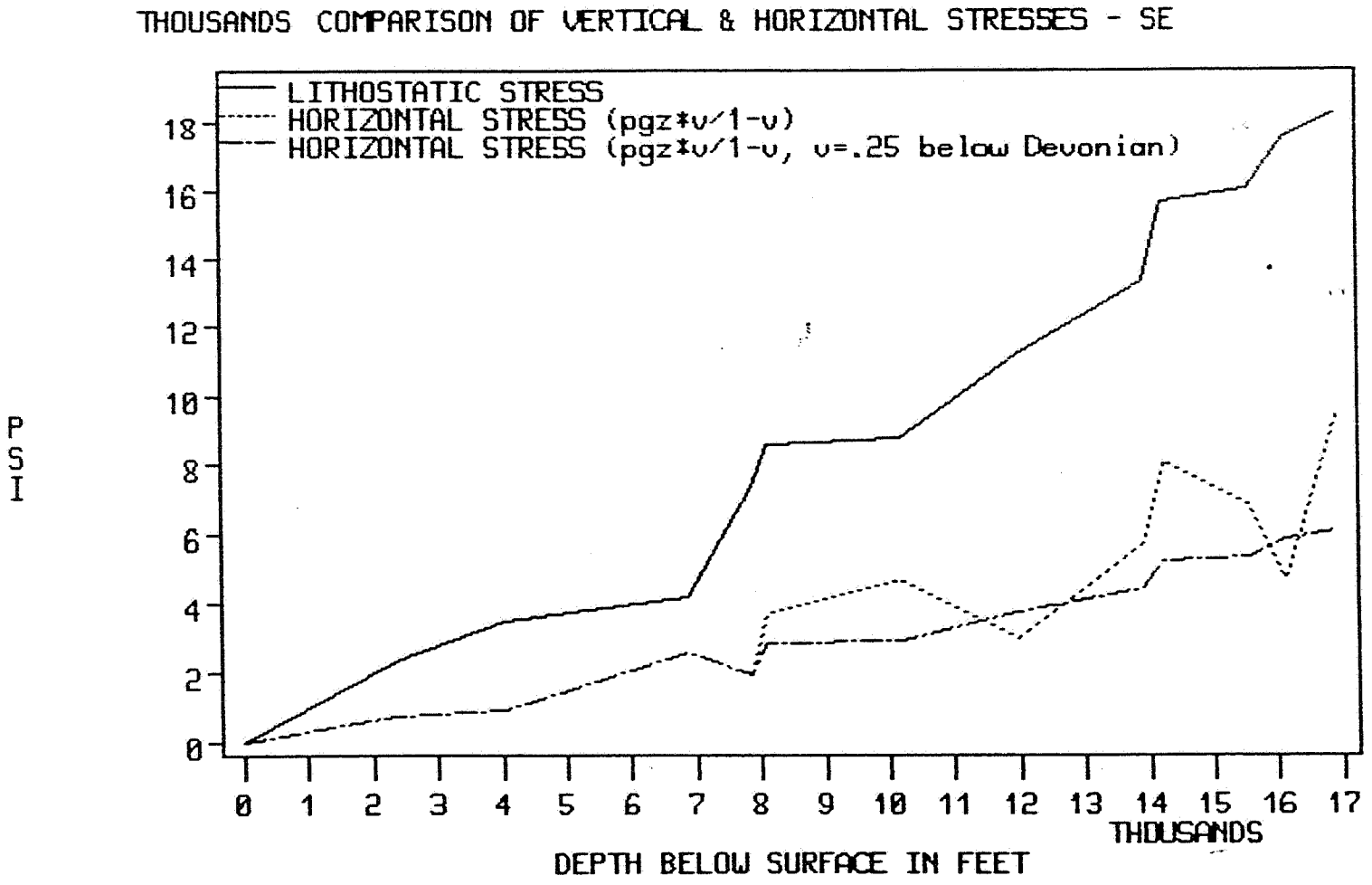

Figure D-8. Comparison of Vertical and Horizontal Stresses on Southeast Section.

NORTHWEST

UNIT	DEPTH	CASE1A	CASE2A	CASE2B
1	0	0	0	0
2	1410	971.3055	971.3055	971.3055
3	1755	1258.166	1258.166	1258.166
4	2230	1588.270	1588.270	1588.270
5	4760	3590.972	3590.972	3590.972
6	6310	4879.409	4879.409	4879.409
7	6330	4894.187	3764.763	2330.562
8	8130	6346.687	2410.131	3022.229
9	9930	7851.680	4807.152	3738.895
10	11730	9374.180	6898.75	4463.896
11	16076	13007.92	7964.034	6194.25
12	22280	18014.20	6840.833	8578.187
13	22820	18470.95	13593.33	8795.687
	24240	19630.61	9347.910	9347.910

SOUTHEAST

UNIT	DEPTH	LITHOS	CASE2A	CASE2B
1	0	0	0	0
2	2360	2322.465	2322.465	2322.465
3	4062	3498.437	3498.437	3498.437
4	6870	4205.298	4205.291	4205.291
5	7870	7380.673	7380.673	7380.673
6	8080	8568.173	8568.173	8568.173
7	10180	8789.839	4732.993	2929.944
8	11980	11210.67	2980.048	3736.888
9	13905	13360.67	5726	4453.555
10	14223	15686.71	8081.027	5228.902
11	15548	16066.54	6885.659	5355.513
12	16128	17593.97	4676.875	5864.659
13	16905	18294.81	9424.597	6098.271
		19201.31	6400.437	6400.437

TABLE D-3

Values for horizonatal stress used in modeling - values in psi.

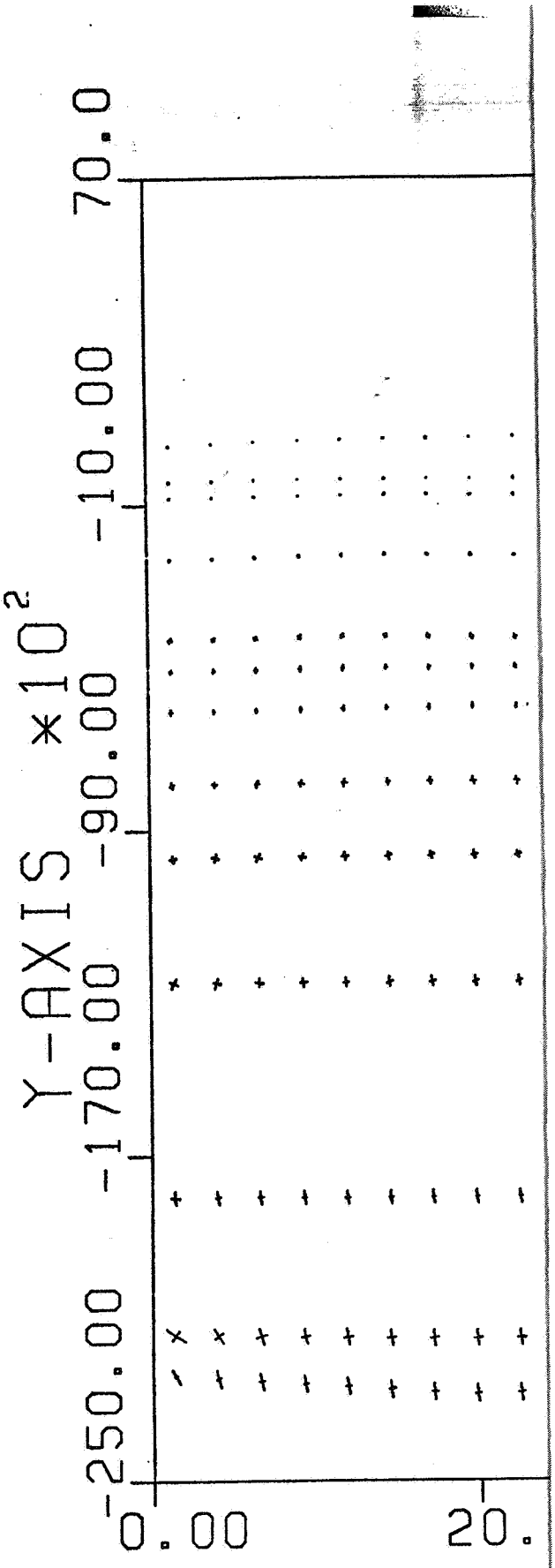

CASE 1A

+ 136875.0 LINE-TENS. STR.

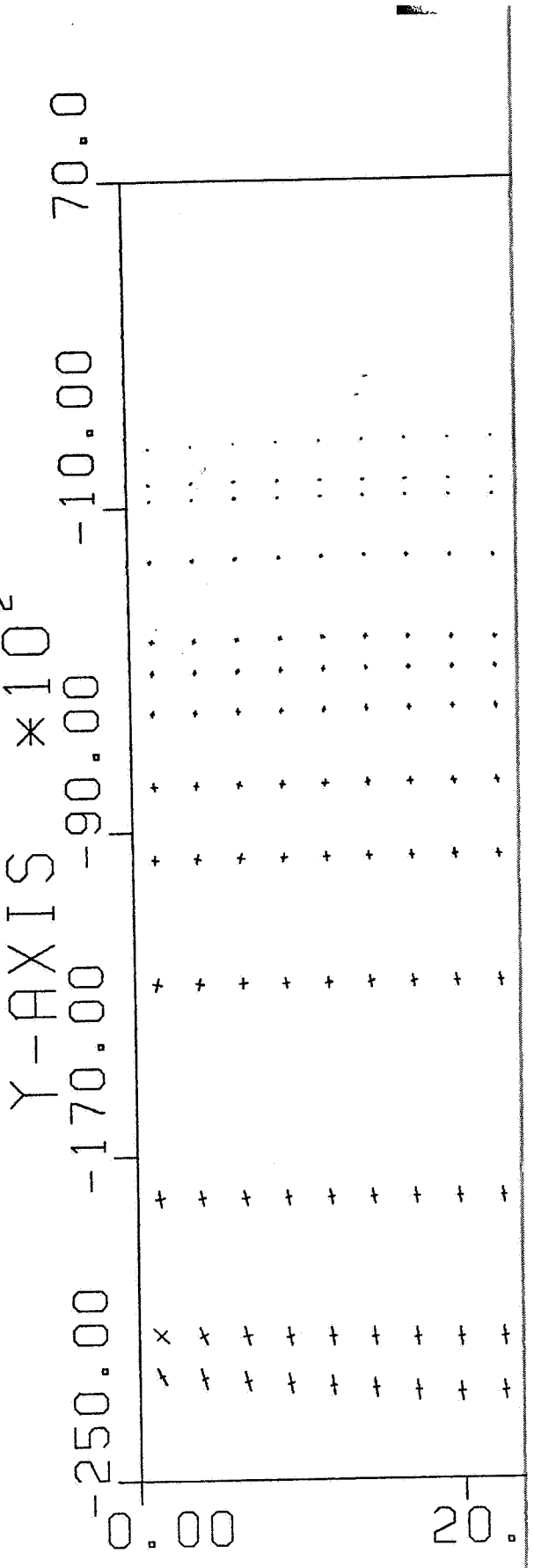

CASE 1B

+ 116805.5K LINE-TENS. STR.

Figure 9-11. Principal stress magnitudes for case 2A.

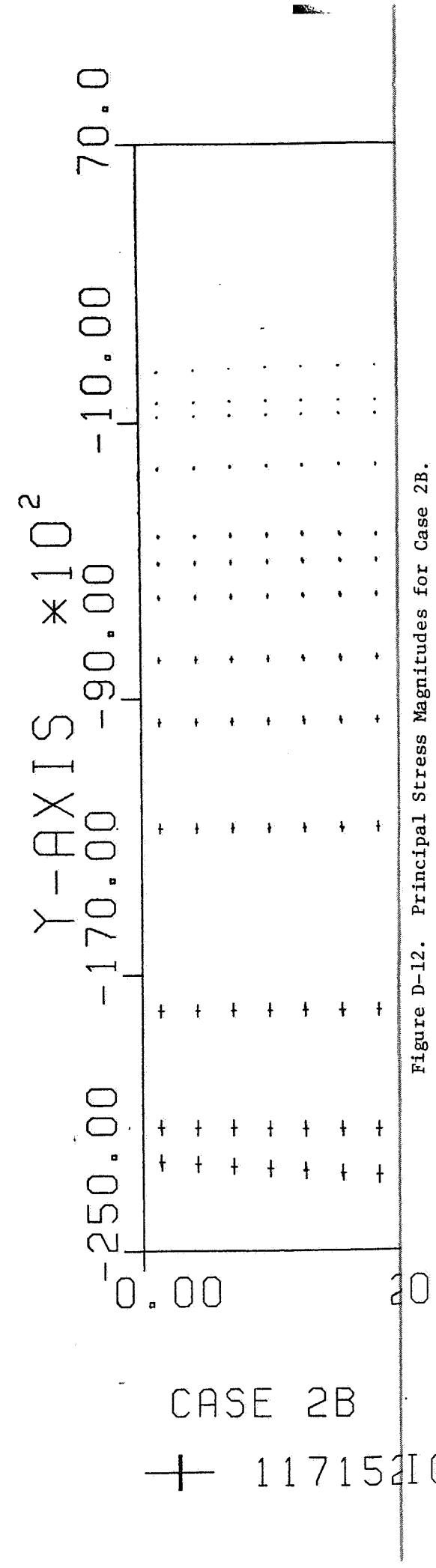

Figure D-12. Principal Stress Magnitudes for Case 2B.